Power, Efficiency, and Emissions Optimization of a Single Cylinder Direct-Injected Diesel Engine for Testing of Alternative Fuels through Heat Release Modeling

BY

Jonathan Michael Stearns Mattson

Submitted to the graduate degree program in the Department of Mechanical Engineering and the Graduate Faculty of the University of Kansas in partial fulfillment of the requirements for the degree of Master of Science.

_____

Chair: Dr. Christopher Depcik

_____

Dr. Peter TenPas

_____

Dr. Edward Peltier

Defended: June 19th, 2013

The Thesis Committee for Jonathan Mattson certifies that this is the approved version of the following thesis:

Power, Efficiency, and Emissions Optimization of a Single Cylinder Direct-Injected Diesel Engine for Testing of Alternative Fuels through Heat Release Modeling

BY

Jonathan Michael Stearns Mattson

_____

Chair: Dr. Christopher Depcik

Accepted: June 20th, 2013

Abstract

The increasing dependency of the global economy on mineral fuels necessitates the investigation and future implementation of renewable fuels. Within the spectrum of compression ignition engines, this requires an understanding of the differences in combustion of alternative fuels (including biodiesels) from mineral diesel fuel oil, and requires an environment conducive to the experimentation necessary for future research. This thesis is a work in four parts, and gives much of the perspective necessary to empirically correlate the changes caused by differing fuel inputs. The first chapter provides a background as to the motivation of the work, its component sections, and a description of the work done previously and in parallel with the thesis. Finally, the focus of the thesis is given in order to relate the components to each other.

The second chapter takes the form of a thorough review of hydrocarbon emissions from the perspective of compression-ignition engines, including a description of the variance in emissions when switching between diesel fuels from mineral or biological sources. The broad field of hydrocarbon emissions is broken down into subspecies of the group, and a recommendation as the future catalytic aftertreatment modeling using these subspecies is given.

In chapter three, the basis of a thermodynamic equilibrium-based heat release model is given. In particular, this model is set up to use an Arrhenius-based rate of combustion calibrated to the emission profile recorded during experimentation. The model is subsequently tested and validated against previously acquired data, in order to highlight the model's ability to cope with varying testing modes, including variable fuels, Exhaust Gas Recirculation, or changing aspiration techniques.

The final chapter describes the experimental procedure used to find the proper injection timings to trigger the Maximum Brake Torque condition at a given engine speed as a function of engine load, with the goal of accelerating future calibration of the improved test cell. These timings are also compared to the emissions profile of the engine, with the goal of linking variations in efficiency and emissions composition to variable injection timings.

Acknowledgements

This work was made possible by the guidance of Dr. Christopher Depcik of the Department of Mechanical Engineering. Furthermore, assistance from Dr. Edward Peltier (of the Department of Civil, Environmental, and Architectural Engineering), as well as advice from Andrew Duncan (of the Department of Chemical and Petroleum Engineering), greatly aided in the decision making process in the modeling of biodiesel fuels and emissions. Funding was provided, in part, by the University of Kansas Department of Mechanical Engineering, as well as the University of Kansas Transportation Research Institute. Finally, the assistance and experience of Michael Mangus and Chenaniah Langness proved to be invaluable in the creation of this work.

Table of Contents

Nomenclature.....xv

1.1 Introduction.....1

1.2 Engine Test Cell Prior and Parallel Work.....2

1.3 Thesis Focus.....4

Chapter II: Recommendations for the Next Generation of Hydrocarbon Modeling with respect to Diesel Exhaust Aftertreatment and Biodiesel Fuels.....6

2.1 Abstract.....6

2.2 Introduction.....7

2.3 Hydrocarbons.....11

2.3.1 Vapor Phase Hydrocarbons.....11

2.3.2 Aldehydes and Ketones.....15

2.3.3 Ozone Formation.....15

2.3.4 Heavy Hydrocarbons.....20

2.4 Biodiesel Emissions.....20

2.4.1 Soybean-Derived Biodiesel.....22

2.4.2 Waste Cooking Oil-Derived Biodiesel.....24

2.4.3 Rapeseed Oil-Derived Biodiesel.....24

2.4.4 Other Biodiesel Sources.....25

2.5 Measurement Techniques.....25

2.6 Hydrocarbon Model.....28

2.7 Conclusions.....31

Chapter III: Equilibrium Heat Release Model as an Extension of Emissions Analysis of Direct Injection Compression Ignition Engines....34
3.1 Abstract....34
3.2 Introduction....34
3.3 Model Equations....41
3.3.1 Components of the 1st Law of Thermodynamics....43
3.3.2 Data Preparation....50
3.3.3 Ideal Gas Approximation....54
3.3.4 Temperature-Correlated Values....56
3.3.5 Intake Conditions and the Chemistry of Combustion....57
3.3.6 Fuel Injection, Ignition Delay, and Combustion Duration....65
3.3.7 Combustion Cycle Calculation....75
3.3.8 Post Processing and Data Storage....85
3.3.9 Graphical User Interface....89
3.4 Results and Discussion....91
3.4.1 Variable Loading....95
3.4.2 Ignition Delay Correlation....99
3.4.3 Pressure Filtering....101
3.4.4 Fuel Testing....102
3.4.5 Exhaust Gas Recirculation....109
3.5 Conclusions....113

Chapter IV: Efficiency and Emissions Mapping for a Single-Cylinder, Direct Injected Compression Ignition Engine....115
4.1 Abstract....115
4.2 Introduction....115

4.3 Experimental Setup....120
4.3.1 Heat Release....123
4.3.2 Procedure....123
4.4 Results and Discussion....125
4.4.1 Performance and Rate of Heat Release....128
4.4.2 Injection, Ignition, Peak Pressure, and Peak Rate of Heat Release....142
4.4.3 MBT Timing Methods....146
4.4.4 Emissions....148
4.5 Conclusions....157

References....159

Appendices....167

Table of Figures

Chapter II: Recommendations for the Next Generation of Hydrocarbon Modeling with respect to Diesel Exhaust Aftertreatment and Biodiesel Fuels

Figure 1. Conversion of different HC species as function of temperature over a Diesel Oxidation Catalyst [33].....9

Figure 2. Examples of BTEX compounds, highlighting the benzene ring structure inherent to the group. Pictured clockwise from upper left; benzene, toluene, ethylbenzene, and three forms of xylene [45].....14

Figure 3. Mechanism for the formation of ozone in a NOx and VOC environment [51].....17

Chapter III: Equilibrium Heat Release Model as an Extension of Emissions Analysis of Direct Injection Compression Ignition Engines

Figure 4. The separation of the three in-cylinder zones, occurring at an arbitrary time after the beginning of combustion.....39

Figure 5. The conceptual separation of the three in-cylinder zones, occurring at an arbitrary time after the end of combustion.....40

Figure 6. Temperature versus entropy diagram derived from the same pressure trace shifted to place TDC at various distances after the maximum pressure indicated by the pressure trace.....52

Figure 7. Unfiltered pressure data. Various phenomena can lead to poor readings at certain portions of the engine cycle, most prominently during combustion. Degrees are listed ATDC.....53

Figure 8. The global reaction formula used for evaluating the overall combustion reaction..... 58

Figure 9. The stoichiometric reaction of air and fuel.....62

Figure 10. The simplified stoichiometric reaction of air and fuel.....62

Figure 11. The local reaction of oxygen and fuel..... 62

Figure 12. The flow of mass through entrainment and production from the fuel and unburned zones into the burned zone.....76

Figure 13. The GUI used as an interface between the User and the HR model in MATLAB.....90

Figure 14. Summation of work done per time step by (or on) the fuel, unburned, burned, and total volumes from IVC to EVO, during a 100% engine load test without turbocharging.....92

Figure 15. Cumulative heat transfer to the cylinder walls after ignition until EVO using calibrated correlations for heat transfer during a 100% load test without turbocharging.....93

Figure 16. Summation of the change in internal energy per time step from IVC to EVO for the fuel, unburned, burned, and total volumes during a 100% engine load test without turbocharging.....94

Figure 17. Components and summation of HR from IVC to EVO during a 100% engine load test without added turbocharging.....95

Figure 18. Rate of Heat Release from TDC to 25° ATDC at various engine loads 96

Figure 19. Rate of Heat Release from TDC to 25° ATDC at various engines load with added turbocharging..... 98

Figure 20. Cumulative mass fraction burned for varying loads, from TDC to 60° ATDC in tests without turbocharging..... 99

Figure 21. Rate of Heat Release at 0.5 N-m of loading for various fuels. Engine operated unthrottled and without turbocharging..... 103

Figure 22. Rate of Heat Release at 4.5 N-m of loading for various fuels. Engine operated unthrottled and without turbocharging..... 103

Figure 23. Rate of Heat Release at 9.0 N-m of loading for various fuels. Engine operated unthrottled and without turbocharging..... 104

Figure 24. Rate of Heat Release at 13.5 N-m of loading for various fuels. Engine operated unthrottled and without turbocharging..... 104

Figure 25. Rate of Heat Release at 16.75 N-m of loading for various fuels. Engine operated unthrottled and without turbocharging..... 105

Figure 26. Ignition timing for fuel tests without turbocharging at varying engine loads, as indicated by the pressure trace.....105

Figure 27. Peak cylinder temperature for fuel tests without turbocharging at varying engine loads.....106

Figure 28. Comparison in the RHR for varying percentages of EGR, without turbocharging, and at 4.5 N-m of engine load.....110

Figure 29. Comparison in the RHR for varying percentages of EGR, without turbocharging, and at 9.0 N-m of engine load.....110

Figure 30. Comparison in the RHR for varying percentages of EGR, without turbocharging, and at 13.5 N-m of engine load.....111

Figure 31. Comparison in the RHR for varying percentages of EGR, without turbocharging, and at 16.75 N-m of engine load.....111

Figure 32. Comparison in ignition timing for varying percentages of EGR at each engine load. Tests run on a throttled engine without turbocharging.....112

Figure 33. Comparison in the peak cylinder temperature for various percentages of EGR at each engine load. Tests run on a throttled engine without turbocharging..... 112

Chapter IV: Efficiency and Emissions Mapping for a Single-Cylinder, Direct Injected Compression Ignition Engine

Figure 34. Example of Rate of Heat Release and combustion phases found in a compression ignition engine, from Heywood [3].....117

Figure 35. Pressure traces for varying injection timings at 0.5 N-m. Engine was operated unthrottled at 1800 RPM.....126

Figure 36. Pressure traces for varying injection timings at 4.5 N-m. Engine was operated unthrottled at 1800 RPM.....126

Figure 37. Pressure traces for varying injection timings at 9.0 N-m. Engine was operated unthrottled at 1800 RPM.....127

Figure 38. Pressure traces for varying injection timings at 13.5 N-m. Engine was operated unthrottled at 1800 RPM.....127
Figure 39. Pressure traces for varying injection timings at 18.0 N-m. Engine was operated unthrottled at 1800 RPM.....128
Figure 40. Rate of Heat Release for engine operating at 1800 RPM for 0.5 N-m of load, with varying injection timings.....130
Figure 41. Normalized Rate of Heat Release for engine operating at 1800 RPM for 0.5 N-m of load, with varying injection timings.....131
Figure 42. Rate of Heat Release for engine operating at 1800 RPM for 4.5 N-m of load, with varying injection timings.....133
Figure 43. Normalized Rate of Heat Release for engine operating at 1800 RPM for 4.5 N-m of load, with varying injection timings.....133
Figure 44. Rate of Heat Release for engine operating at 1800 RPM for 9.0 N-m of load, with varying injection timings.....135
Figure 45. Normalized Rate of Heat Release for engine operating at 1800 RPM for 9.0 N-m of load, with varying injection timings.....135
Figure 46. Rate of Heat Release for engine operating at 1800 RPM for 13.5 N-m of load, with varying injection timings.....137
Figure 47. Normalized Rate of Heat Release for engine operating at 1800 RPM for 13.5 N-m of load, with varying injection timings.....137
Figure 48. Rate of Heat Release for engine operating at 1800 RPM for 18.0 N-m of load, with varying injection timings.....139
Figure 49. Normalized Rate of Heat Release for engine operating at 1800 RPM for 18.0 N-m of load, with varying injection timings.....140
Figure 50. Ignition, peak pressure, and peak RHR timings for MBT at loads below 18.0 N-m.....141
Figure 51. BSFCg and IMEPg for MBT timing at all loads..... 141

Figure 52. Pressure trace for MBT conditions at loads below 18.0 N-m.....142

Figure 53. Normalized RHR for MBT conditions at loads below 18.0 N-m.....142

Figure 54. Relationship between Injection Timing and Ignition Delay at all engine loads.....143

Figure 55. Relationship between Injection Timing and Peak Pressure Timing at all engine loads.....144

Figure 56. Relationship between Injection Timing and Peak RHR Timing at all engine loads..... 144

Figure 57. Relationship between Peak Pressure Timing and Peak RHR Timing at all engine loads..... 145

Figure 58. All timings for MBT indication methods for MBT injection timing for engine loads below 18.0 N-m at 1800 RPM..... 146

Figure 59. All timings for MBT indication methods for engine loads below 18.0 N-m at 1800 RPM..... 147

Figure 60. Brake specific production of NOx for all tested engine loads at 1800 RPM.....149

Figure 61. Brake specific production of PM for all tested engine loads at 1800 RPM.....150

Figure 62. Brake specific production of CO emissions for all tested engine loads at 1800 RPM.....151

Figure 63. Brake specific production of THC emissions for all tested engine loads at 1800 RPM.....152

Figure 64. Fractional composition of THC species at 1800 RPM at 0.5 N-m.....154

Figure 65. Fractional composition of THC species at 1800 RPM at 4.5 N-m.....155

Figure 66. Fractional composition of THC species at 1800 RPM at 9.0 N-m.....155

Figure 67. Fractional composition of THC species at 1800 RPM at 13.5 N-m.....156

Figure 68. Fractional composition of THC species at 1800 RPM at 18.0 N-m.....156

Figure 69. Emissions of n-octane for all engine loads at 1800 RPM.....157

Table of Tables

Chapter II: Recommendations for the Next Generation of Hydrocarbon Modeling with respect to Diesel Exhaust Aftertreatment and Biodiesel Fuels

Table 1. Alphabetized list of MSAT compounds targeted by the EPA [9].....10

Table 2. Reactivity data for Volatile Organic Compounds, part I [55].....18

Table 3. Reactivity data for Volatile Organic Compounds, part II [55].....19

Table 4. EPA MSAT Tier Assignments for Soybean Biodiesel [9]..... 22

Table 5. Difficulty of measurement for various emissions groups through separate means..... 28

Table 6. Investigation into HC species delineated by low, middle, and high levels.....29

Chapter III: Equilibrium Heat Release Model as an Extension of Emissions Analysis of Direct Injection Compression Ignition Engines

Table 7. Variables used in conjunction with Equation 77 and the corresponding authors; Φ is the bulk equivalence ratio..... 71

Table 8. Yanmar L100v Engine Parameters..... 91

Table 9. Engine output characteristics for varying engine load, without turbocharging..... 97

Table 10. Engine output characteristics for varying engine load, with turbocharging..... 98

Table 11. Onset of combustion with corresponding authors, as well as the point of ignition indicated by the pressure trace, evaluated in tests without turbocharging.....100

Table 12. Onset of combustion with corresponding authors for varying percentages of rated engine load, as well as the point of ignition indicated by the pressure trace, for tests with turbocharging..... 100

Table 13. End of combustion as indicated by the 1st and 2nd derivatives of the pressure trace, polytropic expansion, and AFT. All values are in degrees ATDC, except where marked.....101

Table 14. Literature characteristics of various fuels and fuel blends tested. All values measured at standard pressure and 300 K..... 107

Chapter IV: Efficiency and Emissions Mapping for a Single-Cylinder, Direct Injected Compression Ignition Engine

Table 15. Yanmar Engine Specifications.....121

Table 16. Dynamometer Specifications.....122

Table 17. Gross engine output characteristics at 0.5 N-m of load for varying injection timings.....128

Table 18. Gross engine output characteristics at 4.5 N-m of load for varying injection timings.....131

Table 19. Gross engine output characteristics at 9.0 N-m of load for varying injection timings.....134

Table 20. Gross engine output characteristics at 13.5 N-m of load for varying injection timings.....136

Table 21. Gross engine output characteristics at 18.0 N-m of load for varying injection timings.....138

Table 22. Equations of various linear MBT timing methods as a function of injection timing, with associated R2 error from the gathered results.....147

Table 23. Equations of various linear MBT timing methods as a function of engine load, with associated R2 error from the gathered results.....148

Appendices

Table 24. Examples of the molecular formula and lipid number of various FAME species, as well as their fractional composition within used cooking oil, rapeseed oil, and olive oil derived biodiesels, measured by GCMS.....167

Table 25. Examples of the molecular formula and lipid number of various FAME species, as well as their fractional composition within palm oil, coconut oil, and soybean oil derived biodiesels, measured by GCMS.....168

Nomenclature

A	area [m^2], first Arrhenius coefficient [ms]
A_n	injector nozzle area [m^2]
A_s	surface area within cylinder [m^2]
a	coefficient for gas emissivity correlation [- , Pa^{-1} m^{-1}, Pa^{-2} m^{-2}, Pa^{-3} m^{-3}], lipid carbon number
b	engine bore [m], second value of lipid number
$BSFC_g$	gross brake specific fuel consumption [g kW^{-1} h^{-1}]
C_d	coefficient of discharge
c	connecting rod length [m], constant value
c_f	liquid fuel specific heat [J kg^{-1}]
c_p	constant pressure specific heat [J kg^{-1}]
$\bar{c}_p$	constant pressure molar heat [J $mole^{-1}$]
c_v	constant volume specific heat [J kg^{-1}]
d	correlation coefficient used for CHEMKIN-III correlations [- , K^{-1}, K^{-2}, K^{-3}, K^{-4}, K]
E_a	activation energy [kJ $mole^{-1}$]
e_{RMS}	RMS error in internal energy [J]
f	residual fraction (mass basis)
g	global reaction coefficients, dependant variable in Newton-Raphson and secant methods
g'	derivative of dependant variable in Newton-Raphson and secant methods
H	enthalpy [J]
h	specific enthalpy [J kg^{-1}]
$\bar{h}$	molar enthalpy [J $mole^{-1}$]
h_c	conductive heat transfer coefficient [W m^{-2} K^{-1}]
$IMEP_g$	gross indicated mean effective pressure [bar]
K	fuel combustion rate coefficient [m^3 kg^{-1} sec^{-1}]

L_b	mean beam length [m]
l	local combustion formula coefficient
m	mass [kg], number of spatial dimensions
m_f	total mass of fuel used per cycle [kg cycle^{-1}], mass of the fuel zone [kg]
$m_{f,con}$	total mass of fuel consumed by combustion [kg]
$m_{f,rem}$	mass of fuel remaining after combustion [kg]
$\dot{m}_a$	mass flow rate of air [kg s^{-1}]
$\dot{m}_f$	mass flow rate of fuel [kg s^{-1}]
$\dot{m}_{f,inj}$	mass flow rate of fuel by injection [kg s^{-1}]
N	average engine speed [rev min^{-1}]
n	moles of material [mole], total number of zones, counter for iterations
n'	second Arrhenius coefficient
n_h	number of holes on a single fuel injector
n_{inj}	number of fuel injectors within a cylinder
n_R	number of revolutions per engine cycle [rev cycle^{-1}]
P_g	gross power [kW]
p	pressure [Pa]
p_g	partial pressure of bulk CO_2 and H_2O[Pa]
p_{net}	net pressure [Pa]
Q_{hr}	heat release [J]
Q_{ht}	heat transfer [J]
Q_{LHV}	fuel lower heating value [kJ kg^{-1}]
R	gas constant [J kg^{-1} K^{-1}]
R_{univ}	universal gas constant [J mole^{-1} K^{-1}]
r	crank length [m]

r_c	compression ratio
S	entropy [J K^{-1}]
Sk	Stark number ratio of convective to radiative heat transfer
T	temperature [K]
T_f	temperature of the flame [K]
T_{inj}	injection temperature [K]
T_s	temperature, single-zone approximation [K]
T_{vap}	fuel vaporization temperature [K]
T_w	cylinder wall temperature [K]
t	time [s]
t_{step}	time step [s]
U	internal energy [J]
$\forall$	volume [m^3]
$\forall_{bowl}$	piston bowl volume [m^3]
$\forall_{clear}$	clearance volume [m^3]
$\forall_d$	displacement volume [m^3]
W	work [J], molecular weight [kg $mole^{-1}$]
$\dot{W}$	work energy per unit time [J s^{-1}], power [W]
x	mole fraction, independent variable in Newton-Raphson and secant methods
Y_{mb}	fraction of mass burned
y	mass fraction
α_w	wall absorptivity
γ	ratio of specific heats
Δ_θ	heat transfer term for thermodynamic loss angle calculation [Pa]
δ	molar amount of intake air [moles]

ε	fraction of intake air that is composed of residual gases (molar basis)
ε_{fl}	emissivity of the luminous flame
ε_g	emissivity of the bulk gas
ϵ	fraction of intake air that is composed of recycled exhaust gases (molar basis)
η	exponent controlling heat transfer in calculations for thermodynamic loss angle
η_c	combustion efficiency
η_f	fuel conversion efficiency
η_q	gross energy accountability
η_t	thermal efficiency
θ	crank angle [degree]
θ_0	crank angle offset [degree]
θ_{TDC}	crank angle for top dead center [degree]
$\hat{\theta}_{TDC}$	guessed crank angle for top dead center [degree]
ξ	molar amount of injected fuel [moles]
ρ	density [kg m^{-3}]
τ	ignition delay [s]
ϕ	equivalence ratio

Subscripts

a	air
avg	average
b	burned zone, burned
cv	control volume, bulk gas
e	entrained, exhaust
EGR	exhaust gas recirculation
f	fuel zone, fuel

fa	fuel added
fb	fuel burned
h	injector nozzle hole, cylinder head
i	index for zones, inlet
ig	time of ignition
ig,c	correlated time of ignition
ig,ex	expected time of ignition
$igend$	time of end of ignition
inj	injected, time of injection, injectors
injend	time of end of injection
IVC	time of intake value closing
j	index for species
k	index for data points
mix	fuel-air mix
p	produced, piston face
res	residual
u	unburned zone
w	carbon atoms in fuel molecule, wall
x	hydrogen atoms in fuel molecule
y	oxygen atoms in fuel molecule
z	nitrogen atoms in fuel molecule

1.1 Introduction

As nations continue to develop their industry and infrastructure, it is increasingly likely that current energy resources will be not be able to meet demand. This problem is particularly apparent within the area of automotive fuels from mineral oil sources. While world oil supplies will never be "run dry" per se, economical extraction and production of mineral fuels will become increasingly difficult in the coming years, with some researchers believing that "peak oil" has already occurred, or will occur within the next decade [1, 2]. Coupled with the expected industrialization of China and India, in addition to the rising demands of the remaining countries in a world that has surpassed 7 billion people, it is increasingly likely that world demand for petroleum will far outstrip supply [2].

The solution to this problem is multi-faceted, and will likely involve the production and use of renewable and alternative fuels. From the perspective of compression-ignition (CI) engines, this necessitates the production of fuels that can be easily substituted with minimal modification to engine design or operation. To this end, research is being done at the University of Kansas (KU) to quantify the differences in fuel characteristics in operation the operation of CI engines from the point of view of petroleum-based diesel.

These differences are apparent in the properties of the fuels themselves. Physical differences between fuels in properties such as viscosity may lead to changes in behavior (particularly fuel break up and vaporization) in direct-injected (DI) engines [3, 4]. This, in turn, exacerbates the problems of the nature of control in CI engines, where the timing of ignition is only implicitly controlled (through estimations of ignition delay) rather than the explicit control in timing seen in spark-ignition (SI) engines. Differences in fuel density can even change the timing of injection for mechanically controlled injection systems [5, 6]. Chemical differences are more apparent after the injection process has begun, particularly in the form of ignition delay and rate of combustion due to major differences between fuel molecules (such as the added oxygen content of biodiesel fuels) [4]. This in turn requires an understanding of how seemingly small changes in engine operation and timing cause a wide divergence in engine power and

efficiency. In addition, it requires the creation of combustion models that can reflect the wide variety of fuels and operating modes available.

Of particular concern are the emissions characteristics of various fuels when compared to mineral diesel. Combustion of diesel fuels within CI engines are primarily characterized by the emissions of nitrous oxides (NO_x) and particulate matter (PM), and are also emitters of carbon monoxide (CO) and hydrocarbon (HC) species. HC emissions are a particularly noteworthy area of emissions characterization, due to the incredibly large variety of compounds that can be emitted [7, 8]. While the amount of total hydrocarbon (THC) emissions is typically not a large portion of the total emissions profile, minute changes in engine operation can lead to major shifts in the types of HC emissions produced. These shifts are exacerbated by fuel changes, to the degree where certain subspecies of HC emissions can disappear entirely when moving between fuels [8, 9]. In addition, the production of certain emission species (such as polycyclic aromatic hydrocarbons, or PAHs) is of concern to regulatory groups, due to their negative effects on human health and the environment. As a result, an understanding of THC emissions production is essential to CI fuel testing.

1.2 Engine Test Cell Prior and Parallel Work

The engine used for testing at the KU is a Yanmar L100v single-cylinder DI-CI engine. Initially, the engine was included with an alternating current (AC) generator. Past experimentation has been defined in part by the limitations imposed by the engine and its components. With the goal of increased experimental freedom, multiple graduate students at KU have been involved in upgrading the test cell in recent years. These upgrades will be briefly described in the following paragraphs.

Previous testing included thorough upgrades to the capabilities governing intake parameters, including cooled Exhaust Gas Recirculation (EGR) and variable ozone addition [10]. While the Yanmar as packaged did include a passage for EGR, the passage was designed to operate using a fixed amount of EGR. To facilitate more control and variable EGR, the passage was blocked and replaced with an external system controlled independently of engine operation [10].

In addition, the testing capabilities are augmented through the use of a smoke meter and a Fourier transform infrared (FTIR) spectroscopy unit incorporating a flame ionization detector (FID), in order to provide for a thorough analysis of engine-out emissions. Between the two units, PM, THC, NO_x, and CO emissions are measured directly during experimentation, in addition to near complete speciation of all other major compounds found in some engine emissions (such as oxides of sulphur, ammonia vapor, cyanic acids, etc.). Only molecular nitrogen (N_2) and hydrogen (H_2) emissions are not measured directly, due to the FTIR's inability to measure diatomic compounds accurately (molecular oxygen is measured through a dedicated oxygen sensor within the FTIR).

The primary upgrade done in parallel to this work was to change the nature of the DI process being used by the engine. Previously, the engine utilized an in-line fuel injection system, triggered mechanically by the engine's own rotation and set to a constant injector pressure, limiting the ability of researchers to test the effects of variation in injection timing for a single fuel [11]. Furthermore, the mechanical system could only provide a change in fuel flow rate as a response to increased load, and suffered from variation in injection timing across multiple fuels. This variation was due to the variation in the bulk modulus of compressibility of different fuels (and linked to the fuel density). Injection was triggered through a mechanical system sending a period pulse through the fuel, displacing the injector needle and allowing fuel to flow into the cylinder. Deviation in density from fuels changed the speed at which the pulse propagated through the fuel, and caused the actual timing to be advanced or delayed with increases or decreases (respectively) in fuel density.

To allow the researchers more control over injection, the in-line system was replaced with a common rail DI system, whereby injection was controlled electronically through a Bosch ECU running Bosch Modas Sport. Through this system, the timing and rate of fuel flow by injection is controlled directly by the researchers, and only limited by a maximum pressure range of 10 to 200 MPa. With this injection upgrade, the timing of injection is set directly, and does not experience deviation due to fuel changes, allowing for pre-injection variations in engine operation to be negated.

1.3 Thesis Focus

A study was completed in order to ascertain the optimum engine performance characteristics of the Yanmar engine, from the perspective of mitigating engine HC emissions and/or maximizing engine performance. In addition, this work serves to form a baseline from which further fuel testing can be achieved.

In Chapter 2, an overview of the HC emissions expected from CI engines is presented. In addition to providing a profile of the expected emissions of mineral diesel fuels (including diesel fuel oil #2, jet propellant #8 (JP-8), n-heptane, or kerosene), the emissions of biodiesel fuels is also presented, in order to differentiate between mineral and biodiesel fuels, as well as between biodiesel fuels as a function of feedstock. This review serves as a recommendation for the creation of future catalytic aftertreatment models, and highlights areas of concern in the design and construction of catalysts for emissions profiles of variable fuels. Multiple authors were involved in the creation of this particular work, and each contributed efforts to individual portions of the work. Ryan O'Malley worked to provide an explanation of the methodologies by which diesel HC emissions are categorized, as well as creating the baseline description of diesel HC emissions. Dr. Christopher Depcik helped to provide perspective on the evolution of catalytic modeling which was instrumental in the creation of the new methodology. Dr. Edward Peltier served to provide insight on the distinctions between varying groups of aromatic HCs (including BTEX and PAH compounds). Jonathan Mattson was chiefly responsible for the descriptions of biodiesel emissions, as well as the notable changes in emissions when moving from mineral diesel to biodiesel. Both Jonathan Mattson and Ryan O'Malley were involved in the recommendations of the new methodology itself.

In order to provide for a means to analyze the differences in combustion between various engine operating modes, Chapter 3 describes a Heat Release (HR) model. This model was created entirely in MATLAB, and functions by balancing the varying thermodynamic processes occurring within the cylinder. The model requires a number of inputs on fuel specifications and general engine cylinder geometry, as well as the measured rates of fuel and air consumed by the engine. Finally, the model uses a

pressure trace gathered through experimentation, and is calibrated to the known combustion efficiency of the thermodynamic cycle as measured by the brake-specific production of partially oxidized material within the engine emissions (namely THC, CO, and H_2). The authors then validated and tested the model against existing data acquired from prior engine testing, showing the model's capability in calculating the cumulative HR and rate of heat release (RHR) of the engine under various testing modes. This testing includes variation in input fuel (including diesel, JP-8, n-heptane, neat biodiesel, and blends of diesel and biodiesel fuel), variation in aspiration (through the use of turbocharging), and the implementation of cooled EGR.

Finally, Chapter 4 describes subsequent experimentation done to calculate the proper timings of the Maximum Brake Torque (MBT) condition, whereby the engine is operating at peak efficiency for a given speed, load, and fuel flow rate. Through the use of an injection sweep for an intermediate engine speed, the means by which the MBT condition is correlated are used to find the injection timing required to bring about MBT for a given load. The results and validation of this MBT sweep can then be used to correlate MBT timings at other engine speeds in a time-efficient manner, allowing for an accelerated testing schedule for future experimentation. In addition, the emissions of the engine are compared as a function of injection timing, bringing to light the possible links between emissions production and MBT timing. This may provide the groundwork for future experimentation in the correlation of MBT timing to emissions speciation. This correlation may be easier to implement in the existing automobile fleet, as it would not require the addition of pressure-reading sensors to existing (or future) vehicles. This final work was done with the collective work of multiple authors. Michael Mangus was instrumental in running the experiments themselves, as well as providing his expertise on the variations in engine operation encountered during testing. Dr. Christopher Depcik created the initial experimental procedure, in addition to oversight of the process. Jonathan Mattson analyzed the varying MBT timing methodologies described in the literature using the previously described HR model, as well as providing the MBT timing correlation to be used in future testing.

Chapter II: Recommendations for the Next Generation of Hydrocarbon Modeling with respect to Diesel Exhaust Aftertreatment and Biodiesel Fuels

Jonathan M. S. Mattson*[1], Ryan O'Malley[1], Christopher Depcik[1], Edward Peltier[2]

[1] University of Kansas, Department of Mechanical Engineering

[2] University of Kansas, Department of Civil, Environmental, and Architectural Engineering

1530 W. 15th Street, Lawrence, KS, 66045-4709

* Corresponding author: jmsmattson@gmail.com

2.1 Abstract

The modeling of emitted hydrocarbons from internal combustion engines for exhaust aftertreatment devices has remained relatively unchanged since the early 1970s. This older model subdivides the hydrocarbon species into fast, slow, and non-oxidizing components. Current and future regulations from the United States Environmental Protection Agency stretch the abilities of this methodology, necessitating the need for more advanced modeling techniques. To this end, this paper provides a review on the different groups of hydrocarbons in order to provide background and contextual information on the different species expected in diesel emissions. Additionally, this work groups these species into different categories, depending on their chemical make-up, impact on human health, reactivity in the environment, and their prevalence within diesel emissions. Furthermore, this effort presents the emissions characteristics of alternative fuels by linking the feedstock source of various biodiesel fuels to the emissions produced. After understanding the different hydrocarbon emissions, a brief overview regarding the analysis of these species in the exhaust ensures that measurement of the subsequently chosen representative species is feasible. This work ends with a discussion of the choice of singular representative species for different hydrocarbon groups with the goal of improved fidelity and incorporation of biodiesel in future models.

2.2 Introduction

One of the primary objectives of the Environmental Protection Agency (EPA) revolves around the regulation of automobile emission sources, which are hazardous both to the environment and to human health. Increased population levels and the relative ease of access to automobiles have led to a dramatic increase in vehicle emissions within the United States (US). For this reason, the EPA has implemented a series of standards the automotive industry must adhere to in order for their vehicles to be sold within the US [12-14]. These regulations include maximum emissions of specific chemical species that include nitrogen oxides, unburned fuel, and carbon oxide emissions among others. The variety of these combustion products can number in the hundreds of species, each with its own characteristics. The immense amounts of chemical kinetic reactions that take place in the exhaust process are complex, and require application of a significant amount of theory in their study. In addition, decades of research is required simply to enact a new set of standards. Understanding the reactivity, mass and heat transfer dependency, and atmospheric volatility of each form of exhaust species is crucial to the advancement of cleaner automobile exhaust.

One significant topic in the study of emissions is that of exhaust hydrocarbon (HC) species. HCs form primarily from the incomplete combustion of fuel. These species range from relatively simple and stable molecules (such as methane and ethane) to immensely long and complicated HC chains, and almost everything in between [7, 8, 15]. There are a number of causes for HC emissions including intake-exhaust valve overlap (or "short-circuiting"), chamber-wall flame quenching, piston crevice flow, cylinder misfire, non-ideal mixture burning, fuel injection issues, and other phenomena resulting from the complexity of the internal combustion (IC) engine mixing and combustion processes [16, 17]. Regardless of their generation, the result is the same; complete combustion does not occur, and the remaining HC's emanate from the cylinder during the exhaust stroke.

Once free in the environment, HC emission species produce a wide variety of effects as diverse as the HC molecules themselves. Some of the more stable species (most notably methane) are quite benign to human tissue, but can be potent greenhouse gases. Other species react with nitrogen oxides and

sunlight to produce ground level ozone, a major component of smog [16]. Still others, particularly benzene, toluene, ethylbenzene, and xylene (known collectively as BTEX) are incredibly destructive to living tissue [18-23]. For these reasons, the EPA has targeted HC emissions levels as a main culprit for the degradation of air quality in major cities, and the associated rise in health issues [24].

As mentioned, HC emissions form an extremely varied group of substances with the exhaust gases of an IC engine often containing over 150 different HC compounds [15]. Grouping of these compounds typically occurs into categories such as aromatic HCs, volatile organic compounds (VOCs), or complex heavy hydrocarbons (HHCs), among others. Since each particular HC species has its own molecular geometry, attempts at mitigation through exhaust aftertreatment devices may require a specific reaction mechanism to combat each species [25]. Therefore, as regulatory efforts continue to advance, catalytic aftertreatment devices will need to combat the specific HCs targeted by legislation through more advanced catalyst formulations, as well as modeling activities and engine research.

With respect to aftertreatment device modelling, the starting point for HC compounds can be traced to Kuo et al. in 1971 whom simulated the catalytic converter using a series of completely mixed reactors [26]. This model became the basis upon which all other works in this area were derived [27]. Of pertinence to this paper, they simulated hydrocarbon species as two individual species with different reactivity over the catalyst; slow oxidizing and fast oxidizing. They characterized the slow oxidizing species using methane (CH_4) and fast oxidizing species via propene (C_3H_6). For nearly two decades, this remained the de facto standard with a change occurring in the early 1990s as propane (C_3H_8) replaced methane as the slow oxidizing species, with methane then considered to be an inert hydrocarbon [28-31]. This was a reasonable assumption because EPA's HC emission standards at the time consisted of regulations involving only total hydrocarbon (THC) and non-methane hydrocarbon (NMHC) emissions. Moreover, around the same time frame, foreign governments passed other generalized THC-targeting pieces of legislation [32]. Furthermore, HC reactivity over catalysts could be readily lumped into these regimes as illustrated by Adams et al. [33] in Figure 1.

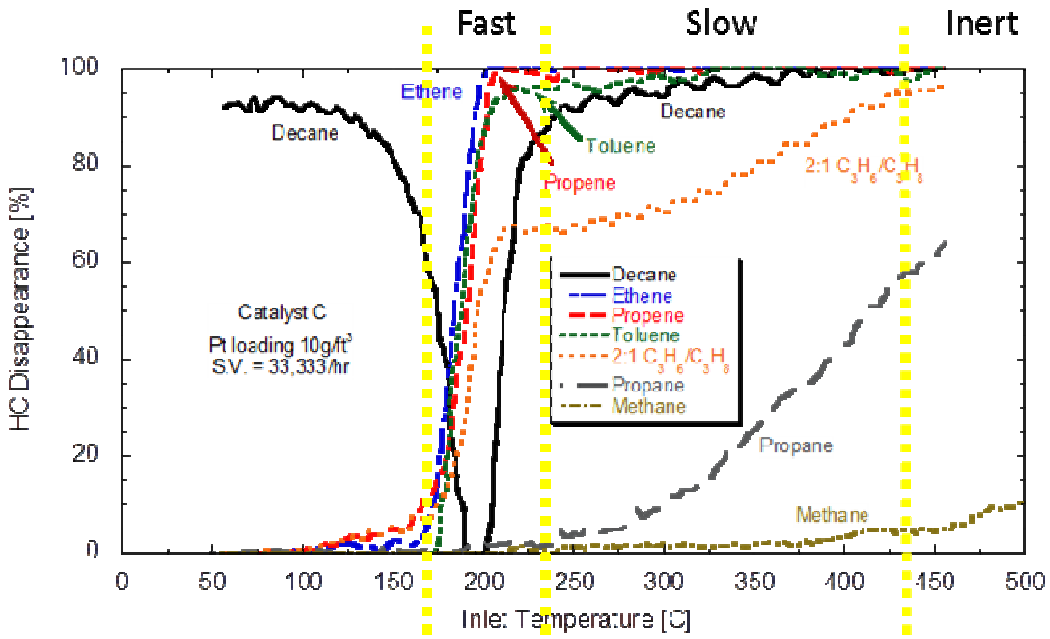

Figure 1. Conversion of different HC species as function of temperature over a Diesel Oxidation Catalyst [33].

However, future EPA regulatory efforts may seek to lower specific HCs based on the potential risks associated with those species. The current focus is a group of HCs and metal compounds known as mobile source air toxics (MSAT). These 21 compounds (or compound groups) listed in Table 1 are extremely hazardous [9]. The MSAT compounds draw from various groups of emissions species. A sizeable portion is from the emissions of metallic compounds, which can be caused by fuel additives, or from impurities in mineral sources [9]. The dioxin/furans category refers to the shorthand notation for polychlorinated dibenzodioxins produced by the combustion of organic compounds with chlorine [34]. The use of methyl tertiary butyl ether (MTBE) as an anti-knock agent in gasoline fuels lead to emissions from the unburned remains of this fuel additive [35]. The remaining compounds form the core of the most volatile HC emissions in compression ignition (CI) engines [9].

Table 1. Alphabetized list of MSAT compounds targeted by the EPA [9].

Acetalydehyde	Dioxin/Furans	Methyl Tertiary Butyl Ether
Acrolein	Ethylbenzene	Naphthalene
Arsenic Compounds	Formaldehyde	Nickel Compounds
Benzene	n-Hexane	PAH/NPAH Compounds
1,3-Butadiene	Lead Compounds	Styrene
Chromium Compounds	Manganese Compounds	Toluene
Diesel PM and Organic Gases	Mercury Compounds	Xylene

One potential avenue for reducing these HC emissions is through the implementation of alternative fuels. Researchers worldwide have developed biodiesel fuels based on different feedstock sources as an alternative to petroleum based diesel fuel. One of the benefits of utilizing biodiesel fuels is the decreased THC emissions [36, 37]. However, while switching fuels might reduce many HC species, the production rates of a few species may be largely unaffected by the change. Moreover, the combustion of biodiesel leads to additional HC species that do not appear in the emissions from conventional petroleum diesel combustion [7, 8]. Furthermore, some biodiesel fuels and fuel blends have shown increased THC emissions over conventional diesel fuels under certain circumstances [38]. This change in the HC emissions profile may necessitate a new generation of catalytic devices that can handle the variation in biodiesel emission species, while still being able to function correctly with conventional diesel exhaust.

Based on this discussion, this paper provides a review of HC species in the exhaust of CI engines in order to understand specific groupings of HCs. This will provide a methodology for breaking up the hundreds of different exhaust HC species into an easier to digest format for analysis. Then, a recap of biodiesel combustion literature will illustrate the change in the HC species profile in order to determine reductions in certain groupings and the possible inclusion of new classes. A discussion involving different measurement techniques will follow documenting how to measure these groupings for both engine and catalytic aftertreatment analysis. This leads into the postulation of a new methodology for modeling HC compounds, which can serve as the groundwork for the simulation of exhaust aftertreatment devices in advance of potential EPA regulations in the near future.

2.3 Hydrocarbons

The sub-grouping of HC emissions from diesel combustion largely follows via vapor phase HCs, polycyclic aromatic hydrocarbons (PAHs), nitro-polycyclic aromatic hydrocarbons (NPAHs), and heavy hydrocarbons (HHCs). In addition, the literature often treats other compounds such as alcohols, ketones, and aldehydes as hydrocarbons even though they contain atoms other than hydrogen and carbon. Some of these compounds, such as vapor phase HCs, appear in both diesel and biodiesel emissions. However, the use of biodiesel will generally reduce a few HC groups, particularly PAHs and NPAHs. Furthermore, many HCs (especially alcohols) lack the stability to remain in emissions and only show up as trace molecules, if they appear at all [9]. The following sections discuss these different HC compounds in order to document the specific compounds present in CI engine emissions. Additionally, the impacts of these emissions on human health and the environment are presented to thoroughly describe all aspects of HC emissions. This description helps provide the context needed to qualitatively rank the differing HC families with respect to their shared dangers in addition to the known methods needed to mitigate them through aftertreatment techniques.

2.3.1 Vapor Phase Hydrocarbons

Vapor phase HCs are a general type of HC emission species produced that can be divided into their own families of alkanes (e.g., methane), alkenes (e.g., butene), alkynes (e.g., propyne), and others. While all HC emissions have a certain risk associated with them, the types of threats from vapor phase HCs are as diverse as the family itself. For example, methane is produced under certain conditions in diesel combustion, and is known to be a potent greenhouse gas [25]. However, methane is also quite benign to living tissue, and does not represent a direct threat to human life. Alternatively, benzene does not pose any threat to the atmosphere, but has been shown to be a potent carcinogen [21]. The vapor-phase HC emissions category can itself be broken down into a number of sub-categories, isolating certain groups of chemicals based on the nature of the threats they pose.

Combustion produces a number of HC emissions that are relatively stable in the atmosphere, most prominently in the form of stable alkanes. While these molecules are generally benign to human beings, this same stability lowers their reactivity. As a result, the stable HC emissions have been grouped as the slow oxidizing and inert HCs since the 1970s, and are relatively well understood [26]. Methane and propane have both been used as representatives of this group with respect to catalysis, and other stable hydrocarbons include ethane and hexane [28]. These species (most notably methane) are potent greenhouse gases (GHG). While most are non-toxic, some individual species can be harmful to human beings over long periods. One such species is n-hexane, which has well documented toxic effects, such as weakness and numbness in the extremities, with nerve damage and paralysis resulting from prolonged exposure [39]. As such, n-hexane is classified as an MSAT compound by the EPA [9].

The arrangement of hydrocarbon molecules often occurs as chains of carbon atoms bonded to each other with hydrogen atoms placed on empty bond locations. Sometimes these chains result in a ring of carbon with the end carbon atoms bonded to one another. This “cyclic” attribute is evident in the structure of a single-ring benzene molecule. In polycyclic compounds, there is more than one ring present [40]. The simplest form of these types is naphthalene, in which two benzene rings fuse together in order to share a common side. These ringed molecules frequently occur in organic compounds and are abundant in oil, coal, and tar. Understanding how these species react in the environment has been a common research topic in organic chemistry studies. The term aromatic refers to the stability caused by the electrons’ behavior on the rings of these cyclic molecules. Aromatic compounds are inherently very stable; in fact, they are more stable than theory first predicted [41]. This is due to the bonded structure and the resonance feature of electron delocalization. The complexity of polycyclic aromatic molecules is broad and requires much research; however, one can attribute their stability to shape, electron distributions, and resonance. Nitro-polycyclic aromatic hydrocarbons (NPAHs) are nearly identical to polycyclic aromatic hydrocarbons (PAHs) with the only difference being the inclusion of nitrogen in the compound. These compounds are toxic and carcinogenic in humans and animals [42]. Both compounds form during the combustion process of petroleum-based fuels and because of their toxicity, the EPA

targets their reduction as the first type of specific HC emissions regulated [9]. Finally, as these HC emissions tend towards larger, more complex molecules, they can be targeted for reduction through either catalytic aftertreatment, or alternatively through diesel particulate filters (DPF) [7, 8].

Another subset of the vapor phase HCs are a group of species known collectively as BTEX, named for the component species benzene, toluene, ethylbenzene, and xylene. These compounds are similar to the PAHs in stability, and their production comes from the recovery of aromatics derived from the catalytic reformation of naphtha in petroleum refineries. Additionally, all of the species within this classification build on the ring structure of benzene (as illustrated in Figure 2). From this base structure, one or more hydrogen atoms can be replaced with secondary "tail" structures that differentiate one BTEX species from another. While these secondary structures are somewhat easy to remove, the primary benzene ring is extremely stable. As a result, BTEX compounds will often change from one species to another, but will retain their benzene ring, and remain within the BTEX family. This stability leads to use of BTEX compounds in resins, adhesives, rubbers, explosives, polymers, and solvents. Additionally, the compounds have found their way into the automotive industry as a fuel additive in gasoline (increasing the octane number), and have been shown to be a significant component of diesel exhaust [43, 44]. All four compounds are in relatively high industry demand, and benzene leads the group as the fifteenth most common chemical produced within the US, with approximately 15 billion pounds produced in 1997 [22]. This demand results in a unique problem since their useful industrial qualities also cause them to be incredibly dangerous to human beings when released into the atmosphere or ground water supplies. In particular, these compounds have a high water solubility and, therefore, are highly mobile in ground water [22]. Seepage out of older fuel storage tanks, spills, and deliberate use of these compounds leads to contamination of aquifers, crops, and livestock. Additionally, other species exist that behave similarly to the BTEX compounds, all of which present various risks to human health. As a result of their dangers, the EPA classifies all four BTEX compounds, as well as the BTEX-like styrene and 1,3-butadiene, as MSAT compounds [9].

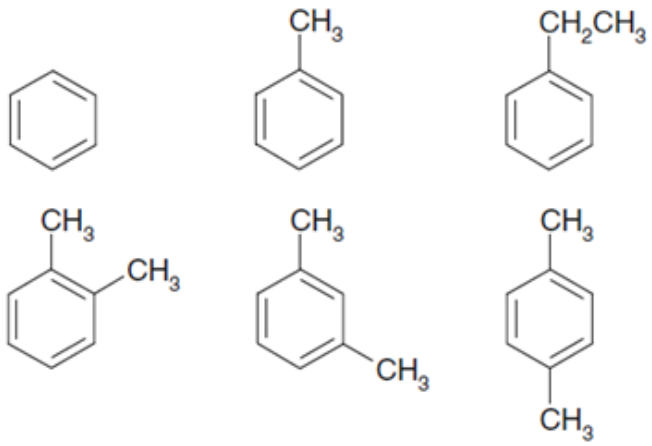

Figure 2. Examples of BTEX compounds, highlighting the benzene ring structure inherent to the group. Pictured clockwise from upper left; benzene, toluene, ethylbenzene, and three forms of xylene [45].

By far the most potent compound is benzene, a relatively simple vapor phase HC common to all automotive exhaust. Reports exist of benzene poisoning following exposure of less than 100 parts per million, and the American Petroleum Institute has stated that "the only absolutely safe concentration for benzene is zero" [21]. Accordingly, the EPA has limited the maximum contamination level (MCL) of benzene in drinking water supplies to five parts per billion [18]. Acute exposure has been linked to dizziness, headaches, apprehension, and increased heart rate [21]. Additionally, symptoms such as nervousness, irritability, and cardiovascular problems may last two to four weeks after exposure. Victims of benzene poisoning typically show an absence of blood clotting agents, and deaths from acute benzene exposure are usually the result of widespread hemorrhages throughout the body, including the brain. Chronic exposure has also been linked to various forms of cancer [21]. Other scenarios have led to heart, skin, or respiratory problems, as well as birth defects [19, 20]. Similar but lesser effects have been noted for ethylbenzene [46].

Toluene and xylene are both less dangerous than benzene, but both have unique health effects from long-term exposure. Neither species is thought to be carcinogenic, and both act as a substitute for benzene in dyes, paints, inks, and other household chemicals as an aerosol or solvent. Toluene enters the body primarily through digestion, decreasing the risk of exposure slightly. However, toluene can on

occasion enter the body through the skin or respiration. Conversely, xylene typically enters the body through respiration or the skin. Short-term exposure to either substance can cause irritation to the affected area, as well as dizziness and headaches. Prolonged exposure to toluene has been linked to damage to the nervous system, degeneration of respiratory tissue, and developmental disabilities in children [23]. Similarly, long term exposure to xylene has been shown to affect concentration, memory, vision, and muscle coordination [47]. Both substances can cause damage to the kidneys and liver.

2.3.2 Aldehydes and Ketones

The related organic components of aldehydes and ketones both develop during the combustion of diesel and biodiesel fuels. While not all pose a clear danger to human health, many that result from combustion can be quite damaging to living organisms. The primary aldehyde present in automotive exhaust is formaldehyde, a toxic and carcinogenic compound that accounts for 40-50% of aldehyde and ketone production in both diesel and biodiesel fuels [7, 8]. Short-term exposure leads to respiratory problems, as well as skin and eye irritation. Prolonged exposure can lead to cancer of the respiratory system [48]. Within the aldehyde and ketone grouping are the compounds acetone and acrolein. Exposure to either chemical can cause irritation and damage within the respiratory system, with acetone being a known carcinogen [49, 50]. While the EPA does not list acetone as an MSAT compound, this paper considers this prominent HC species to be closely related to the MSAT compounds.

2.3.3 Ozone Formation

While not a specific hydrocarbon, any discussion revolving around HC species emitted from IC engines must include a related examination of ozone. Ozone (O_3) is a gas comprised of three oxygen molecules covalently bonded. This naturally occurring chemical is present within the upper atmosphere and helps filter ultraviolet radiation from the sun. The protection this chemical provides at high altitudes is drastically different from how it behaves at ground level. Its presence at low altitude is due mainly to human activities, particularly those that involve the production of hydrocarbons. Some natural occurring ozone at ground level appears due to normal chemistry and transport from the ozone layer in the upper

atmosphere. However, man-made O_3 accounts for ten times the natural amount [51]. Illustrating the reasoning behind the EPA's regulatory efforts, many major U.S. cities are currently facing health and environmental problems associated with ground-level ozone; among these is the well-known smog problem [52].

Smog is a main issue caused by the burning of fossil fuels and is obvious in many cities across the country. The hazy cloud that commonly surrounds heavily industrialized and populated areas appears as a smoky fog, which is where it gets its name. The public attributes the various health concerns associated with living in these places largely to the ozone found in the haze; however, aerosols and particulate matter cause the visual component of the fog. Ozone is a severe irritant in smog, causing coughing, choking, throat irritation, congestion, and stinging eyes. It can damage lung tissue, aggravate respiratory diseases such as bronchitis, emphysema, and asthma and increase the susceptibility of people to contracting respiratory disease [53]. These risks are especially aggressive towards children and those with existing respiratory problems. Overall, it reduces lung function by damaging lung tissue and inflaming the linings of the lungs, and prolonged exposure has led to permanently scarred lung tissue. In addition to the health problems, ozone distresses public welfare and food supply. By interfering with sugar production and storage, ozone inhibits plant growth, damages crops and forests, negatively impacts the appearance of landscaping and impacts species diversity in ecosystems [53]. These problems for the population and ecosystems located around heavy-smog cities was one of the driving factors that lead to the founding of the EPA and assisted in setting up modern emissions control practices.

Ozone forms via a complex process involving multiple emissions species. The creation of ozone happens when particular volatile organic compounds (VOCs) interact with nitrogen oxides (NO_x) in the presence of sunlight. These VOC species are a class of HC compounds with drastically different toxicity and reactivity, as well as very high vapour pressures, which under normal circumstances allow significant vaporization into the atmosphere. Among these are aldehydes, ketones, and other light HC compounds [54]. Mainly excluded from this group are methane, ethane, acetone, and the less common types such as chlorohyrdocarbons.

Research confirms that ozone forms through NO_x precursors in the presence of sunlight and oxygen [52]. In particular, solar radiation and atmospheric heat break down NO_2 molecules by removing one oxygen molecule. This free oxygen atom joins atmospheric O_2 and forms ozone. This then reacts with NO to form NO_2 and atmospheric oxygen again. The creation and destruction of ozone results in low overall levels and is the result of chemical kinetics. However, the addition of volatile organic compounds permits the regeneration of NO_2 without destroying the ozone. In particular, when VOCs are present in the atmosphere, they react with hydroxyl (OH) radicals and add peroxy molecules (-OO) to the VOC chains. These VOC peroxide molecules react with NO to form NO_2 and oxygenated VOCs. This reaction replenishes NO_2 concentration, which decreases the destruction rate of NO and O_3. Figure 3 describes the overall mechanism illustrating that the addition of VOC reduces the frequency of the third reaction by eliminating NO and adding a second NO_2 production pathway [51].

$$NO_2 + sunlight \rightarrow NO + O$$
$$O + O_2 \rightarrow O_3$$
$$O_3 + NO \rightarrow O_2 + NO_2$$
$$VOC + OH + O_2 \rightarrow VOC \cdot OO + H_2O$$
$$VOC \cdot OO + NO \rightarrow VOC \cdot O + NO_2$$

Figure 3. Mechanism for the formation of ozone in a NOx and VOC environment [51].

With respect to VOCs, understanding their reactivity is necessary for developing a list of targeted HC species. The maximum incremental reactivity (MIR) scale is a tool developed by William Carter at the University of California-Riverside [55]. This scale pertains to the specific case when the reactions are VOC-limited and has become the standard for measuring reactivity. In the VOC-limited case, there is an excess of NO_x and/or low concentration of VOC resulting in the third reaction of Figure 3 being the main source for production of NO_2. This is commonly used near emissions sources, as downwind reactions move towards the VOC-limited condition [51]. The scale is a measure of grams of ozone produced on average per gram of specific HC. A second scale developed by Carter describes air pollution characteristics where a reduction in VOC and NO_x are equally beneficial. This scale calculates an equal benefit incremental reactivity (EBIR) without an excess of NO_x. For completeness, Table 2 and Table 3

present a selection of harmful VOCs, including the Chemical Abstracts Service labelling number, molecular weight, and MIR rating of common VOC compounds [55].

Table 2. Reactivity data for Volatile Organic Compounds, part I [55].

VOC	CAS #	g/mole	MIR*	EBIR**
1,2,4-trimethyl benzene	95-63-6	120.19	8.87	1.65
1,2-diacetyl benzene	704-00-7	162.19	2.25	0.33
1-butene	106-98-9	56.11	9.73	2.37
1-heptanol	111-70-6	116.2	1.84	0.59
2-ethyl-1-hexanol	104-76-7	130.23	2	0.58
2-heptanone	110-43-0	114.19	2.36	0.75
2-methyl pentane	107-83-5	86.18	1.5	0.57
2-nonanone	821-55-6	142.24	1.08	0.32
2-pentanol	6032-29-7	88.15	1.61	0.57
2-pentanone	107-87-9	86.13	2.81	0.89
3,7-dimethyl-1-octanol	106-21-8	158.28	1.2	0.34
3-methyl-1,2-butadiene	598-25-4	68.12	10.29	2.44
3-methylbutanal (isovaleraldehyde)	590-86-3	86.13	4.97	1.23
4-methyl-2-pentanone	108-10-1	100.16	3.88	1.08
acetaldehyde	75-07-0	44.05	6.54	1.61
acetone	67-64-1	58.08	0.36	0.089
alpha-pinene	80-56-8	136.23	4.51	0.89
beta-pinene	127-91-3	136.23	3.52	0.79
branched C5 alkenes		72.15	1.45	0.65
branched C6 alkenes		114.23	1.45	0.46
branched C8 alkenes		114.23	1.45	0.46
butanal	123-72-8	72.11	5.97	1.48
C10 alkenes		140.27	3.31	0.83
C10 disubstituted benzenes		134.22	5.68	0.91
C10 ketones		156.27	0.9	0.25
C6 ketones		100.16	3.14	0.99
C7 cyclic ketones		112.17	1.18	0.42
C8 cyclic ketones		126.2	1.05	0.37
C8 ketones		128.21	1.4	0.44

*Maximum Incremental Reactivity (MIR) based on VOC-limited [51]

**Equal Benefit Incremental Reactivity, beneficiary reduction, NO_x limited [51]

Table 3. Reactivity data for Volatile Organic Compounds, part II [55].

VOC	CAS #	g/mole	MIR*	EBIR**
camphene	79-92-5	136.23	4.51	0.89
camphor	76-22-2	152.23	0.49	0.129
crotonaldehyde	4170-30-3	70.09	9.39	1.94
dichlorobenzene	106-46-7	147	0.178	-0.042
d-limonene	5989-27-5	136.23	4.55	0.96
ethanol	64-17-5	46.07	1.53	0.59
ethylbenzene	100-41-4	106.17	3.04	0.5
ethyl cyclohexane	1678-91-7	112.21	1.47	0.45
formaldehyde	50-00-0	30.03	9.46	1.27
furan	110-00-9	68.07	9.15	2.06
heptanal	111-71-7	114.19	3.69	0.92
hexanal	66-25-1	100.16	4.35	1.1
hexenal	6789-80-6	98	4.35	1.1
isobutene	115-11-7	56.11	6.29	1.18
isopentane	78-78-4	72.15	1.45	0.65
isopropyl alcohol	67-63-0	60.1	0.61	0.25
linalool	78-70-6	156.27	5.43	1.07
methanol	67-56-1	32.04	0.67	0.19
methoxybenzene; anisole	100-66-3	108.14	6.66	1
monochlorobenzene	108-90-7	112.56	0.32	-0.074
n-heptane	142-82-5	100.2	1.07	0.39
nonanal	124-19-6	142	3.16	0.77
octanal	124-13-0	128.21	3.16	0.77
o-cymene; 1-methyl-2-(1-methylethyl) benzene	527-84-4	134.22	5.49	0.89
o-xylene	95-47-6	106.17	7.64	1.16
pentenal	1576-87-0	84	5.08	1.29
phenol	108-95-2	94.11	2.76	-0.85
propionaldehyde	123-38-6	58.08	7.08	1.75
styrene	100-42-5	104.15	1.73	-0.48
terpene (monoterpenes)		136.23	4.04	
terpinolene	586-62-9	136.23	6.36	1.18
toluene	108-88-3	92.14	4	0.52
trans-2,5-dimethyl 3-hexane	692-70-6	112.21	4.82	1.29
Trichlorobenzene	120-82-1	181.5	0.178	-0.042
trimethylbezene	95-63-6	120.19	8.87	1.65
α-terpineol	98-55-5	154.25	4.63	0.89

*Maximum Incremental Reactivity (MIR) based on VOC-limited [51]

**Equal Benefit Incremental Reactivity (EBIR), beneficiary reduction, NO_x limited [51]

2.3.4 Heavy Hydrocarbons

Heavy hydrocarbons (HHCs) are effectively the "remainder" of HCs that consist of many HC species that simply do not fit in the other sub-categories mentioned. Additionally, HHCs are unable to exist in a gaseous state at room temperature, reverting to a particulate form. As such, HHC species tend to blur the line between HCs and particulate emissions, and it is generally more expedient to reduce these emissions through DPF than through catalysis. HHCs typically consist of extremely complex molecules, some forming through combustion and some that are inherent to petroleum fuels. In either case, most HHCs are due to additives or impurities within mineral diesel fuel. Consequently, the combustion of biodiesel fuels will see greatly reduced HHC emissions, depending on the amount of impurities within the fuel. Many methyl ester acids are also included in this category, and are exclusive to biodiesels [7, 8]. These acids are generally considered by some to be benign, and have lower toxicities [8]. However, there is some debate as to whether or not these acids are carcinogenic [56].

2.4 Biodiesel Emissions

In a CI engine, the direct injection of fuel into the engine combustion chamber occurs largely during the compression stroke. While the actual timing of the injection event will change between engines (depending on engine loading, speed, etc…), the fuel will never have ample time to mix fully with the air in the cylinder, resulting a heterogeneous air-to-fuel ratio that ranges from infinite at the edges to near zero at the center of the injected fuel [3]. In this central fuel pocket, not enough air is present to allow for complete combustion, and therefore the fuel HCs at the center may not undergo complete oxidation. In the exhaust event, after a certain degree of late stage oxidation, the remaining HCs emanate from the engine, forming a large fraction of HC emissions. The change in HC profiles resulting from biodiesel combustion is due to the differing chemical composition of biodiesel fuels, the primary cause being the presence of oxygen within the fuel molecule, leading to a dissimilar combustion process [36]. The actual amount of oxygen depends on the individual species and the size of the molecule, but the composition of

oxygen is typically around 11% (by mass) [37, 57]. This oxygen embedded within the chemical composition of the fuel causes a significant change in the combustion process.

In a biodiesel-fueled engine, the oxygenated fuel mitigates the relatively low air-to-fuel ratio in the fuel pocket by introducing oxygen everywhere in the cylinder that the fuel is present. This, in turn, leads to more complete (although still not total) combustion of the fuel [3, 58]. The actual amount of THC emissions reduced by switching to biodiesel varies between fuels and engines. Soybean-based fuels have been shown to have an average THC reduction of 50-60%, with some authors demonstrating reductions of up to 75% [36, 59]. When using rapeseed oil based fuels, authors have found an average 50% reduction in THCs [36]. Tests of various biodiesel fuels by many authors have shown significant decreases in THC emissions when using neat (unblended) biodiesel fuels in CI engines, even with more exotic fuels such as coconut or bunge-seed oils [36, 57, 59-64]. The EPA itself has determined that switching to neat biodiesel can yield up to a 70% reduction in THC emissions [9]. Additionally, the EPA has found that the percentage reduction of THC emissions when switching to neat or blended biodiesel can be expressed as a function of the percentage of biodiesel in the fuel [9, 36].

Using neat biodiesel and biodiesel fuel blends is not a guarantee of decreased HC emissions. Research has shown it may even lead to increased total emissions, especially when using a low percentage of biodiesel in the fuel [65-67]. These findings highlight the difficulties in the prediction of emissions from diesel-biodiesel blends, and could be due to various qualities of biodiesel fuel (such as high viscosity or lower volatility) that exacerbate HC emissions when using low-percentage blends and vegetable oil-derived biodiesel [68]. Additionally, care must be taken in the measurement of HC emissions for higher percentage blends of biodiesel, as well as neat biodiesel, due to the potential for errors in the measurement of THCs; e.g., the amount of THC emissions produced often approach the limit of what can be accurately read by sensor equipment, and unstable combustion reactions can cause large deviations between cycles [3, 69]. Of the greatest importance for this study, the EPA determined that while the THC emissions are reduced, the mass ratio of toxic to non-toxic HCs can increase with higher percentages of biodiesel [9]. Furthermore, each type of biodiesel fuel is made from its own individual

feedstock source, which can cause significant deviations in chemistry from fuel to fuel [62]. Of particular importance is the degree of saturation of biodiesel, which can play a role in the exhaust emissions of biodiesel fuels [70].

2.4.1 Soybean-Derived Biodiesel

Soybean-derived biodiesel is one of the most popular forms of alternative diesel fuels in the US, primarily because it is the only biodiesel fuel available in sufficient commercial quantities. Regarding this biodiesel feedstock, the EPA tested both neat and blended versions targeting MSAT compounds. They found 11 of these species present in biodiesel exhaust with the others are caused largely by fuel additives or impurities in the mineral diesel fuel blended with biodiesel [9]. They subsequently grouped these eleven compounds into three tiers in Table 4 based on the consistency of the results from their testing.

Table 4. EPA MSAT Tier Assignments for Soybean Biodiesel [9].

Acetaldehyde	Tier 1	n-Hexane	Tier 2
Acrolein	Tier 2	Naphthalene	Tier 1
Benzene	Tier 3	Styrene	Tier 2
1,3-Butadiene	Tier 3	Toluene	Tier 3
Ethylbenzene	Tier 1	Xylene	Tier 1
Formaldehyde	Tier 1		

The first tier of MSATs consists of HC emissions that provide for estimation as a function of biodiesel percentage. In particular, all five of these species decrease as soybean-biodiesel percentage increases [9]. These findings are largely consistent with those of other authors [71]. The second tier of MSAT compounds included somewhat inconclusive data. Of the three in this category, acrolein and n-hexanes decrease slightly as biodiesel percentage increased. The remaining toxin in this category (styrene) demonstrated a possible increase with an added percentage of soybean-biodiesel [9]. The third tier of MSATs is composed of compounds with uncertain results. Butadiene emissions showed divergent trends throughout testing, but in general trended downward as biodiesel percentage increases. Benzene and toluene were the only two HC species that rejected categorization outright. While no experimental verification was given, the EPA report suggests that toluene emissions would stay reasonably constant as biodiesel percentage increased, and that benzene emissions should increase slightly [9]. Moreover,

authors are testing soybean-based biodiesel for THC emissions as a function of injection timing. Efforts by Northrop et al. showed that neat soybean biodiesel had significantly fewer THC emissions as the injection event was moved later after top dead center (ATDC) than US mineral diesel [72].

Other soybean oil-based biodiesel data captured by Sharp et al. illustrates a marked decrease in THCs when testing in three separate engines [8]. The first engine experiments show a reduction in vapor phase HCs by 60% along with a 30% decrease in net aldehyde emissions. PAHs were down almost 75%, consistent with findings by other authors [73]. Nitrofluorene and nitropyrene demonstrated a 90% reduction, with other NPAHs reduced to trace amounts. Testing over the two other engines found similar results. In regards to specific species of the vapor phase HCs, ethylene, acetylene, and butadiene all demonstrated a reduction of around 22%. However, the production of hexane increased, up from zero to almost 0.4 mg/hp-hour, with heptane demonstrating a similar increase. Dimethylpentane and methylcyclopentane increased significantly from zero to 0.27 mg/hp-hour. Benzene and toluene production seemed virtually unaffected by the change in fuels, with benzene production increasing in only a few engine tests.

Among aldehydes and ketones, many species showed large decreases in production [8]. However, emissions of formaldehyde were more resistant, as emissions fell by only 25-40% in each test, with other authors reporting either similar or worsened results [74]. Three-quarters of the total mass of VOCs were found to be formaldehyde, acetaldehyde, or acrolein. The ozone potential of the VOCs emitted varied between each engine tested with the emissions of neat biodiesel similar to the emissions of mineral diesel on each engine tested. The results for soybean oil-based biodiesel demonstrate a stark contrast in HHCs to diesel. Biodiesel combustion produced 95% less HHCs during the first engine test. In general, all of the HHCs produced in diesel combustion were almost completely absent during biodiesel combustion. However, the emissions captured during the biodiesel tests indicated the creation of methyl ester acids, which were not present during the diesel combustion trials.

2.4.2 Waste Cooking Oil-Derived Biodiesel

In comparison to soybean oil biodiesel, trials performed by Lea-Langton et al. have shown that using neat recycled oil (a mixture of various vegetable oils) for methyl ester biodiesel generally lowers overall PAH emissions [38]. However, the specific PAH species of fluoranthene and pyrene increase under low engine power experiments by 58.6% and 71.5%, respectively. Naphthalene and benzo(a)athracene both showed significant decreases for both high and low power tests. Anthracene decreases slightly, and the production of fluorene increased slightly, but both were near undetectable levels. Increasing the power output finds that this trend reverses for these particular species as they undergo a subsequent reduction.

Extensive testing by Chase et al. shows that recycled cooking oil has significantly reduced THC emissions from average drive cycles. During a 200,000-mile road test, average THC emissions were around 25% those of mineral diesel. However, average emissions of aldehydes and ketones were higher for the waste cooking oil-based fuel than for mineral diesel, with roughly 75% of the VOC emissions consisting of formaldehyde and acetaldehyde, as found by other authors [74]. Additionally, they found no meaningful amounts of aldehyde or ketone emissions in species larger than four carbon atoms in size, possibly indicating that the higher heat of combustion was more effective at breaking down the more complex species. PAH emissions decrease significantly, varying from 20-50% the emissions of mineral diesel fuel, depending on the species. Chrysene, benzo(a)anthracene, and benzo(g,h,i)perylene were found to be the largest of the PAH emission species. Total NPAH emissions were around 30% the levels in mineral diesel, with all species being driven close to near-immeasurable levels [75].

2.4.3 Rapeseed Oil-Derived Biodiesel

In addition to recycled oil, Lea-Langton et al. tested emissions as a function of rapeseed oil as the feedstock for methyl ester biodiesel [38]. The data gathered demonstrates that using neat rapeseed oil biodiesel reduces PAH emissions in the same fashion as neat recycled oil biodiesel. Similar to the recycled oil fuel, however, emissions for fluoranthene and pyrene were greater than mineral diesel at low

power, up 12.9% and 20.3%, respectively. Correspondingly, increasing power output reduced all measured PAH species to levels below those of diesel emissions. Anthracene and fluorene both showed virtually no change between neat rapeseed biodiesel and mineral diesel, but were already stretching the limits of the HC emissions analyzer's abilities. Benzo(a)anthracene showed a significant decrease at low power outputs, but increased slightly above diesel emissions at high power [38].

Aakko et al. have shown a net decrease in HC emissions by switching to neat rapeseed oil, but noted that formaldehyde emissions only decreased in blends of rapeseed oil, and not in neat rapeseed oil biodiesel, as corroborated by other researchers [73, 74]. Furthermore, neat rapeseed oil displayed some of the lowest PAH emissions across all fuels tested, at levels comparable to neat soybean oil-derived biodiesel, and around half the levels emitted by other fuels and blends [73]. NPAH emissions were too minute to be measured accurately, but were still believed to exist due to particular phenomenon occurring during later tests with catalysts.

2.4.4 Other Biodiesel Sources

Many other biodiesel sources exist, each with varying levels of HC speciation research associated with it. One of the more popular alternative biodiesel sources is jatropha oil methyl ester, which has shown up to a 58% reduction in THC emissions [64, 66, 76, 77]. Other exotic biodiesel sources such as bunge seed and karanja oil-based biodiesels have shown similar results. Additionally, both karanja and jatropha biodiesel have shown greatly reduced THC emissions at both high and low engine speeds [63, 77]. Researchers have also shown a decrease in THC emissions by switching to neat and blended biodiesels derived from animal fats, particularly at higher engine loads [78, 79]. However, these researchers also commented on the quality of biodiesel, with lower quality fuels producing more HCs, among other emissions [79].

2.5 Measurement Techniques

Before postulating a recommended HC model for exhaust aftertreatment modelling, it is pertinent to understand how to measure these different HC species in order to create an experimentally feasible

model. Modern labs employ many methods that detect the presence and concentration of different molecules. The industry standard for determination of the concentration of hydrocarbons is by a flame ionization detector (FID). This ionization detector functions by producing a current proportional to the concentration of solute HCs in the emission stream. The analyzer subjects carbon compounds, ionized in a hydrogen-air flame, to an electric field supplied by the detector. The resulting electric potential is directed toward an electrode, where an electrometer responds to the ionized molecules subsequently producing a very small current (on the order of 10^{-12} amps) that is then converted to a voltage, filtered, and analyzed [80]. This device measures the THC level using propane as the calibration gas while assuming that all of the HCs compounds react similarly to propane. Another use of this device is to measure the methane concentration, during which the calibration is set for methane. Subtracting this second measurement from the first involving propane allows the researcher to obtain the NMHC [81]. This procedure is done to obtain measurements for the fast oxidizing (NMHC = C_3H_6) and slow oxidizing (THC–NMHC = C_3H_8) species as outlined previously [26, 27]. Overall, the FID is a relatively simple, yet flexible tool that provides high sensitivity and a broad range of applications.

A relatively newer alternative to FID measurements is through a Fourier Transform Infrared (FTIR) spectrometer. The FTIR operates by passing a beam of infrared light through an emissions sample. Different molecules, and different molecular bonds, will absorb unique wavelengths within the infrared spectrum, and by measuring this absorbance the FTIR can give an interpretation of the chemical species present within the exhaust sample. The broad-spectrum analysis of the FTIR provides a quantitative measure of almost all species within the exhaust (including HCs), making it a valuable addition to exhaust emissions analysis. However, FID technology is still more widely used, partially due to the FTIR's inability to measure diatomic compounds (most importantly molecular nitrogen, oxygen, and hydrogen).
In order to compensate for the weaknesses of both the FID and FTIR systems, many researchers have chosen to combine the two into one system, allowing the FTIR to handle a broad analysis of the full sample, and focusing the FID on particular species, as well as for a measurement of THC content. Other devices have taken the combination of emissions analysis devices one step further, such as AVL's

SESAM-FTIR analyzer, which allows for the integration of an FID system, as well as a paramagnetic detector (PMD) that can measure the oxygen content of the emissions sample [82].

A gas chromatograph (GC) provides for further analysis of gaseous compounds. This device involves injecting and vaporizing a sample of the emissions mixture into a defined column. An inert carrier gas, such as helium or nitrogen, transports this vapor to the GC column. Within this column, the components separate, or partition, into groups of similar constituents and set up a microscopic liquid phase on an inert solid. This partition takes places between the carrier gas (mobile phase) and the boiling liquid (stationary phase). The compounds analyzed interact with the walls of the column causing the elution of the molecules, or extraction through a solvent. The device then calculates a residence time that the specific compound stays in the liquid phase before elution to the detector. Different chemicals have different retention times, which allow technicians to differentiate the specific species [83]. A GC study allows for analysis of the oxygenated components of the exhaust gases. This includes the aldehydes and alcohols, which tend to respond differently during ionization detection than the lumped propane approach in the FID. This method then provides a measure of the total organic gas (TOG) [81]. When subtracting the amounts of methane and ethane from this measure, the resulting fraction is a measure of the VOCs within the exhaust emissions.

The effectiveness of emissions measurement technology is of significant interest. HC emissions are already reduced to levels at the periphery of what can be measured (indeed, past EPA legislation limiting engine-out HCs went hand-in-hand with advances in GC technology) [9]. Indeed, while speciation of lighter HCs (most notably the BTEX species, as well as VOCs) can use GC or FID techniques, PAH and NPAH species have already been reduced to extremely low amounts, and therefore are difficult to measure directly [84]. As a result, PAH and NPAH analysis is frequently achieved through measurements of particulate emissions, along with HHCs and other non-HC particulates, through GC-mass spectrometry (GC-MS), which unify gaseous emissions analysis techniques with mass spectrometry of solid emissions components. The mass spectrometer functions by comparing the mass and electrical charge of particulates, categorizing them by their mass-to-charge ratio. When using any of these techniques, it can be difficult to

differentiate one species from another, so PAH/NPAH analysis methods often include a combination of measurements from both FID and GC-MS of particulate emissions [8, 85]. Since HHCs do not exist in a gaseous state at ambient conditions, an analysis can only occur through GC-MS of a particulate filter. Due to the massive amount of HHCs that typically exist in engine exhaust, it is often necessary to compare the spectra obtained by analysis to those within the spectral libraries of various research institutions. Even with these libraries, speciation is approximated, and so can only be used to compare HHC emissions between tests [7, 8]. Ultimately, correct speciation of engine-out HC species requires the combination of various techniques. A brief description of the techniques required for ideal speciation is provided in Table 5.

Table 5. Difficulty of measurement for various emissions groups through separate means.

Group	Difficulty of Measurement					Measurement Choice
	FID	FTIR	GC	GC-MS	Particle GC	
BTEX	Low	Low	Low	Low	N/A	GC, FID, or FTIR
VOC	Medium	Low	Low	Low	N/A	FTIR, GC, or GC-MS
Slow Oxidizers	Low	Medium	Medium	Medium	N/A	FID, calibrate for C_3H_8
Inert Emissions	Low	Medium	Medium	Medium	N/A	FID, calibrate for CH_4
THC	Low	Medium	Medium	Medium	N/A	FID
PAH/NPAH	Medium	High	High	High	Medium	FID and Particle GC
HHC	N/A	High	N/A	N/A	Medium	Particle GC

2.6 Hydrocarbon Model

After studying the EPA's concerns, as well as the known health risks and how to measure the different HC species, one can postulate the creation of new models for the control and simulation of diesel and biodiesel HC emissions across exhaust aftertreatment devices. The current model that groups the HCs into three categories in regards to how quickly they oxidize (fast, slow, and stable) is useful; however, this review illustrates that expanding the fast-oxidizing compounds fraction may result in better predictive efforts in future models. In order to avoid many of the complex non-linear equations needed to describe chemical kinetics, this effort categorizes the species simply into several groups, using attributes such as toxicity, reactivity, and catalytic behavior. Table 6 provides for this analysis, and is delineated by relative low, middle, and high dependencies on each category.

Table 6. Investigation into HC species delineated by low, middle, and high levels.

Group	Representative Species	GHG Potency	MIR Level	Health Hazard	Diesel Emissions	Biodiesel Emissions	Measuring Difficulty	Model?
BTEX	Benzene [C_6H_6]	Low	Low	High	Medium	Medium	Low	Yes
VOC Aldehydes	Formaldehyde [CH_2O]	Low	High	Medium	Low	Medium	Low	Yes
VOC Ketones	Acetone [C_3H_6O]	Low	Medium	Low	Low	Low	Medium	Maybe
Slow Oxidizers	Propane [C_3H_8]	High	Low	Low	Medium	Low	Low	Yes
Inert Emissions	Methane [CH_4]	High	Low	Low	Medium	Low	Low	Maybe
PAH NPAH	Napthalene [$C_{10}H_8$]	Low	Low	Medium	Low	Low	High	No
HHC - Diesel	C_{13}, C_{14}, C_{15} species	Low	Low	Medium	Medium	N/A	High	No
HHC - Biodiesel	Hexadecanoic FAME	Low	Low	Low	N/A	Low	Medium	No

The primary category takes the form of the BTEX compounds, along with a number of related compounds. Their separation is due to their unique reactivity and the specific strategies needed to eliminate them from engine exhaust. This category contains the most deadly of the aromatic compounds, and would ideally be used as a foundation for the control of emissions of benzene, toluene, ethylbenzene, xylene, styrene, and 1,3-butadiene. This would account for over half of the 11 MSAT compounds targeted by the EPA. It is recommended that benzene be used as the representative species for the BTEX group, due mainly to benzene being the most prevalent, and most dangerous, of the listed species. Additionally, the chemical makeup of many of the other species, namely toluene, xylene, and styrene, are reasonably similar to benzene, and may react in a similar manner over a catalytic converter. Since the BTEX category would be suitable for the control of many other aromatic compounds, it removes the need to model more complex compounds, such as styrene. However, as aromatic compounds are all notoriously difficult to control, further expansion into modeling of aromatic compounds is justifiable.

The second category seeks to control the VOC compounds, limiting the emissions of a number of compounds responsible for various environmental and biological threats. Ideally, this category would target many aldehyde and ketone species created during combustion. Specifically, this should include formaldehyde, acetaldehyde, and acrolein; thereby, nullifying three MSAT compounds, as well as acetone.

Additionally, this category can target the production of ozone-harming HCs. The representatives of these groups are formaldehyde (for aldehydes) and acetone (for ketones), due to the fact that they are the simplest (and therefore, the most likely) chemical examples of each type. In this category, one could expand the modeling to separate aldehyde and ketone HCs. However, the modeling of only one of the two categories should be sufficient to control emissions of the other category due to the similarities between the two groups. To this end, modeling of aldehydes through formaldehyde can remove the need to model ketones. The choice of aldehydes is due to their slightly increased biological dangers, as well as their (relative) ease of measurement.

The final categories include the slow and non-oxidizing compounds. Propane remains as a representative species, owing to its exceptional stability and widespread usage in current models along with available emissions analyzers. Researchers can additionally use this category in order to mitigate the production of n-hexanes, accounting for one MSAT compound group. Unlike the previous categories, this targeting of the slow oxidizing compounds is due largely to their environmental effects, although many sub-species (such as n-hexanes) do present a degree of danger to biological systems. Additionally, methane is included as a measure of the inert, non-oxidizing gases. These species are largely unaffected by catalysis, and so modeling of these species is often unneeded with respect to the construction of future catalysis models. However, future regulations of GHG emissions may warrant revisiting this assumption in order to create a more complete aftertreatment model.

PAH/NPAH emissions may lie outside the previously listed categories. While one can mitigate aromatic emissions by catalytic aftertreatment, they also are large enough for DPF devices to reduce. As a result, reduction in PAH emissions often occur through a combination of both techniques. Additionally, HHC emissions are almost exclusively diminished through DPFs, reducing the requirements being forced upon the catalytic device [7, 8]. The authors recommend that both PAH/NPAH emissions and HHCs not be modeled (at least initially) in future efforts using the presented methodology. As newer catalytic models are developed, PAH emissions could be targeted, but should not come at the expense of BTEX and VOC emissions. In the event that the modeling of PAH emissions is found to be necessary,

naphthalene is recommended as the representative species, as research has shown it to be the most prevalent of the PAH species, and therefore the highest likelihood to affect humans and the environment. If HHC emissions are to be targeted, the models should be focused on C_{13} n-tridecane, C_{14} n-tetradecane, and C_{15} n-pentadecane, as these species represent the greatest portion of HHC species [8].

With respect to neat biodiesel emissions, newer catalysts will encounter lowered THC emissions, but slightly increased emissions in the BTEX and VOC groups. More troublingly, the BTEX and VOC groups will most likely consolidate towards the simpler and more stable molecules of the two groups, namely benzene and formaldehyde. HHC emissions present an interesting challenge, as the diesel HHC species are replaced with an entirely new set of methyl ester acids, and could potentially need their own category, modeled by one of the more common species such as hexadecanoic acid methyl ester. However, methyl ester acids are produced at extremely low levels, and so may not warrant attention. Accordingly, the catalyst model could neglect other emissions categories, or even model both sub-groups of VOC species. However, such a catalyst would be unable to effectively control emissions from mineral diesel (or diesel-biodiesel blends), and so would only be suitable for an engine fueled exclusively on neat biodiesel fuels. A catalytic aftertreatment device that would be able to control diesel, biodiesel, *and* blended fuels is the obvious goal, but may be difficult to model and construct.

2.7 Conclusions

The methodology described in this paper serves as a means to improve upon current HC oxidation simulation strategies, and is based on EPA concerns along with the chemical properties of those species produced in diesel and biodiesel-fueled engines. This expansion subdivides the fast oxidizing HC emissions into multiple species, in order to control different groups of emissions more effectively. However, for this methodology to be useable, one must take into account a number of different factors.

First, while analysis techniques exist for measuring each of the HC species, some emissions analyzers are reaching their limit in their measurement of HC emissions. In particular, emissions analyzers often measure THC and NMHC emissions only. Furthermore, the decreased THC emissions of

biodiesel fuel may lead to incorrect measurements altogether. These limitations together necessitate the use of a combination of multiple emissions analysis techniques, including FTIR, FID, and GC analysis. Additionally, the catalytic reactivity of each species of interest mentioned must now be ascertained. Results have been given by other authors, but more research will be needed in this area [8, 38, 86]. Ultimately, any research in this area must first overcome the limitations of present technology, especially when dealing with biodiesel HC emissions.

In particular, biodiesel emissions pose a unique challenge to future models. While the combustion of neat biodiesel will see lower THC emissions, testing has shown that certain species are unaffected by the change in fuels, and some species (such as benzene and formaldehyde) increase in production under certain circumstances, particularly in blends. This challenge is of significant concern because these same species currently resist catalytic aftertreatment techniques.

Next, this effort requires follow-up work reviewing the HC emissions of gasoline and ethanol-fueled engines. Vast differences in chemistry and the combustion cycle may lead to a new set of representative HC emissions from these fuels. Furthermore, a change in fuel additives (such as the addition of MTBE to gasoline) may lead to further changes in HC emissions.

Finally, the generic labeling of biodiesel fuels means that any one engine must function on available biodiesel fuel supplies. This necessitates a “one size fits all” catalytic device that must be open to a consumer's preference (or lack thereof) for certain biodiesel fuels over others, or with respect to conventional diesel and/or blends. Most likely, designing an economical catalyst that could actively keep THC emissions down, combat the specific HCs that the EPA (or the more proactive California Air Resources Board) wishes to nullify, *and* function effectively given any type of biodiesel, petroleum-based diesel, or fuel blend could be difficult to achieve.

Overall, the models built upon the presented methodology should include oxidation sites designed for better aftertreatment of various VOCs and propane. Additional layers of hydrogenation and aromatic oxidation substrates will optimize the system in a more efficient manner. By designing each layer of the washcoat of the catalyst to combat each of the three groups specifically, optimal diffusion, heat transfer,

and reactivity characteristics can be achieved. This more optimized catalyst model should allow for better command of which reactions occur, controlling overall emission levels of HCs.

Chapter III: Equilibrium Heat Release Model as an Extension of Emissions Analysis of Direct Injection Compression Ignition Engines

Jonathan M. S. Mattson*[1], Christopher Depcik[1]

[1] University of Kansas, Department of Mechanical Engineering

* Corresponding author: jmsmattson@gmail.com

3.1 Abstract

The heat release analysis of an internal combustion engine is essential for understanding the process of combustion, and such models are commonly used tools during engine testing. This effort describes a zero-dimensional (0-D) three-zone model (burned, unburned, and fuel mass zones) for computing the rate of heat release using in-cylinder pressure-time history. Each zone is thermodynamically independent except for the shared use of the pressure trace. By utilizing fundamental mass and energy balances including Exhaust Gas Recirculation and engine turbocharging, the model balances numerical accuracy with time-efficient computation. The model utilizes established ignition delays, as well as known indicators for the onset of combustion. The model includes a methodology for diagnosing ignition delay from both Arrhenius-based functions and pressure trace indications. Improvements to the literature in this area include the incorporation of an Arrhenius-based function for the rate of combustion, freeing the user from needing to diagnose the duration of the combustion event. The model is calibrated to a combustion efficiency gained through a separate emissions analysis, providing a stable platform to calculate the rate of heat release. Model results demonstrate the rate of heat release of various fuel chemistries (mineral diesels, oxygenates, and other fuels) utilizing pressure data acquired from the testing of a single-cylinder compression ignition engine.

3.2 Introduction

Analysis of the combustion process within an internal combustion (IC) engine is essential to engine research. Two distinct techniques exist in order to characterize combustion. The first is a measurement of emissions species, whereby quantifying exhaust gases allows for calculation of the

degree of combustion within the cylinder. The second is a combustion model, used to calculate various thermodynamic characteristics throughout the engine's thermodynamic cycle. One of the primary tools used by researchers for this analysis is a Heat Release (HR) model [87]. The diagnostic HR model functions by calculating the total energy released by the combustion of fuel based on the measurement of in-cylinder pressure [87, 88]. In regards to the specifics of the HR model, there is a wide divergence in available models.

The number of "dimensions" used (*m*), as well as the number of "zones" (*n*) that make up a distinct portion of the control volume often characterizes a HR model [87]. As such, designation of HR models often follows the "*m*-dimensional, *n*-zone" nomenclature. The dimension characteristic refers to number of spatial dimensions used to characterize the movement and evolution of events within the cylinder, in addition to time. For example, a zero-dimensional (0-D) model ignores all geometry within the cylinder (other than the volume and surface area), and the properties within the cylinder only change as a function of time. Of importance, higher dimensional models (often computational fluid dynamics (CFD) based) see greatly increased accuracy when quantifying the energy output of fuels [89, 90]. However, these added dependencies on space introduce a large number of equations (primarily through the balance of momentum), at the cost of greatly increased computational time. In contrast, 0-D models neglect spatial dimensions, leading to low computational cost. As a result, 0-D models are favored when computational speed is a concern, and some are able to provide results in real-time in real-time [91]. The number of "zones" (*n*) within the model refers to the separation of the volume within the cylinder at any given time into multiple smaller volumes, each with its own thermodynamic qualities. The number of zones can range widely, from only three or four (in the case of 0-D models) to hundreds or thousands (for CFD programs), with the reasoning behind separating the zones varying as well. Additional zones are often required in order to model certain in-cylinder phenomenon (such as blow-by effects, or fuel stratification in DI engines), and lead to increased accuracy in modeling with only a slight increase in computational time [87].

Within the 0-D modeling group are two main versions of HR programs: those that incorporate a balance of the First Law of Thermodynamics, and those that calculate HR from equilibrium of the cylinder contents [3, 87]. First Law HR models include the summation of the individual components of heat release; namely work, internal energy, heat transfer, and other effects such as blow-by and injection. They often use a single zone, and calculate the rate of change of the energy flowing into or out of the cylinder, as well as the change in energy remaining within the cylinder [88]. By summing the rate of change of the energy components, these models calculate the total rate of heat release (RHR) of the control volume and are constrained by setting the RHR equal to the rate of combustion of fuel. As a result, First Law models must express the mass fraction of fuel burned for a given crank angle as a function of pressure and volume [92-95]. The most prominent model is the Wiebe function, which sets the mass fraction burned equal to an exponential curve [96, 97]. A similar model was developed by Matekunas et al., using the ratio of the pressure of the engine cycle and the normalized motoring pressure curve of the same engine [98]. If the combustion efficiency and mass flow rate of fuel are known, the RHR and cumulative HR can be solved from the mass fraction of fuel burned [95]. However, both models require a known beginning and end of combustion that may not necessarily be available from the model, and can lead to problems in some compression ignition (CI) engines that experience prolonged combustion events [95, 98-100]. These models are also hampered by instability caused by variations in the pressure trace, leading to some situations where the mass fraction burned is reduced or exceeds unity for portions of the engine cycle [88, 95, 101].

Equilibrium HR models calculate the change in energy within the control volume due to individual effects (e.g., work, injection, heat transfer, etc.), and then predict the HR by summing the components of energy being added or removed from the control volume [102]. They are closely related to First Law models; however, the RHR is not necessarily defined by the rate of mass fraction burned. Instead, the change in the mass of fuel burned is dependent on the varying pressure, temperature, and speciation of the zones (or the bulk gas). This is defined by the true RHR of the fuel itself, providing a more fundamental basis for the calculation of HR. As a result, these models are almost always subdivided

into zones in order to separate the mass of the control volume into groups, depending on their chemical composition (liquid fuels vs. gases) or origin (residual gases vs. intake species) [87, 88, 103]. Each zone has its own thermodynamic properties based on the constituent species contained within the zone. The number and nature of the zones is arbitrary based on what the modeler wishes to calculate within the combustion cycle. For example, a "fuel zone" is often added to allow for the calculation of fuel ignition delay or vaporization [87]. Alternatively, multiple "burned zones" for combusted material can be added, particularly in models wishing to predict emissions species [104]. The addition of multiple zones can lead to a large system of equations; hence, authors often make assumptions in the sharing of thermodynamic properties between the zones [103, 105]. While many variations of the Equilibrium HR model exist, virtually all of them use a shared value of pressure in all of the zones. This assumption is mainly due to the difficulties in measuring a pressure gradient within the cylinder [93, 94]. Equilibrium models can include the calculation of the ignition delay in the fuel zone as a function of the fuel properties at a given crank angle, primarily in the form of the Arrhenius rate expressions developed by Hiroyasu et al. [106-108]. A similar Arrhenius expression can be used for the rate of combustion, which provides an alternative to the Wiebe and Matekunas expressions. This is particularly useful for CI engines where the duration of combustion is unknown. Since the Arrhenius function is self-limiting, it will slow as the amount of fuel remaining in the cylinder decreases resulting in an effective combustion duration [88]. The function provided by Hiroyasu et al. also expresses the activation energy of the fuel as a constant value; hence, the reaction rates of different fuels are concentrated into a single term.

The model described herein is a 0-D HR model for direct injection (DI) CI engines, and was chosen for its relative simplicity and increased computational speed. The model is broken down into three distinct zones; an unburned zone constituting intake gases that have not undergone combustion, a fuel zone comprised entirely of unburned fuel, and a burned zone of the products of combustion, as well as gases that are entrained into the high-temperature combustion zone, but do not react chemically [87, 103]. As a result, the burned zone will not contain any molecular oxygen or fuel. While this does not occur in reality (unburned fuel and oxygen will be interspersed with combusted materials), the program makes this

assumption in order to simplify the numerical algorithms. The program does not require that all three zones exist together at all times within the cylinder, and the simulation can add or remove zones at any time. For example, for the first few degrees of the program (up to fuel injection), the model only includes the unburned zone. This is because fuel injection has yet to occur, precluding the existence of the other two zones. After injection, the fuel and unburned zones coexist without combusting for a brief period, before combustion commences and all three zones are evident.

Changes in the size and composition of each of the three zones are constrained by the conservation of mass and energy, as well as the ideal gas equation of state. Therefore, the mass and energy contained within each zone, as well as flowing between the zones, and entering and leaving the system must sum to zero at all times between the intake valve closing (IVC) and exhaust valve opening (EVO) events. Normally, all mass transfer between zones is neglected. The exception to this is the combustion process itself, where the mass of fuel and oxygen is transferred and transformed by combustion into the burned zone, along with the species entrained with oxygen from the unburned zone (e.g., water vapor, carbon monoxide and dioxide) and heated by the energy released by combustion. The speciation of this zone is controlled entirely by the amount of fuel burned at a given time, which in turn defines the amount of species entrained from the unburned zone. During combustion, the burned zone advances along the boundary between the fuel and unburned zones, conceptually separating the two zones as shown in Figure 4. Recall that this is a 0-D model; hence, the figure merely attempts to provide a graphical interpretation of what is occurring, not an accurate dimensional portrayal. The rate of combustion itself is controlled entirely through an Arrhenius-type equation, which models the reaction rate largely as a function of cylinder conditions and the species of fuel used in the cycle.

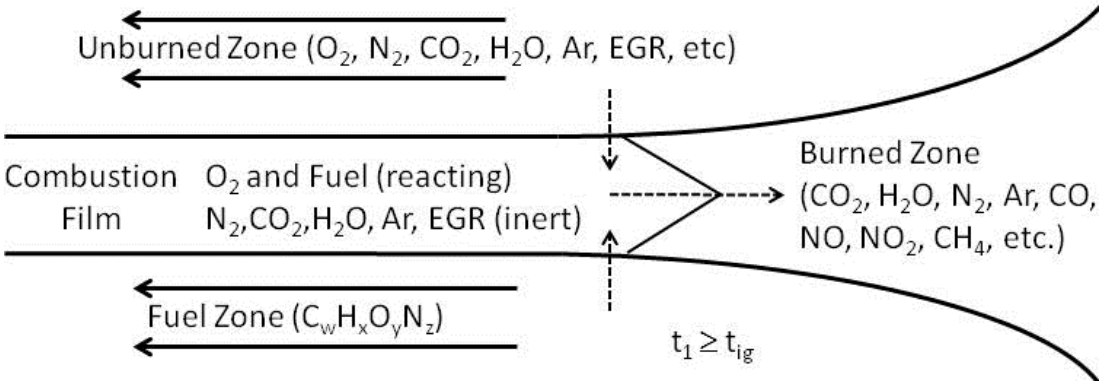

Figure 4. The separation of the three in-cylinder zones, occurring at an arbitrary time after the beginning of combustion.

At the end of combustion, subdivision of the in-cylinder volume results in a burned zone and any of a number of possible combinations of the fuel and unburned zones, with the burned zone separating the fuel and unburned zones as indicated in Figure 5, preventing further combustion. Since the amount of fuel or air typically limits combustion in an IC engine, it is entirely possible for either the fuel or the unburned zones to disappear entirely after consuming all available material. However, as complete combustion of is unlikely to occur, it is probable that all three zones will exist simultaneously at the end of combustion. Furthermore, a CI engine typically operates at equivalency ratios well below stoichiometry (with a surplus of air), and so the unburned zone is likely to compose a significant portion of the in-cylinder volume following combustion. A direct-injected spark ignition (DI-SI) engine would operate under conditions closer to (or above) stoichiometry. The model presented can allow for a DI-SI engine, but would require a new mechanism for combustion (replacing the unknown ignition delay with spark timing, and the addition of a mechanism for flame propagation).

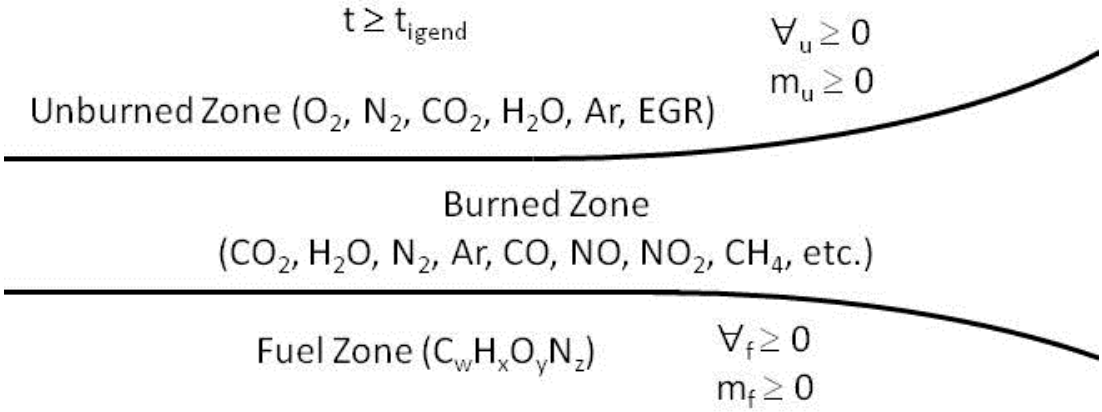

Figure 5. The conceptual separation of the three in-cylinder zones, occurring at an arbitrary time after the end of combustion.

The HR model presented herein is based on previous constructed Equilibrium HR models [103, 105]. However, the model does not constrain the change in temperature between zones before ignition, except through the conservation of energy. This is done in order to preserve the change in temperature of the fuel zone, which is thought to be critical to the calculation of ignition delay [107]. The program also makes use of an Arrhenius expression to simulate the ignition delay of the fuel. In contrast to previous work, the model is intended to be used as a complement to emissions analysis. As a result, the model is freed from needing to predict emissions except for those that would have a noticeable effect on the RHR of the system. A second Arrhenius expression is used to calculate the rate of the combustion reaction directly from the temperature indicated through the pressure trace, accounting for combustion through both premixed flames and diffusion. This expression is calibrated by using the measured combustion efficiency based on emissions analyzers. This increases the stability of the combustion reaction model and provides a realistic value for the fuel consumed at a given crank angle. Finally, the program is able to change between input fuels or fuel blends relatively easily, as only one variable in the Arrhenius expression must be adjusted. The following sections describe the model equations and its results for a wide variety of fuels and engine operating conditions.

3.3 Model Equations

The HR model builds on a number of separate simulation phenomena pertaining to the physics of combustion. The following sections state all assumptions made in the construction of the model for clarity, in the order that they are applied.

The primary equation used in the construction of any HR model is the First Law of Thermodynamics. Using this equation ensures that all energy moving into or out of the system, as well as the energy remaining within the system, is accounted for at all times. For the purpose of an HR model, the First Law is simplified to the following form:

Rate of Change of Heat Release with respect to time	$$\frac{dQ_{hr}}{dt} = \frac{dU_{cv}}{dt} + \frac{dW_{cv}}{dt} + \frac{dQ_{ht}}{dt} + \sum h \frac{dm_{cv}}{dt}$$	(1)

In this equation, the total RHR of the fuel (dQ_{hr}/dt) in the control volume due to combustion is found by summing the rate of change in internal energy (dU_{cv}/dt), the rate of change in work output (dW_{cv}/dt), and the rate of change in heat transfer (dQ_{ht}/dt), all with respect to time. Additionally, the rate of change in energy within the system due to mass flow into or out of the engine cylinder is included ($h \cdot dm_{cv}/dt$). For convenience, the work and heat transfer terms are defined with positive values indicating that energy is leaving the control volume, and the mass flow term is defined with positive values indicating that mass is entering the system. Since there are no sources of energy in the system other than those that come from combustion, or from mass flow, the solution of this equation will satisfy conservation of energy.

For a 0-D, three-zone model, a number of assumptions are made in order to simplify the conservation of energy. First, HR is only calculated when the cylinder is a closed control volume (e.g., no open valves); hence, any cylinder blow-by (or crevice flow) to the crankcase is neglected. In this situation, there is little mass flow into or out of the system with the only mass entering the system between IVC and EVO caused by the addition of fuel. In the authors' testing situation, the timing, duration, and magnitude of a single injection event are known; hence, the equations used to describe them (presented later) are

straightforward. As a result, the equations used to ensure the conservation of mass can be written only as being dependent on time only, as follows:

Change in mass with respect to time, before injection	$\frac{dm_{cv}}{dt} = 0 \quad t < t_{inj}$	(2)
Change in mass with respect to time, during injection	$\frac{dm_{cv}}{dt} = \frac{dm_{f,inj}}{dt} = \dot{m}_{f,inj} \quad t_{inj} \le t \le t_{injend}$	(3)
Change in mass with respect to time, after injection	$\frac{dm_{cv}}{dt} = 0 \quad t > t_{injend}$	(4)

where t_{inj} indicates the time in the thermodynamic cycle when fuel is injected, t_{injend} indicates the time when fuel injection has finished, and $\dot{m}_{f,inj}$ is the fuel injection rate of the injection event that can change as a function of time. Note that this effort can be expanded in order to account for multiple injection events.

Next, it is assumed that the engine crank angle (θ) is useable as a surrogate for time, allowing Equation 1 to be rewritten as a function of crank angle:

Rate of Change of Heat Release with respect to crank angle	$\frac{dQ_{hr}}{d\theta} = \frac{dU_{cv}}{d\theta} + \frac{dW_{cv}}{d\theta} + \frac{dQ_{ht}}{d\theta} + \sum h \frac{dm_{cv}}{d\theta}$	(5)

Within the program, the majority of the calculations follow this dependency on crank angle instead of time. However, some functions (such as the calculation of heat transfer coefficients) are calculated using a time dependency for convenience based on prior references, and must then be translated to a crank angle dependency. To enable this, the functional change in time with respect to crank angle is given by the following:

Change in time with respect to a change in crank angle	$\frac{dt}{d\theta} = \frac{t_{step}}{\Delta\theta}$	(6)

where t_{step} is the amount of time needed to step between crank angles indexed in the pressure trace, and is related the change in crank angle by the following relation:

Size of the functional time-step	$t_{step} = \Delta\theta \cdot \frac{1\,rev}{360°} \cdot \frac{1\,min}{N\,rev} \cdot \frac{60\,sec}{1\,min}$	(7)

where N is the average speed of the engine in revolutions per minute, and the remaining terms are for unit conversion only.

3.3.1 Components of the 1st Law of Thermodynamics

The first term on the right-hand side of Equation 5 represents the change in internal energy. For many HR programs, the change in internal energy is given in a form similar to the following [109]:

Rate of Change of Internal Energy within the Control Volume with respect to crank angle	$\frac{dU_{cv}}{d\theta} = m \cdot c_v \cdot \frac{dT}{d\theta}$	(8)

where m is the mass, c_v is the constant volume specific heat, and the remaining term is the change in temperature for the cylinder. This can be rewritten to describe the change in internal energy for a zone:

Rate of Change of Internal Energy within an Arbitrary Zone with respect to crank angle	$\frac{dU_i}{d\theta} = m_i \cdot c_{v,i} \cdot \frac{dT_i}{d\theta}$	(9)

where all the terms are now related to a specific zone, denoted by the subscript i (u-unburned, f-fuel, b-burned).

These models require three assumptions. The first assumption calls for the constant volume specific heat to remain constant throughout the entire cycle, which strictly speaking is never valid. Both constant volume and constant pressure specific heats are complex functions of many variables. However, the specific heats have been shown to be largely functions of temperature, and so have been correlated to functions of temperature. Additionally, large changes in temperature are required to produce significant variances in the constant volume specific heat, making the assumption of constant specific heat more viable for engine cycles with smaller changes in temperature.

The second assumption made in Equations 8 and 9 is that the mass within the cylinder does not change between IVC and EVO. On a cylinder-scale (i.e., single zone) model, the assumption holds so long as the change in internal energy from fuel injection and the loss of mass to the crankcase are both negligible. However, even in the case that mass is held constant within the cylinder volume, the

assumption fails during the combustion event for the three-zone model, as there is significant amounts of mass transfer between zones.

As a result, a separate description for the internal energy during the combustion event is required, in which the internal energy is defined as a function of mass, temperature, and constant volume specific heat. If all three variables are treated as being functions of crank angle, an alternative definition of the internal energy of a zone *i* is given that allows for mass transfer between zones, as well as changes in specific heat, by using the chain rule:

Full Expression for the Rate of Change of Internal Energy of a zone with respect to crank angle	$\frac{dU_i}{d\theta} = \left[\frac{\partial U_i}{\partial m_i}\frac{\partial m_i}{\partial \theta}\right]_{T,c_v} + \left[\frac{\partial U_i}{\partial T_i}\frac{\partial T_i}{\partial \theta}\right]_{m,c_v} + \left[\frac{\partial U_i}{\partial c_{v,i}}\frac{\partial c_{v,i}}{\partial \theta}\right]_{T,m}$ $\frac{dU_i}{d\theta} = T_i \cdot c_{v,i} \cdot \frac{dm_i}{d\theta} + m_i \cdot c_{v,i} \cdot \frac{dT_i}{d\theta} + T_i \cdot m_i \cdot \frac{dc_{v,i}}{d\theta}$	(10)

It can be seen that if there is no mass transfer between zones, and the change in constant volume specific heat is negligible, the first and last terms are reduced to zero, and Equation 10 simplifies back to Equation 9. From a practical perspective, the change in constant volume specific heat is quite small in comparison to the other two terms, but can still be significant for large changes in temperature (such as the beginning of combustion). It should be noted that Equation 10 does not provide for a mechanism to describe the complete change in energy due to a change of phase, which complicates the calculation of HR for a vaporizing fuel. The mechanism for this additional change in energy is calculated separately and presented later.

Once the internal energy of each zone is found, it is possible to determine the net change in internal energy by summing the change in each zone at a given time:

Functional Change of Internal Energy in the Control Volume with respect to crank angle	$\frac{dU_{cv}}{d\theta} = \sum \frac{dU_i}{d\theta} = \frac{dU_u}{d\theta} + \frac{dU_f}{d\theta} + \frac{dU_b}{d\theta}$	(11)

The internal energy is dependent on temperature, mass, and the specific types of species present within the cylinder. As a result, large changes in speciation and temperature will cause significant changes in internal energy, but may only affect a small portion of the total species present within the cylinder. As a

result, it is necessary to calculate the changes in internal energy of each individual zone, before calculating the summed change in internal energy at a given point in time.

The second term in Equation 5 represents the change in work with respect to crank angle described mathematically as follows:

Rate of Change of Work within the Control Volume with respect to crank angle	$\frac{dW_{cv}}{d\theta} = p\frac{d\forall_{cv}}{d\theta}$	(12)

where p is the pressure from a provided pressure trace, and $\forall_{cv}$ is the volume within the cylinder at a given crank angle from a geometric analysis of the engine, as described by Heywood [3]:

Total In-Cylinder Volume as a function of crank angle	$\forall_{cv} = \forall_{bowl} + \forall_{clear} + \frac{\pi b^2}{4}\cdot\left[c + r - r\cos\theta - \sqrt{c^2 - (r\sin\theta)^2}\right]$	(13)

where b is the bore, c is the length of the connecting rod, and r is the length of the crank arm. The terms $\forall_{bowl}$ and $\forall_{clear}$ are the volumes of the "bowl" feature within the piston head (if it has one) and the clearance volume of the cylinder, respectively.

Since both the pressure and volume are measured quantities, the work done by (or on) the control volume is generally the most accurate of the terms of Equation 5 within a single-zone model. With respect to any multi-zone model, however, each zone must have its own thermodynamic characteristics, and therefore its own value for pressure. In addition, the bulk gas within the cylinder must obey Pascal's Law, in that any change in pressure at any given point within the cylinder must be transmitted evenly throughout the rest of the cylinder. This change will not happen instantly, causing a temporary difference between locations in the cylinder. However, it is functionally difficult to measure this difference, impractical to differentiate from signal errors in measurement, and impossible to save during the process of pressure filtering. As a result, it is assumed that the value of pressure is constant at a given time for any location (and therefore any zone) within the cylinder [87, 103]. The change in work for a zone can then be described:

Rate of Change of Work within a Zone with respect to crank angle	$\frac{dW_i}{d\theta} = p\frac{d\forall_i}{d\theta}$	(14)

where the work and volume terms are now for a specific zone, denoted by the subscript *i*, and *p* is the shared cylinder pressure. Finally, the summation of the work done by the zones together must be equal to the work done by the control volume:

Functional Rate of Change of Work within the Control Volume with respect to crank angle	$\frac{dW_{cv}}{d\theta} = \sum \frac{dW_i}{d\theta} = p\left(\frac{d\forall_u}{d\theta} + \frac{d\forall_f}{d\theta} + \frac{d\forall_b}{d\theta}\right)$	(15)

The third term in Equation 5 represents the change in heat transfer with respect to crank angle. The mathematical description of heat transfer is given as:

Rate of Heat Transfer with respect to crank angle, general expression	$\frac{dQ_{ht}}{d\theta} = h_c \frac{dt}{d\theta} \cdot A_s \left(T_{cv} - T_w\right) + \sigma \frac{dt}{d\theta} \cdot A_s (\varepsilon_g T_{cv}^4 - \alpha_w T_w^4)$	(16)

where h_c is the convective heat transfer coefficient (in $W \cdot m^{-2} \cdot K^{-1}$), ε_g is the emissivity of the bulk gas, α_w is the absorptivity of the cylinder walls, T_{cv} is the average temperature within the cylinder factoring all three zones, T_w is the temperature of the cylinder walls (which is typically measured experimentally), A_s is the total surface area within the cylinder, σ is the Stefan-Boltzmann constant, and $dt/d\theta$ allows for conversion from watts (or J sec^{-1}) to J $degree^{-1}$. In this equation, the first expression on the right hand side represents convective heat transfer, while the second expression represents radiative heat transfer. Since the radiative portion is usually small (e.g., in the case of port fuel injected gasoline engines), it is occasionally neglected in favor of the much larger convective heat transfer term. However, in the case of CI engines, radiative heat transfer can be significant, and so cannot be neglected [109].

While the equation for heat transfer is agreed upon, the proper correlations for the coefficients (primarily those for the convective heat transfer and bulk gas emissivity) are not [110]. Several models exist for evaluating the coefficients, and authors have conducted studies on the validity of using certain coefficients over others [101, 109, 111-113]. The convective heat transfer coefficients used within the program are from correlations provided by Woschni and Hohenburg, which are the most widely used correlations in the literature due to their relative accuracy and ease of use [101, 110]. Additionally, many HR models allow for the calibration of the heat transfer coefficient, in order to account for all of the energy released by burning a known quantity of fuel [101].

The emissivity of the bulk gas is given as a function of temperature, pressure, and composition, and is necessary to find the rate of radiative heat transfer [114, 115]. Typically, the emissivity is tied to the amount of carbon dioxide and water vapor within the bulk gas, due to these species being the primary emitters of infrared radiation [116]. Within the HR program, the emissivity is correlated using a method by Bahadori et al. [117]:

Correlation for Exhaust Gas Emissivity	$\varepsilon_g = a_1 + a_2(p_g L_b) + a_3(p_g L_b)^2 + a_4(p_g L_b)^3$	(17)

where p_g is the combined partial pressures of water and carbon dioxide, a_1 through a_4 are coefficients dependant on the bulk gas temperature, and L_b is the mean beam length (or the characteristic length), which is dependent on the cylinder volume and surface area:

Characteristic Length or Beam Length within a Cylinder	$L_b = \forall_{cv} / A_s$	(18)

The surface area within the cylinder represents the total area through which heat is transferred, and is broken up into three major components:

Total Cylinder Surface Area	$A_s = A_{s,p} + A_{s,h} + A_{s,w}$	(19)

where $A_{s,p}$, $A_{s,h}$, and $A_{s,w}$ are the surface areas of the piston, the cylinder head, and the cylinder walls. The surface areas of the piston and cylinder head are assumed to be constant throughout the cycle, and must be measured to take into account the geometry of the surfaces. The area of the walls can be derived from Heywood's expression for the cylinder volume (Equation 13), and is given by the following:

Surface Area of the Swept Area of the Cylinder	$A_{s,w} = \pi \cdot b \cdot \left[c + r - r\cos\theta - \sqrt{c^2 - (r\sin\theta)^2} \right] + A_{wc}$	(20)

where the final value A_{wc} corresponds to the surface area of the walls of the clearance volume:

Surface Area of the Walls of the Clearance Volume	$A_{wc} = \frac{4 \cdot \forall_{clear}}{b}$	(21)

The radiative heat transfer to the engine cylinder walls is generally thought to be an important component of CI engine heat release. However, the rate of radiative heat transfer is overshadowed by convective heat transfer [111]. The importance of radiative heat transfer can be shown by evaluating the

Stark number (*Sk*), given as the ratio of convective (or conductive) heat transfer to heat transfer by radiation. The Stark number for the interior of a cylinder is given as follows [118]:

Definition of the Stark Number for Convection and Radiation	$$Sk = \frac{k_{wall}}{L_b \cdot \sigma \cdot \left(\varepsilon_g \cdot T_g^3\right)}$$	(22)

where k_{wall} is the thermal conductivity of the wall material. In general practice, if *Sk* falls below 10 during the combustion cycle, it indicates that the amount of heat transfer by radiation is significant, and so should not be ignored.

An important component of radiative heat transfer within internal combustion engines is the luminosity of the flame front and/or the soot formed during the combustion process. These can be lumped together into one term using a shape factor. However, in reality the flame luminosity will largely override the gas emissivity during combustion, allowing the rate of heat transfer (Equation 16) to be rewritten:

Rate of Radiative Heat Transfer	$$\frac{dQ_{ht}}{d\theta} = h_c \frac{dt}{d\theta} \cdot A_s \left(T_{cv} - T_w\right) + \sigma \frac{dt}{d\theta} \cdot A_s (\varepsilon_{fl} T_{fl}^4 - \alpha_w T_w^4)$$	(23)

where ε_{fl} and T_{fl} are the emissivity and temperature of the flame and burning particulates. Often, adiabatic flame temperature is used as a value for T_{fl}, and the emissivity is set to 0.6 [111]. Additionally, the computation of the Stark number will also change:

Functional Stark Number for Convection and Radiation	$$Sk = \frac{k_{wall}}{L_b \cdot \sigma \cdot \left(\varepsilon_{fl} \cdot T_{fl}^3\right)}$$	(24)

In effect, Equations 23 and 24 are used when the combustion flame exists within the cylinder. At all other times, the equations using the gas emissivity (Equations 16 and 22) are used, as there is no luminous flame to provide radiation.

The fourth and final term in Equation 5 represents changes in energy due to mass flow into or out of the control volume. By using the enthalpy of the mass entering or exiting the control volume, this term accounts for both the internal energy lost (or gained) and flow work done by (or on) the mass. The term can be used to represent various phenomena, such as the intake or exhaust events, crevice flow, or fuel injection. The amount of energy this term represents is greatly dependent on the HR model itself, the engine cycle, the method of fuel injection used, and the general state of the engine and its components. As

a result, the importance in the cumulative change in energy is extremely variable, ranging from significant to near negligible. In many models, this term is ignored, while in others, the term is either lumped with or assumed to be included in the calculation of heat transfer into (or out of) the control volume, particularly in models that calibrate the respective governing heat transfer coefficients.

For the model described herein, the fourth term in Equation 5 is generally neglected; there is assumed (almost) no change in mass, as the model only operates over the closed portion of the engine cycle, and crevice flow is neglected. The obvious exception is the change in mass due to fuel injection. While the components of the total release due to direct fuel injection are generally small (from a practical perspective), they are still important to consider. Additionally, the program models heat transfer through the cylinder walls separately from the change in energy due to fuel injection, allowing the user to differentiate between the two HR components.

Because the change in mass of the zones was presented earlier in Equation 10, the enthalpy term can be further simplified to specifically account for the energy needed to heat and vaporize the injected fuel:

Rate of Change of Enthalpy due to Fuel Injection	$\sum h \frac{dm_{cv}}{d\theta} = \left[h_{fg} + c_f \cdot (T_{vap} - T_{inj}) + c_{p,f} \cdot (T_f - T_{vap}) \right] \cdot \dot{m}_{f,inj}$	(25)

where h_{fg} is the enthalpy of vaporization of the fuel, T_{vap} is the temperature of vaporization (or flash point) of the fuel, T_{inj} is the temperature of the fuel at injection, T_f is the temperature of the fuel zone, c_f is the specific heat of the liquid fuel (correlated to an assumed injection temperature of 310 K), and $c_{p,f}$ is the constant pressure specific heat of the fuel (correlated to the current temperature of the fuel). This expression includes a few assumptions; one is that as fuel is injected, it is instantaneously raised to its vaporization temperature and subsequently vaporizes. Moreover, the change in enthalpy of the fuel as it heats up is expressed as the specific heat times the temperature difference, a reasonable assumption given the same standard state enthalpy. The model then accounts for the energy needed to bring the liquid fuel to its flash point, the energy needed to vaporize the fuel, and the energy required to bring the fuel vapor to

the current temperature of the fuel zone. At this point, any further changes in the temperature and energy of the contents of the fuel zone are controlled by the balance of internal energy (Equation 10).

3.3.2 Data Preparation

Of necessity to the HR program is the determination of precisely where top dead center (TDC) falls within the provided pressure trace. Authors have shown that an error of only one degree of crank angle can lead to a 20-25% error in the calculation of HR [119-122]. This error is normally mitigated by correctly setting up the radial encoder used to measure rotation of the crankshaft. However, encoder drift between tests can lead to a steady change of the timing of TDC across multiple tests. As a result, methods have been developed to ascertain the location of TDC within a provided pressure trace.

The first and simplest method is to set the peak value of motoring pressure trace to TDC (i.e., spinning the engine using a dynamometer without combustion), on the assumption that the point of minimum volume will also be the point of maximum pressure. However, this assumption is flawed due to the presence of thermodynamic losses around the geometric TDC. This error is primarily caused by heat transfer out of the engine cylinder, and is known as the thermodynamic loss angle (TLA) [119, 122, 123].

The second method implemented within this paper is to find the point of symmetry in the motoring pressure trace, while also taking possible heat transfer into account [119]. In this method, it is assumed that the pressure curves on either side of TDC are symmetrical for any given pair of points only when using the correct value of TDC. The expression for this correct offset of TDC from the measured value is written to include the effects of heat transfer:

Correction Value for Finding the true value of TDC	$\Delta_\theta = \left[p\big\|_{\theta_{TDC}-\theta_0} - p\big\|_{\theta_{TDC}+\theta_0} \right] \cdot \left[\frac{\forall\big\|_{\theta_0}}{\forall\big\|_{\theta_{TDC}+\theta}} \right]^\eta$	(26)

where θ_{TDC} is the crank angle at TDC, θ_0 is the offset crank angle, θ is an arbitrary crank angle, and η is used as a coefficient to allow for heat transfer.

In order to find the actual value of TDC, it is necessary to minimize the sum of squared errors between the upward (compression) and downward (expansion) slopes of the motoring curve in the vicinity of TDC during the closed portion of the engine cycle:

Sum of the Squared Errors between strokes	$\sum_{\theta_i}\left[p\big\vert_{\hat{\theta}_{TDC}-\theta_k} - p\big\vert_{\hat{\theta}_{TDC}+\theta_k} - \Delta\big\vert_{\hat{\theta}_{TDC}+\theta_k} \right]^2$	(27)

where $\hat{\theta}_{TDC}$ is a guessed value for TDC, and θ_k is a crank angle ranging between two arbitrary crank angles *a* and *b* on the downward slope of the motoring curve (and $-\theta_k$ are the corresponding values on the upward slope between the points -*a* and -*b*). By iteration, the value of $\hat{\theta}_{TDC}$ that minimizes Equation 27 can be found, resulting in an accurate approximation of TDC [119]. In general, the authors of the included reference suggest that the values of *a* and *b* be 30° and 115° after top dead center (ATDC), and that η be set to 1.1.

A third method involves the calculation of the entropy during the compression and expansion strokes of the motoring trace [123]. If it is assumed that the mass within the cylinder is constant during this portion of the cycle, and the mass flow rate of air into the engine is known, then the temperature of the cycle can be found by applying the ideal gas model to the motoring pressure trace. Additionally, the change in entropy (δS) at a time step can also be shown:

Change in Enthalpy	$\delta S = c_p \frac{\delta \forall_{cv}}{\forall_{cv}} + c_v \frac{\delta p}{p}$	(28)

where the values of $\delta\forall$ and δp are approximated as the slope of the known volume and pressure curves at a given point, and c_p and c_v are the specific heating values for constant pressure and volume, respectively. With this, the entropy (S) at a crank angle can be solved:

Total Enthalpy	$S = \delta S \cdot \Delta\theta$	(29)

From this, it is possible to plot a temperature-entropy (*T*-*S*) diagram. If the position of TDC is varied so that the pressure trace is shifted backwards or forwards, the *T*-*S* diagram must also shift. The referenced authors note that if the position of TDC is placed too far after the geometric TDC, a loop will appear in the *T*-*S* diagram (see Figure 6). According to the authors, if the position of TDC is adjusted

backwards until the loop disappears (forming a "point" at the shifted value of TDC), then the correct point of TDC will be a further 0.45° back in the cycle (see Figure 6) [123].

Between the second and third models presented, it is therefore possible to find the correct amount of phase lag between the peak value of the pressure trace from motoring and the location of geometric TDC. For testing of the HR model, the phase lag was calculated through a separate program, using the motoring curves of the engine. Using both of the methods presented, the thermodynamic loss angle was found to be two degrees of crank angle, and an additional error of half a degree of crank angle was found in the encoder reading.

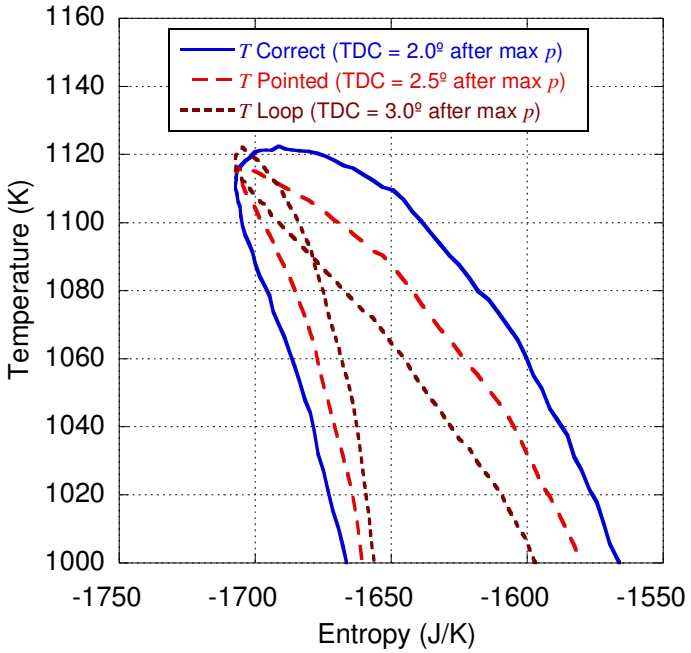

Figure 6. Temperature versus entropy diagram derived from the same pressure trace shifted to place TDC at various distances after the maximum pressure indicated by the pressure trace.

The next portion of the data preparation portion of the program is primarily concerned with reading in the pressure data used for calculating the combustion cycle while making it useable for analysis. Depending on the quality of the pressure transducer used, the data can be subject to noise at certain portions of the engine cycle. Figure 7 provides an example of "noisy" data during three situations; around IVC (at the bottom left of Figure 7, shortly before -100°), at the peak in pressure due to combustion just

after TDC, and at the intake valve opening (IVO) event (at the bottom right of Figure 7, corresponding to the second TDC reading, or +360°). Generally, the first and last components will not affect the calculation of HR, as IVC is well before combustion, and IVO is late enough as to be outside the modeled portion of the cycle. However, the noise during combustion can lead to large errors, particularly in the calculation of internal energy [124].

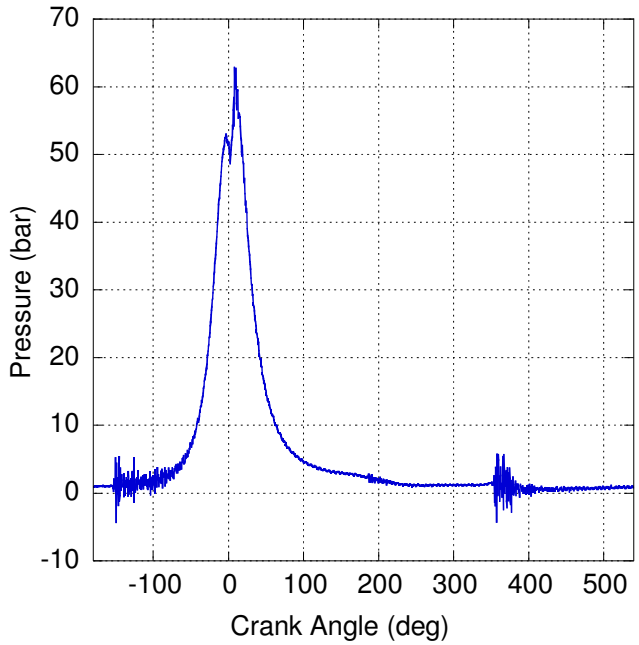

Figure 7. Unfiltered pressure data. Various phenomena can lead to poor readings at certain portions of the engine cycle, most prominently during combustion. Degrees are listed ATDC.

The first method in filtering the pressure trace is to compute an average trace. Data over a number of engine cycles (preferably 60 or more) is used to establish a tentative average for a particular crank angle [11]. If an individual pressure reading varies from the tentative profile by more than 25%, or is a negative value, the program assumes that the reading is an erroneous value, removing it from the profile. After removing these unwanted pressure traces, the program re-averages the remaining traces to calculate a cycle-to-cycle averaged pressure for that crank angle, before moving on. After filtering each data point individually, the program then filters the data points with respect to their neighbors. First, the program calculates a local average of the four data points surrounding any given point (two before, and two after). If any point is found to vary by more than 15% from the expected value given by the average, it is

replaced in favor of the local average. Finally, the program performs a rolling average of all of the data points.

In addition to filtering the pressure data, one of the first items accomplished is to declare all variables necessary to the main function along with preparing any other information needed in the computational portion of the code. In particular, after the fuel, engine, and test data are read, the program calculates a number of required variables, including the change in time and crank angle between data points. A number of storage matrices are created, and the molecular weights of all in-cylinder species are defined (in kg per mole). Particular events of note (such as the beginning of injection, IVC, and EVO) are translated from a known crank angle degree to an indexed point. The program also solves for the mass added in the injection event while cataloging the end of injection and the total mass of fuel added. Furthermore, the program reads in data needed for the enthalpy calculations of all in-cylinder species.

3.3.3 Ideal Gas Approximation

The primary assumption of the model is that the properties of mass within the engine cylinder evolve as a function of time only. This assumption greatly simplifies the continuity equations, particularly by removing the conservation of momentum from the model [87, 103]. Additionally, the model operates with up to three zones within the cylinder at any one time as discussed prior. The limit of the volume of each zone is dependent on the size of the other volumes, and the actual volume within the cylinder. The volumes of the three zones (indicated by the subscript *i*) must sum to the total volume in-cylinder at all times:

Relation between Zone Volumes and Control Volume	$\forall_{cv} = \forall_u + \forall_f + \forall_b = \sum \forall_i$	(30)

As a result, the change in volume over time can be easily linked to the change in volume of each of the zones:

Relation between change in Zone Volumes and Control Volume	$\frac{d\forall_{cv}}{d\theta} = \frac{d\forall_u}{d\theta} + \frac{d\forall_f}{d\theta} + \frac{d\forall_b}{d\theta} = \sum \frac{d\forall_i}{d\theta}$	(31)

The unburned zone ($\forall_u$) contains the unburned air mass from the engine's intake cycle, as well as both residual (left over from the previous cycle) and external EGR species with the percentage of EGR specified by the user. Before the injection of fuel, the unburned zone takes up the entire volume of the cylinder. At the point of fuel injection, the fuel zone ($\forall_f$) comes into existence. After a subsequent ignition delay, discussed later, the burned zone ($\forall_b$) appears and expands with respect to time. Each zone has its own mass and volume, as well as its own set of constants (specific heats, gas constants, etc…) in a manner similar to the single-zone model formulated by Lapuerta et al. [103, 109]. However, in order to turn the single-zone model into a three-zone model, it is necessary to track the individual temperatures of each zone.

Within the cylinder, all species present are treated as ideal gases, and each zone uses the ideal gas model as a constraint:

Ideal Gas Approximation	$p\forall_i = m_i R_i T_i = n_i R_{univ} T_i$	(32)

With pressure as the known value, it becomes necessary to solve for the mass within a zone (m_i), the associated gas constant of the zone (R_i), and the temperature (T_i) and volume of the zones, respectively. In some situations, the molar form of the ideal gas model is more appropriate (most prominently during combustion), and so the moles of material present (n_i) and the universal gas constant (R_{univ}) are used in place of m_i and R_i. From a known mass and volume, the density within a zone (ρ_i) can be solved using:

Definition of Density	$\rho_i = m_i / \forall_i$	(33)

In order to describe the contents of each zone, it is necessary to break up the zones into their constituent chemical species, and so the subscript *j* is used to indicate an arbitrary species. Calculation of the gas constant of species *j* within zone *i* utilizes the molecular weight of that species (W_j) and the universal gas constant:

Mass-specific Gas Constant of a single Species	$R_{j,i} = R_{univ} / W_j$	(34)

From this, the gas constant of zone *i* is solvable as a mass-based average of all of the species confined to a particular zone:

Mass-specific Gas Constant of a single Zone	$R_i = \frac{\Sigma R_{j,i} \cdot m_{j,i}}{\Sigma m_{j,i}} = \frac{\Sigma R_{j,i} \cdot m_{j,i}}{m_i}$	(35)

where $R_{j,i}$ and $m_{j,i}$ are the gas constant and mass of a certain species j within zone i. Finally, the bulk gas constant can be found by a mass-average of the three gas constants.

Mass-specific Gas Constant of a the Control Volume	$R_{cv} = \frac{\Sigma R_i \cdot m_i}{m_{cv}}$	(36)

where m_{cv} is the total mass within the cylinder.

3.3.4 Temperature-Correlated Values

Enthalpy and heating values for individual species are correlated to the temperature of that species using the method provided by the CHEMKIN-III program from Sandia National Laboratories [125]. The correlation for the constant pressure specific heating value of a species j is defined as follows:

CHEMKIN Correlation for Constant Pressure Specific Heat of a single Species	$c_{p,j,i} = \frac{\overline{c}_{p,j,i}}{W_j} = \frac{R_{univ} \cdot \left(d_1 + d_2 T_i + d_3 T_i^2 + d_4 T_i^3 + d_5 T_i^4\right)}{W_j}$	(37)

where T_i is the temperature of the zone, and d_1 through d_5 are coefficients linked to that individual species. The program chooses between two sets of constants for any given chemical species; one for temperatures below 1000 K, and the other for higher temperatures. With the temperature set, Equation 37 is used to calculate the molar specific heat, which is immediately converted to a mass basis by dividing by the molecular weight of the species. Note that the constant volume specific heat can be found similarly:

CHEMKIN Correlation for Constant Volume Specific Heat of a single Species	$c_{v,j,i} = \frac{R_{univ} \cdot \left(d_1 + d_2 T_i + d_3 T_i^2 + d_4 T_i^3 + d_5 T_i^4\right) - R_{univ}}{W_j}$ $c_{v,j,i} = \frac{\overline{c}_{p,j,i} - R_{univ}}{W_j}$	(38)

With the specific heats of all the individual species known, it is possible to find the mass-averaged specific heat of a zone with constant pressure illustrated here as an example:

Constant Pressure Specific Heat of a single Zone	$c_{p,i} = \frac{\sum_j m_{j,i} \cdot c_{p,j,i}}{\sum_j m_{j,i}}$	(39)

Using a similar methodology, the CHEMKIN-III correlation can be used to calculate the standardized molar enthalpy of a species *j* at a given temperature within a zone *i*:

CHEMKIN Correlation for the Molar Enthalpy of a Species	$\bar{h}_{j,i} = R_{univ} \cdot T_i \cdot \left(d_1 + \frac{d_2}{2} T_i + \frac{d_3}{3} T_i^2 + \frac{d_4}{4} T_i^3 + \frac{d_5}{5} T_i^4 + \frac{d_6}{T_i} \right)$	(40)

utilizing the same constants and values in the above correlations including an extra constant d_6. These correlated values are used later in the balancing of internal energy and enthalpy, particularly within the combustion cycle.

3.3.5 Intake Conditions and the Chemistry of Combustion

Before combustion can be modeled, it is necessary to model the chemical processes occurring within the cylinder. It is assumed that during combustion, a specific amount of oxygen and fuel will be entrained to a combustion film, and react stoichiometrically to form the products of combustion, which are then placed within the burned zone. Entrained along with the oxygen are the other species composing the unburned zone of the cylinder, namely the other components of the intake air (most notably molecular nitrogen) and the recycled products of combustion from the previous cycle. These entrained products are assumed to be inert during combustion, and are moved into the burned zone alongside the products. Both the entrainment and production processes represent a transfer of mass between the three zones of the model, and this transfer is modeled through three equations: a "global" reaction equation for entrainment (as well as initial speciation), a "local" reaction equation for production, and a rate equation to govern the speed of the reaction.

It is possible for an HR model to include the prediction of exhaust species. However, 0-D models tend to have difficulty making accurate descriptions of emissions species [126]. Furthermore, a dedicated emissions analyzer that operates outside of the HR model is more effective in this role. Use of an analyzer allows for calculation of combustion efficiency, which the HR model can then utilize for calibration in

order to calculate the true RHR [109]. As a result, an extensive equation describing the chemical combustion reaction is not needed. In this effort, the fuel molecule allows for carbon, hydrogen, oxygen, and nitrogen (CHON) atoms, and inlet air is comprised of approximately 21% molecular oxygen (O_2) and 79% molecular nitrogen for simplicity. Moreover, the only possible products of combustion are carbon dioxide (CO_2), water vapor (H_2O), and molecular nitrogen (N_2) if nitrogen is present in the fuel, as well as unburned fuel. While dissociation of the products is likely due to the high temperatures of combustion (particularly with respect to molecular oxygen and nitrogen forming nitrogen oxides), this dissociation is not currently modeled. In addition, this effort neglects the influence of water vapor, carbon dioxide, and argon in the ambient air. Future work can include dissociation and changes to air constituents for comparative purposes.

In order to simulate the global reaction equation, the model uses the known air and fuel flow rates into the engine, as well as the amount of residual gases and EGR present in the mixture. This Equation is given in Figure 8.

$$\xi(\mathrm{C}_w\mathrm{H}_x\mathrm{O}_y\mathrm{N}_z)+\delta\left(g_2\mathrm{O}_2+g_3\mathrm{N}_2\right)+\left(\varepsilon+\epsilon\right)\left(g_4\mathrm{O}_2+g_5\mathrm{CO}_2+g_6\mathrm{H}_2\mathrm{O}+g_7\mathrm{N}_2\right)$$
$$\rightarrow\lambda\left(g_4\mathrm{O}_2+g_5\mathrm{CO}_2+g_6\mathrm{H}_2\mathrm{O}+g_7\mathrm{N}_2\right)+\zeta(\mathrm{C}_w\mathrm{H}_x\mathrm{O}_y\mathrm{N}_z)$$

Figure 8. The global reaction formula used for evaluating the overall combustion reaction.

The coefficients ξ and δ provide the amount of fuel and air present (in moles), ε and ϵ are used to differentiate recycled species into moles of residual and EGR, λ represents the moles of products, and ζ is the number of moles of unburned hydrocarbons left over at the end of the process. Since this effort is for CI engines that operate with equivalence ratios less than one, the formula anticipates excess oxygen being present in the reactants and, as a result, also the products. The coefficients g_2 and g_3 relate the ratios of O_2 and N_2 in the intake atmospheric air (0.21 and 0.79, respectively). The coefficients g_4 through g_7 represent the moles of each of the four products of combustion on both the left and right hand sides accounting for residual/EGR and combustion products (which will have the same fractional constituents), respectively. The last coefficient, g_8, allows for the inclusion of the combustion efficiency in the model. It is assumed

here for simplicity that a certain fraction of fuel does not convert in deference to writing partial oxidation components.

This results in the global formula separating inlet air oxygen and nitrogen (g_2 and g_3) from recycled oxygen and nitrogen (g_4 through g_7) utilizing separate coefficients. In particular, the first of these new coefficients (δ) is used for all inlet air species, while the others (ε and ϵ) account for gases recycled either by EGR, or through the internal residual fraction (both on a volume basis). The program then uses ε and ϵ with the exhaust species coefficients to populate the unburned zone at IVC. From this point, the coefficients are used to calculate the total moles (and therefore mass) of each species, based on the total amount of fuel used in a single engine cycle.

The mass at IVC is given as the sum of the intake, residual, and EGR mass:

Mass within the cylinder at IVC, from Conservation of Mass	$m_{IVC} = m_a + m_r + m_{EGR}$	(41)

Additionally, the mass at IVC can be approximated by using the ideal gas model:

Mass within the cylinder at IVC, from Ideal Gas Approximation	$m_{IVC} = \frac{p_{IVC} \forall_{IVC}}{R_{IVC} T_{IVC}}$	(42)

where p,$\forall$, and T are the known pressure, volume, and temperature in the cylinder at IVC (note: temperature is assumed to be the intake manifold temperature). In order to solve for the mass present at IVC, it is necessary to estimate the composition of the cylinder contents at IVC. Since δ represents the moles of air present in the reaction, the coefficient can then be solved for directly by making an assumption as to the mass of air present:

Moles of Air present at IVC	$\delta = n_a = m_a \cdot W_a$	(43)

where W_a is the molar weight of atmospheric air. The amount of fuel used per cycle on a molar basis can be solved using the measured mass flow rates of air and fuel flowing into the cylinder with the estimated amount of air:

Moles of Fuel used in a Cycle	$\xi = \delta \cdot \frac{\dot{m}_f}{\dot{m}_a} \cdot \frac{W_a}{W_f}$	(44)

in which $\dot{m}_f$ and $\dot{m}_a$ are the measured mass flow rates of fuel and air into the cylinder from the experimental setup, and W_f is the molecular weight of fuel. Next, the coefficient for EGR can be found:

Coefficient for Residual Gases	$\varepsilon = \frac{m_{EGR}}{W_{EGR}} = \frac{f \cdot m_{IVC}}{W_{EGR}}$	(45)

where W_{EGR} is the molecular weight of EGR, and f is the mass-based residual fraction of the engine, which can be estimated from measured engine parameters [3]:

Definition of Residual Fraction	$f = \frac{1}{r_c} \cdot \frac{p_i}{p_e} \cdot \frac{T_i}{T_e}$	(46)

as a function of the engine's compression ratio (r_c), and the pressure and temperature at the inlet (i) and exhaust (e). The coefficient for the EGR species can also be solved:

Coefficient for EGR utilized	$\epsilon = \frac{\delta \cdot EGR}{1 - EGR}$	(47)

and is written as a function of the amount of air present, and the ratio representing the amount of EGR used (measured in the experimental setup) [10]. Finally, the coefficient ζ in the global combustion formula can be found:

Coefficient for the amount of Fuel that does not react	$\zeta = (1 - \eta_c) \cdot \xi$	(48)

which is a function of the amount of fuel present, as well as the measured combustion efficiency of the engine (η_c):

Definition of Combustion Efficiency	$\eta_c = \frac{H_R - H_P}{m_f Q_{LHV}} = \frac{h_R m_R - h_P m_P}{m_f Q_{LHV}}$	(49)

which is the ratio of the change in enthalpy between the reactants and products of the reaction (denoted by the subscripts R and P, respectively) to the total energy that can be liberated from the fuel and expressed as the product of the fuel's mass (m_f) and lower heating value (Q_{LHV}). The remaining constants in the global combustion formula (g_4, g_5, g_6, and g_7) can then be solved using a traditional chemical atom balance. The program then calculates the mass and gas constant at IVC indicated by the balanced global

formula using the calculated residual fraction and known percentage of EGR, and iterates until the mass of residual, recycled, and intake species converge.

With an emissions analysis, the combustion efficiency of the engine cycle can be estimated from the remaining energy content of the species present within the exhaust emissions:

Experimental Combustion Efficiency Calculation	$\eta_c = 1 - \frac{\sum \dot{m}_i Q_{LHV,i}}{\dot{m}_f Q_{LHV,f}}$	(50)

where $\dot{m}_f$ is the mass flow rate of fuel into the engine, and $\dot{m}_i$ and $Q_{LHV,i}$ are the mass flow rates and lower heating values of any exhaust constituent species that can undergo further combustion (e.g., hydrogen, carbon monoxide, hydrocarbons, or particulates). This method requires a separate suite of emissions analysis components and techniques to evaluate the composition of the exhaust species [10]. In effect, Equation 50 calculates a measure of combustion inefficiency, and then subtracts from unity to find the emissions-indicated combustion efficiency. This value is of great importance to the HR model, as it serves as the mass fraction burned value used to calibrate the rate of combustion (discussed later).

With the reaction balanced, the program converts the intake gases from a molar to a mass basis. Changes in the intake due to boosting (through either turbocharging or supercharging) are accounted for by using the known pressure at IVC, the raised air flow rate into the cylinder, and the inlet air temperature that are all measured quantities by the experimental setup.

With the global reaction defined, the program can provide accurate calculations of various constants used throughout the program (such as a zone's gas constant or specific heating value). The formula can also be used to describe the entrainment processes during combustion. However, the global reaction formula is unable to provide a clear representation on the production of any given species, and, therefore, the program employs a local combustion formula.

The second chemical equation is the local formula which solves for the transformation of chemical species during a series of stoichiometric combustion events (occurring one after another at each step in the program) similar to other authors [103, 127]. This reaction is derived from the formula often used in balancing equations to find the stoichiometric fuel-air ratio (see Figure 9).

$$C_wH_xO_yN_z + a\left(O_2 + 3.76N_2\right) \rightarrow wCO_2 + \frac{x}{2}H_2O + \left(3.76a + \frac{z}{2}\right)N_2$$

Figure 9. The stoichiometric reaction of air and fuel.

In this case, *w*, *x*, *y*, and *z* correspond to the number of atoms of carbon, hydrogen, oxygen, and nitrogen present within the fuel molecule (respectively), and *a* is the amount of oxygen (in moles) required to balance the reaction, such that all of the oxygen and fuel molecules are consumed in the reaction. The reaction provides for production of CO_2 and H_2O due to combustion, as well as showing the required amount of oxygen entrainment for stoichiometric combustion. However, the reaction also blends nitrogen entrainment, but this is included in the global formula. Therefore, this reaction is adjusted to remove the nitrogen entrainment component from the left and right sides of the reaction (see Figure 10).

$$C_wH_xO_yN_z + aO_2 \rightarrow wCO_2 + \frac{x}{2}H_2O + \frac{z}{2}N_2$$

Figure 10. The simplified stoichiometric reaction of air and fuel.

This reaction uses the same coefficients as the stoichiometric formula (Figure 9). Most importantly, it can be shown that the coefficient *a* is the same in both equations. In this way, nitrogen production is separated from entrainment, supplying the final relation needed to model the production processes of combustion. For convenience, the program rewrites the formula again, in order to remove all fractional components from the coefficients, and to index them for use elsewhere (see Figure 11).

$$C_wH_xO_yN_z + l_2O_2 \rightarrow l_3CO_2 + l_4H_2O + l_5N_2$$

Figure 11. The local reaction of oxygen and fuel.

where l_2 is the number of moles of oxygen molecules needed to balance the equation, and l_3, l_4, and l_5 are equal to the coefficients w, $x/2$, and $z/2$ in the stoichiometric reaction (respectively).

Note that this reaction does not take EGR species or the nitrogen from the ambient air into account. Both EGR and nitrogen will affect the rate of combustion, as well as the amount of energy released from the subsequent reaction by adding diluents to the combustion reaction. As a result, the local combustion formula is not used to measure the energy released from combustion directly, or as a way to

calculate the rate of combustion. Instead, it only serves as a mechanism to provide for the change of species from the reactants (fuel and oxygen) to products (carbon dioxide, water, and molecular nitrogen). When paired with the global formula, both the entrainment and production of species can be modeled entirely as a function of the rate of combustion of fuel, which is discussed later.

To calculate the equivalence ratio of the engine cycle, the program compares the actual fuel-air ratio to the fuel-air ratio of a stoichiometric reaction:

Definition of Equivalence Ratio	$$\Phi = \frac{\left(m_f / m_a\right)_{actual}}{\left(m_f / m_a\right)_{stoich}}$$	(51)

In order to calculate the actual fuel-air ratio, it is only necessary to use the molar weights of fuel and air, the fraction of the cylinder volume that contains intake air, and the total amount of fuel present:

Actual Fuel-Air Ratio	$$\left(\frac{m_f}{m_a}\right)_{actual} = \frac{\xi \cdot W_f}{\delta \cdot W_a}$$	(52)

with air assumed to have a molecular weight of 28.97 g/mole.

The solution of the stoichiometric fuel-air ratio is given via a similar equation, using the amount of air needed to balance the stoichiometric reactions equations:

Stoichiometric Fuel-Air Ratio	$$\left(\frac{m_f}{m_a}\right)_{stoich} = \frac{W_f}{l_2 \cdot (W_{O_2} + 3.76 \cdot W_{N_2})}$$	(53)

where l_2 is the required amount of oxygen from the local combustion formula (see Figure 11), and the molar weights of oxygen and nitrogen are represented by and W_{O_2} and W_{N_2}. With the actual and stoichiometric conditions set, the equivalence ratio is therefore known.

Both the global and local combustion reactions are dependent on the size and composition of the fuel molecule. Mineral diesel fuels are composed of numerous species of long-chain hydrocarbons, primarily alkanes from C_{10} to C_{19}. It is common practice to approximate fuel with a single molecular formula that represents the average molecule size within the fuel. As a result, the program includes formulas for diesel fuels #1 (approximated as $C_{14.4}H_{24.9}$) and #2 ($C_{10.8}H_{18.7}$). In addition, other standard fuels are also accounted for, namely kerosene ($C_{12}H_{23}$) and JP-8 ($C_{11}H_{21}$) [128].

Biodiesel fuels are similar to diesel fuels, except they replace fatty-acid methyl esters (FAME) for alkanes. Previous efforts in the authors' laboratory investigating biodiesel allow for a complete determination of the chemical composition of specific biodiesel fuels [11]. For the HR program, the biodiesel species are broken down into individual species based on the lipid number of the acid that they were formed from, in the form *a:b*, where *a* is the number of carbon atoms within the methyl ester acid, and *b* is the number of double bonds within the molecule. This notation is not always able to communicate the actual species present within the fuel, as multiple species can take the same form (such as methyl linoleate and linoelaidate, which both are written as 18:2). However, the notation is still useful for determining the speciation of atoms within the methyl ester molecules themselves, and therefore will yield a good estimate for the average chemical formula of the biodiesel fuel.

The relation of the lipid number to the molecular formula is as follows [129]:

Lipid Number Relation	$C_{(a+1)}H_{2(a+1-b)}O_2$	(54)

where the subscripts *a* and *b* are the components of the lipid number. In this way, a saturated fatty acid (which has no double bonds) will always have twice as many hydrogen atoms as carbon atoms. In unsaturated fatty acids, the number of double bonds increases, and so the molecule contains two less hydrogen atoms for each double bond present. For example, methyl stearate (octanoate) is formed from stearic acid, which has a lipid number of 18:0, and so a respective molecular formula of $C_{19}H_{38}O_2$. Species with a lipid number of 18:2 have two double bonds, requiring four less hydrogen atoms, for a molecular formula of $C_{19}H_{34}O_2$. Within the methyl ester molecules, the oxygen content stays relatively constant at two atoms per molecule, regardless of the size of the overall molecule [129].

By using the lipid numbers and mass fractions provided in the earlier study, the number of carbon, hydrogen, and oxygen atoms needed for an average chemical composition of the biodiesel fuel can be found:

Relation of fuel Carbon atoms to the fuel lipid number.	$w = \sum \frac{W_i \cdot a_i}{M_i} \cdot M$	(55)

Relation of fuel Hydrogen atoms to the fuel lipid number.	$x = \sum \frac{W_i \cdot 2(a_i - b_i)}{M_i} \cdot M$	(56)
Relation of fuel Oxygen atoms to the fuel lipid number	$y = \sum \frac{W_i \cdot 2}{M_i} \cdot M = 2$	(57)

where W_i is the mass fraction of a methyl ester subspecies, M_i is the molar weight of the subspecies, M is the average molar weight of the mixture, and w, x, and y are the coefficients used in the global and local combustion reactions. An example of the composition of various biodiesel fuels used in this analysis is included in Table 24 and Table 25 of the Appendices.

3.3.6 Fuel Injection, Ignition Delay, and Combustion Duration

Before the combustion rate can be defined, it is necessary to know the flow rate of fuel entering the cylinder through injection, and the allowable beginning and end of combustion. To find the flow rate of fuel into the cylinder before and during combustion, the timing, length, and duration of the injection event must be known. The most common expression detailing the mass flow rate of fuel during injection is given as [104, 130]:

Mass Flow Rate of Fuel into the Cylinder by Injection	$\dot{m}_{f,inj} = C_d A_n n_h n_{inj} \left(2 \cdot \rho_f \cdot \Delta p\right)^{1/2}$	(58)

where the mass flow rate of fuel by injection $\left(\dot{m}_{f,inj}\right)$ is defined by the area of the nozzle holes through which the fuel flows (A_n), the number of holes on each injector (n_h), the number of injectors (n_{inj}), the density of the injected fuel (ρ_f), and the change in pressure (Δp) between the nozzle (often approximated as the fuel line pressure) and cylinder. Additionally, the fuel flow rate is defined by a dimensionless constant (C_d) known as the coefficient of discharge, and is normally set to 0.39 [104, 131]. To add fuel to the cylinder, the program assumes a square wave for fuel injection, and converts Equation 58 to be dependent on crank angle in place of time using the relation given in Equation 6:

Change in Mass of Fuel added with respect to crank angle	$\frac{dm_{fa}}{d\theta} = \dot{m}_{f,inj} \cdot \frac{dt}{d\theta}$	(59)

In order to finish the calculation, the program only requires a limiting factor on the total amount of fuel that can be injected. With the mass flow rate of fuel flowing into the engine known through an upstream Coriolis flow meter, the total mass of fuel injected per cycle can be written as follows:

Mass of Fuel present in a Cycle	$m_f = \dot{m}_f \cdot \frac{1 min}{N rev} \cdot \frac{60 sec}{1 min} \cdot \frac{n_R rev}{1 cycle}$	(60)

where n_R is the number of revolutions per engine cycle, and $\dot{m}_f$ is the rate of fuel consumption of the engine. During the addition of fuel by injection, the program continually checks the total amount of fuel injected against the amount permitted by Equation 60. If the total mass injected reaches or exceeds the known amount of fuel used per cycle, the program ends the injection process. This model currently only allows for a single fuel injection profile with inclusion of multiple profiles left as a future enhancement.

Prior to fuel injection, the cylinder contains only unburned mixture and the temperature can be calculated using the ideal gas model (Equation 42) since the amount of mass in the cylinder is constant:

Unburned Zone Temperature from Ideal Gas Approximation	$T_u^k = \frac{p^k \cdot \forall_{cv}^k}{m_{IVC} \cdot R_{IVC}}$	(61)

with the pressure and volume of the cylinder known at each time-step, *k*. However, when fuel is added, the vaporization event will draw energy away from the working fluid, the fuel zone will begin to exist, and the amount of mass in the cylinder grows. As a result, calculations are needed in order to estimate the temperature of the fuel and unburned zones after injection and vaporization. This requires summing the internal energy of the two component zones (unburned and fuel) with the bulk internal energy within the cylinder:

Internal Energy of the Control Volume before Ignition	$U_{cv}^k = m_{cv}^k \cdot u_{cv}^k = m_u^k \cdot u_u^k + m_f^k \cdot u_f^k = U_u^k + U_f^k$	(62)

where U_{cv}^k is the total internal energy content of the mass within the control volume, m_{cv}^k and u_{cv}^k are the mass and specific internal energy of the entire control volume, and u_u^k and u_f^k are the specific internal energy of the unburned and fuel zones (respectively).

At this point, it is necessary to translate the specific internal energy to a temperature value following from the relation of internal energy to enthalpy:

Relation of Internal Energy to Enthalpy, molar basis	$\overline{u} = \overline{h} - R_{univ} \cdot T$	(63)

where both internal energy and enthalpy are written on a molar basis. After further manipulation, the expression for the standardized internal energy of species *j* within zone *i* can be written using the enthalpy correlation (Equation 40):

Internal Energy of a single Species, molar basis	$\overline{u}_{j,i} = \overline{h}_{j,i} - R_{univ} \cdot T_i$	(64)

where the internal energy is a function of the universal gas constant, the temperature of the respective zone. The resulting internal energy of a zone can then be found by summing the total internal energy of each species:

Internal Energy of a single Zone	$U_i = \sum_j m_{j,i} \cdot \frac{\overline{u}_{j,i}}{W_j} = \sum_j n_{j,i} \cdot \overline{u}_{j,i}$	(65)

where U_i is the total internal energy of zone *i* for Equation 62. Since the mass and composition of each zone is known at this point, only the bulk, fuel, and unburned temperatures are required to balance Equation 62. The bulk temperature can be solved quickly using the ideal gas model:

Control Volume Temperature from Ideal Gas Approximation	$T_{cv}^k = \frac{p^k \cdot \forall_{cv}^k}{m_{cv}^k \cdot R_{cv}^k}$	(66)

updating the mass and bulk gas constant. As a result, the only remaining unknowns are the temperature values corresponding to each of the two zones, requiring one additional equation in addition to the balance of internal energy (Equation 62).

This equation comes from the relationship between the volume of each zone and the total volume within the cylinder (given in Equation 30) that is expanded using the ideal gas model:

Extension of the relationship between the Volumes of the Zones and the Control Volume	$\forall_{cv}^k = \forall_u^k + \forall_f^k = \frac{m_u^k \cdot R_u^k \cdot T_u^k}{p_u^k} + \frac{m_f^k \cdot R_f^k \cdot T_f^k}{p_f^k}$	(67)

This equation can be simplified by the fact that the pressure of each zone is equivalent to the total pressure within the control volume:

Simplification of Equation 67	$\forall_{cv}^{k} = \frac{m_{cv}^{k} \cdot R_{cv}^{k} \cdot T_{cv}^{k}}{p^{k}} = \frac{m_{u}^{k} \cdot R_{u}^{k} \cdot T_{u}^{k} + m_{f}^{k} \cdot R_{f}^{k} \cdot T_{f}^{k}}{p^{k}}$	(68)

By further simplification, it can be shown that the temperatures of each zone are related to each other:

Relation between the Temperatures and Masses of the Zones and the Control Volume before Ignition	$\left(m_{u}^{k} + m_{f}^{k}\right) \cdot R_{cv}^{k} \cdot T_{cv}^{k} = m_{u}^{k} \cdot R_{u}^{k} \cdot T_{u}^{k} + m_{f}^{k} \cdot R_{f}^{k} \cdot T_{f}^{k}$	(69)

The temperature of the fuel zone is set to the flash point of the fuel at the first time step after injection begins.

To iterate, the program takes advantage of the Newton-Raphson method, shown here in its general form:

Newton-Raphson Method	$x_{n+1} = x_{n} - \frac{g\big\vert_{x_n}}{g'\big\vert_{x_n}}$	(70)

In this case, the variable x is replaced with the temperature of the unburned zone (T_u), and the function g is by a form of Equation 62:

Definition of g for the Newton-Raphson Method, before Ignition	$g\big\vert_{x_n} = U_{u} + U_{f} - U_{cv} = 0$	(71)

where the internal energy of the control volume can be solved immediately because the mass, composition, and temperature of the bulk gas is known.

In order to find the derivative $g'|_{x_n}$, it is necessary to understand the functional dependency of each of the terms composing the function g, and how each of these terms relates to the chosen value of x. Each of the internal energy terms are themselves functions of the temperature, mass, and constant volume specific heat of their respective zones (or of the entire control volume). However, for the purposes of using the Newton-Raphson method, a part of this dependency is ignored; the mass of each zone is already known, and so the mass will not change between successive iterations. Additionally, the constant volume specific heats of all three terms are known to be a function of temperature, and so the Newton-Raphson method can be solved as the change in internal energy only with respect to temperature, thus minimizing the number of computations required. Furthermore, the temperature of the control volume (T_{cv}) is already

known through Equation 66. After taking these dependencies into account, the equation for $g'|_{x_n}$ can be written as follows:

Definition of g' for the Newton-Raphson Method, before Ignition	$$g'\big\|_{x_n} = \frac{dg\big\|_{x_n}}{dT_u^k} = \frac{dU_u}{dT_u^k} + \frac{dU_f}{dT_u^k} = \frac{dU_u}{dT_u^k} + \frac{dU_f}{dT_f^k}\frac{dT_f^k}{dT_u^k}$$	(72)

As a result, it is only necessary to relate the change in the fuel zone temperature to the change in the unburned zone temperature, as well as relating to change in internal energy to the change in temperature, at a given time step *k*.

Equation 9 is used to find the change in a zones internal energy only with respect to its temperature:

Rate of Change of Internal Energy with respect to Temperature	$$\frac{dU_i}{dT_i} = m_i \cdot c_{v,i} = \sum_j m_{j,i} \cdot c_{v,j,i}$$	(73)

In this case, the mass of a zone is already known, and its constant volume specific heat can be found using Equation 38 and the known composition of the zone.

By rewriting Equation 69, the fuel zone temperature can be written in terms of the unburned zone temperature:

Relationship between the Fuel and Unburned Temperatures	$$T_f^k = \frac{\left(m_u^k + m_f^k\right) \cdot R_{cv}^k \cdot T_{cv}^k - m_u^k \cdot R_u^k \cdot T_u^k}{m_f^k \cdot R_f^k}$$	(74)

By taking the derivative of Equation 74 with respect to the unburned zone temperature, a relation for the change in fuel temperature with respect to the unburned zone temperature is given:

Rate of Change of the Fuel Temperature with respect to the Unburned Temperature	$$\frac{dT_f^k}{dT_u^k} = \frac{-m_u^k \cdot R_u^k}{m_f^k \cdot R_f^k}$$	(75)

With all of the components defined, Equation 70 can be rewritten explicitly for use in the program:

Newton-Raphson Method before the Start of Combustion	$$T_u^{n+1} = T_u^n - \frac{U_u + U_f - U_{cv}}{m_u^k \cdot c_{v,u}^n - m_f^k \cdot c_{v,f}^n \cdot \frac{m_u^k \cdot R_u^k}{m_f^k \cdot R_f^k}}$$	(76)

The program then iterates Equation 76 until the temperature of the unburned zone converges, and Equation 74 is solved one final time in order to find the current temperature of the fuel zone. With the mass and temperature known, it is possible to calculate the volume of the fuel and unburned zones through the ideal gas equation of state (by Equation 32). As a result, as fuel is injected, the fraction of the volume taken up by the fuel zone increases, and the fraction of the volume taken up by the unburned zone will decrease.

After injection of fuel, a certain time must pass before the fuel can ignite on its own. Many separate equations exist for finding the approximate ignition delay (τ) of diesel fuel. One such example is an Arrhenius expression as suggested by Hiroyasu et al. [107]:

Correlation of Ignition Delay	$\tau = A \cdot 10^{-3} \cdot \left(\frac{p}{10^5} \right)^{-n'} \cdot e^{E_a / (R_{univ} \cdot T_{cv})}$	(77)

Empirical values for different fuel and engine types have been provided by many authors [132-134]. As shown, the ignition delay is largely a function of the activation energy of the fuel (E_a) and bulk gas temperature, as well as the universal gas constant, and the pressure within the cylinder. Furthermore, the function employs two constants (A and n'), which have been tabulated by numerous authors, and are given in Table 7 [106, 134-148]. The constants used by some authors are also functions of the bulk equivalence ratio within the cylinder. The expression relies on the bulk temperature of the mixture within the control volume, as opposed to the temperature of the fuel itself, and so will function whether or not fuel vaporization and heating is modeled or not.

Table 7. Variables used in conjunction with Equation 77 and the corresponding authors; Φ is the bulk equivalence ratio.

Coefficient Source	*A*	*n'*	E_a/R_{univ}
Wolfer [135]	0.44	1.19	4650
Kadota [108]	6.58	0.52	4400
Spadaccini [142, 143]	$4 \cdot 10^{-10}$	1	20080
Stringer [136]	0.0409	0.757	5473
Hiroyasu [106]	$0.01 \cdot \Phi^{-}$	2.5	6000
Fujimoto (High Pressure)	0.134	1.06	5130
Fujimoto (Low Pressure)	0.136	0.615	4170
Pischinger [146]	0.0081	1.14	7813
Watson [141]	3.45	1.02	2100
Assanis [134]	$2.4 \cdot \Phi^{-0.2}$	1.02	2100
Stiesch [104]	$4 \cdot \Phi^{-1.04}$	2.5	6000

From Equation 77, it is possible to predict ignition timing for the specific run time conditions. In particular, combustion is initiated when the ignition delay becomes smaller than the time-step (*dt*) between data points:

Theoretical Ignition Timing	$\int_0^t \frac{1}{\tau} dt \geq 1$	(78)

Also, the ignition delay term may change rapidly between time steps, due to variations in pressure and temperature over short periods of time.

To calculate the ignition timing of each of the 11 correlations, the program follows the following algorithm, solving for all of correlations simultaneously:

- Each of the sets of coefficients provided in Table 7 yields a set ignition delay (in seconds) when used with Equation 77.
- At a given time step *k*, the program computes the ignition delay τ^k using the in-cylinder pressure and bulk gas temperature.
- The value of τ^k is compared to the ignition delay at the previous step (τ^{k-1}), after it is adjusted to take into account the time that has passed (t_{step}), in order to evaluate which of the two ignition delays is smaller:

Functional Ignition Delay	$(\tau_{ig}^{k-1} - t_{step}) \sim \tau_{ig}^{k}$	(79)

- The smaller of the two values in Equation 79 is used as the current ignition delay, and is compared to the value of t_{step}.
- If the current ignition delay is smaller than t_{step}, it is assumed that combustion will begin at the next time step (k+1).
- If the value of t_{step} is smaller, then the program moves forward to the next time step, and repeats the process.
- The algorithm continues until the start of combustion corresponding to each of the ignition delays is found.
- Alternatively, if the value of k is too large to be realistic (such as past EVO), the program ceases iteration and returns a negative value of k to signify that a particular ignition delay correlation has failed.

The program also calculates an expected point of ignition, which can be obtained directly from the pressure trace. In particular, a reasonably reliable method of defining the beginning of combustion occurs through analysis of the fluctuations in pressure readings [134, 149-151]. For this analysis, Syrimis et al. showed that the zero value of the second derivative of pressure with respect to time occurs slightly before the point of autoignition within the cylinder, and that the second derivative of pressure will peak slightly after the point of igntion [150]. With the expected ignition time calculated using this second-derivative methodology, the program keeps track of the deviation from the expected ignition time for each of the correlations:

Allowable Ignition Deviation	$deviation = \left\lvert \theta_{ig,c} - \theta_{ig,ex} \right\rvert$	(80)

where $\theta_{ig,c}$ is a correlated time of ignition (from the values in Table 7), and $\theta_{ig,ex}$ is the expected time of ignition (second-derivative method). Whichever correlation has the smallest deviation is chosen as the actual point of ignition for the remainder of the cycle. In the event that two (or more) ignition delays are equidistant from the expected point of ignition, the correlated point of ignition that occurs after the time

of ignition indicated by the pressure trace is assumed to be correct. Finally, if none of the correlated times of ignition are within a prescribed deviation from the ignition time indicated by the pressure trace, the correlated ignition delays are thrown out entirely, and the program continues with the time of ignition indicated by the second derivative of the pressure trace. This prescribed deviation can be set by the user, but is otherwise set to a default value of five degrees of crank angle.

At this point, the combustion function then toggles a "burn" condition, allowing it to calculate mass flow between zones from the chemical reaction. Additionally, the identity of the particular correlation used is saved to the combustion function's output. Alternatively, the user can also select to use a particular ignition delay correlation. In this case, the program still keeps track of the deviation from the expected point of ignition, and will reset the ignition correlation if the deviation is deemed too large.

Calculation of the end of combustion is a slightly more challenging task. It has been claimed by some authors that the end of combustion may be linked to the minimum of either the first or second derivative of pressure within the system [150]. Other authors have indicated that the end of combustion can be linked loosely to when the output HR of the program reaches 90% of its maximum value [87, 150]. Another means of limiting combustion is by letting the combustion reaction run its course. In this case, the reaction is allowed to run up to EVO, and is primarily controlled by the amount of oxygen and fuel present within the cylinder, and could also be controlled by the pressure and temperature as well. When one of the necessary chemical components is used up, the reaction slows down dramatically, but additional reactions are not prevented from occurring if conditions are conducive to combustion later on in the cycle (such as secondary fuel injection close to EVO). For this work, the combustion cycle is allowed to continue just before EVO, as it ensures that the amount of material burned within the cylinder follows the combustion rate equation (presented later). The other means of determining the end of combustion are also utilized (e.g., minimum of first derivative of pressure), but do not directly control the reaction; instead, they are displayed at the end of the program for later analysis.

In this effort, another model using a polytropic expansion expression is proposed. For the majority of the combustion cycle, the RHR by the fuel is much greater than the combined rate of heat

transfer and work done by the engine, and there is a net addition of energy to the system. However, after the combustion event ends, the change in pressure of the contents is only due to geometric expansion of the cylinder volume and heat transfer to the cylinder walls. In this situation, one can assume that the working fluid will behave according to the polytropic relationship (often used when modeling engines) [103, 152]:

Polytropic Relationship	$p\forall^n = c$	(81)

where c is a constant, and n is the polytropic index, which can range anywhere from 1.2 (the lower limit of what is expected after combustion) to 1.4 (signifying isentropic expansion):

Allowable Range of n for the Polytropic Relationship	$1.2 \le n \le 1.4$	(82)

Since the pressure and volume terms are known for all points between IVC and EVO, the program can evaluate Equation 81 across the entire engine cycle. If at any point the change in Equation 81 between points is found to be constant, then it can be reasoned that the engine is undergoing expansion only, and the net energy addition to the system is zero, signifying that combustion has ended (or is about to end). As the actual value of the polytropic index is not known, the program repeats this process, varying n across the possible range of values given by Equation 82. The equation is therefore used to find the expected end of ignition at separate values of n, varying from 1.2 to 1.4. The program then averages the values to provide a single expected value for the end of combustion.

In addition, the program also calculates the change in the polytropic exponent by backtracking from EVO towards TDC. It is assumed that combustion is more or less completed by EVO, and that no other late-stage events (such as post-oxidation fuel injection) will take place. Therefore, expansion at this portion of the cycle will behave according to Equation 81. By moving backwards through the pressure trace, the point where Equation 81 is no longer constant can be found, indicating the point where combustion could have ended.

3.3.7 Combustion Cycle Calculation

Prior to the beginning of combustion, a divide exists between the unburned and fuel zones. At the onset of combustion, a set amount of fuel enters (i.e., is entrained into) this divide from the fuel zone. Moreover, a set amount of oxygen is assumed to move into this divide from the unburned zone in the exact amount needed for stoichiometric combustion, as described by the local combustion formula (see Figure 11). By assuming that the unburned zone is evenly mixed, the packet of mass coming from the unburned zone is of the same composition as the unburned zone as a whole. Therefore, the mole fractions of each species within the material entrained from the unburned zone is equal to the mole fractions of those species within entire unburned volume. In this way, the amount of each species entrained into the film at any given time is dependent on the instantaneous rate of consumption of fuel.

Numerous models exist for controlling the rate of combustion of fuel within the cylinder. One such equation is an Arrhenius expression, provided by Hiroyasu et al. [104, 107]:

Arrhenius Expression for the Rate of Combustion	$\frac{dm_{fb}}{dt} \le K \cdot \rho_{mix}^{2} \cdot y_{fv}^{1} \cdot y_{\mathrm{O}_2}^{5} \cdot \forall_{cv} \cdot e^{-E_a/(R_{univ} \cdot T_{cv})}$	(83)

where the mass burn rate (dm_{fb}/dt) is given as a function of the mixture density (ρ_{mix}), the mass fractions of vaporized fuel and oxygen with respect to total amount of material within the cylinder (y_{fv} and y_{O_2}), and the total cylinder volume ($\forall_{cv}$). Note that this expression utilizes the same activation energy described by the Arrhenius expression in Equation 77 for calculating ignition delay. The constant K represents the speed of combustion and is adjusted between iterations of the combustion function of the program that will be discussed later.

In the HR model presented herein, it is required that the mass burn rate be expressed in terms of crank angle instead of time:

Rate of Change of the Mass of Fuel due to Combustion	$\frac{dm_{fb}}{d\theta} = \frac{dm_{fb}}{dt} \cdot \frac{dt}{d\theta} \approx \frac{dm_{fb}}{dt} \cdot \frac{t_{step}}{\Delta\theta}$	(84)

Functionally, the derivative of time with respect to crank angle is replaced with the time step divided by the change in crank angle between time steps (from Equation 6). Additionally, it is assumed that all fuel

within the cylinder is vaporized by the time that combustion begins, allowing Equation 83 to be rewritten to a form useable in the program:

Functional Arrhenius Expression for the Rate of Combustion	$\frac{dm_{fb}}{d\theta} \le \frac{t_{step}}{\Delta\theta} \cdot K \cdot \rho_{cv}^2 \cdot y_f \cdot y_{O_2}^5 \cdot \forall_{cv} \cdot e^{-E_a/(R_{univ} \cdot T_{cv})}$	(85)

where y_f is the mass fraction of all fuel with respect to the total amount of material within the cylinder, and ρ_{cv} is the density of the bulk gas.

With the rate of combustion set by Equation 85, it is possible to solve for oxygen entrained from the unburned zone, and therefore the rate of entrainment and production of all species moving into the burned zone. In order to react stoichiometrically, the amount of oxygen needed is written as a function of the mass of fuel burned, where l_2 is the coefficient for oxygen consumed per mole of fuel from the local combustion formula (see Figure 11):

Rate of Change of Oxygen due to Combustion	$\frac{dm_{O_2}}{d\theta} = \frac{dm_{fb}}{d\theta} \cdot \frac{W_{O_2}}{W_{fuel}} \cdot l_2$	(86)

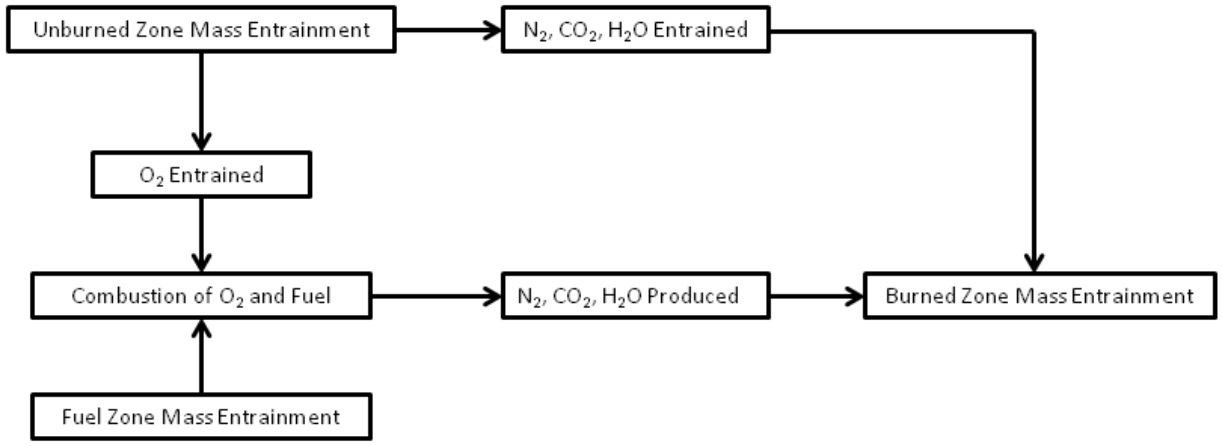

Figure 12. The flow of mass through entrainment and production from the fuel and unburned zones into the burned zone.

From this equation, it is possible to define the change in mass of CO_2, H_2O, and N_2 due to entrainment from the unburned zone as illustrated by Figure 12. The rate of entrainment of each species is related back to the calculated rate of entrainment for O_2 in Equation 86. This is based on the assumption

that volume of the unburned zone and the volume of material entrained at each time step have the same ratio of species. The entrainment rate of each species (subscript *e*) into the burned zone is then defined, using the ratio of its molecular weight and mole fraction within the unburned zone (using the coefficients of the global combustion formula, see Figure 8) both with respect to O_2:

Rate of Entrainment of Carbon Dioxide due to Combustion	$\frac{dm_{CO_2,e}}{d\theta} = \frac{dm_{O_2}}{d\theta} \cdot \frac{W_{CO_2}}{W_{O_2}} \cdot \frac{(\varepsilon+\epsilon)\cdot g_5}{\delta \cdot g_2 + (\varepsilon+\epsilon)\cdot g_4}$	(87)
Rate of Entrainment of Water due to Combustion	$\frac{dm_{H_2O,e}}{d\theta} = \frac{dm_{O_2}}{d\theta} \cdot \frac{W_{H_2O}}{W_{O_2}} \cdot \frac{(\varepsilon+\epsilon)\cdot g_6}{\delta \cdot g_2 + (\varepsilon+\epsilon)\cdot g_4}$	(88)
Rate of Entrainment of Nitrogen due to Combustion	$\frac{dm_{N_2,e}}{d\theta} = \frac{dm_{O_2}}{d\theta} \cdot \frac{W_{N_2}}{W_{O_2}} \cdot \frac{\delta \cdot g_3 + (\varepsilon+\epsilon)\cdot g_7}{\delta \cdot g_2 + (\varepsilon+\epsilon)\cdot g_4}$	(89)

The production rates of CO_2, H_2O, and N_2 from combustion (subscript *p*) are also calculated similarly by using the rate of consumption of O_2 by local combustion (see Figure 11):

Rate of Production of Carbon Dioxide due to Combustion.	$\frac{dm_{CO_2,p}}{d\theta} = \frac{dm_{O_2}}{d\theta} \cdot \frac{W_{CO_2}}{W_{O_2}} \cdot \frac{l_3}{l_2}$	(90)
Rate of Production of Water due to Combustion	$\frac{dm_{H_2O,p}}{d\theta} = \frac{dm_{O_2}}{d\theta} \cdot \frac{W_{H_2O}}{W_{O_2}} \cdot \frac{l_4}{l_2}$	(91)
Rate of Production of Nitrogen due to Combustion	$\frac{dm_{N_2,p}}{d\theta} = \frac{dm_{O_2}}{d\theta} \cdot \frac{W_{N_2}}{W_{O_2}} \cdot \frac{l_5}{l_2}$	(92)

By using these equations, it is possible to define the change in mass with respect to time of each species within any of the three zones (recall subscript *u* for unburned and *b* for burned):

Rate of Change in Unburned Zone Oxygen from Combustion	$\frac{dm_{O_2,u}}{d\theta} = -\frac{dm_{O_2}}{d\theta}$	(93)
Rate of Change in Unburned Zone Carbon Dioxide from Combustion	$\frac{dm_{CO_2,u}}{d\theta} = -\frac{dm_{CO_2,e}}{d\theta}$	(94)
Rate of Change in Unburned Zone Water from Combustion	$\frac{dm_{H_2O,u}}{d\theta} = -\frac{dm_{H_2O,e}}{d\theta}$	(95)
Rate of Change in Unburned Zone Nitrogen from Combustion	$\frac{dm_{N_2,u}}{d\theta} = -\frac{dm_{N_2,e}}{d\theta}$	(96)

Rate of Change in Burned Zone Carbon Dioxide from Combustion	$\frac{dm_{CO_2,b}}{d\theta} = \frac{dm_{CO_2,e}}{d\theta} + \frac{dm_{CO_2,p}}{d\theta}$	(97)
Rate of Change in Burned Zone Water from Combustion	$\frac{dm_{H_2O,b}}{d\theta} = \frac{dm_{H_2O,e}}{d\theta} + \frac{dm_{H_2O,p}}{d\theta}$	(98)
Rate of Change in Burned Zone Nitrogen from Combustion	$\frac{dm_{N_2,b}}{d\theta} = \frac{dm_{N_2,e}}{d\theta} + \frac{dm_{N_2,p}}{d\theta}$	(99)

As a result, the total mass flow rate of the fuel zone (including Equation 59), lost by the unburned zone, and gained by the burned zone is, respectively:

Rate of Change of Mass of the Fuel Zone	$\frac{dm_f}{d\theta} = \frac{dm_{fa}}{d\theta} - \frac{dm_{fb}}{d\theta}$	(100)
Rate of Change of Mass of the Unburned Zone	$\frac{dm_u}{d\theta} = \frac{dm_{O_2,u}}{d\theta} + \frac{dm_{CO_2,u}}{d\theta} + \frac{dm_{H_2O,u}}{d\theta} + \frac{dm_{N_2,u}}{d\theta}$	(101)
Rate of Change of Mass of the Burned Zone	$\frac{dm_b}{d\theta} = \frac{dm_{CO_2,b}}{d\theta} + \frac{dm_{H_2O,b}}{d\theta} + \frac{dm_{N_2,b}}{d\theta}$	(102)

Finally, the mass of species *j* within an arbitrary zone *i* at any time step *k* can be solved for, as well as the mass of an entire zone:

Mass of a single Species	$m_{j,i}^k = m_{j,i}^{k-1} + \frac{dm_{j,i}}{d\theta} \cdot \Delta\theta$	(103)
Mass of a single Zone	$m_i^k = m_i^{k-1} + \frac{dm_i}{d\theta} \cdot \Delta\theta$	(104)

With the masses of each zone now defined, the gas constants of each zone can also be found using Equations 34 and 35.

The next step of the combustion calculation sequence is to evaluate the temperature of each of the three zones. The primary equation used in this calculation is an expanded form of the balance of internal energy given by Equation 62:

Internal Energy of the Control Volume after Ignition	$U_{cv}^k = m_{cv}^k \cdot u_{cv}^k = m_u^k \cdot u_u^k + m_f^k \cdot u_f^k + m_b^k \cdot u_b^k$	(105)

where u_b^k and m_b^k are the specific internal energy and mass and burned zone, and the other values are the same as the ones used in Equation 62. By reusing Equations 63-65, the balance of internal energy can be rewritten to include the standardized internal energy of the burned zone:

Balance of Internal Energy during and after Combustion	$U_{cv} = U_u + U_f + U_b$	(106)

where the internal energy of any of the four components is a function of temperature and mass. Again, the mass of each zone is known, and so the only the temperature must be found in order to balance the internal energy equation. The bulk temperature is found using Equation 66, and allows for calculation of the bulk internal energy; therefore, the only remaining unknowns needed to balance Equation 105 are the temperature values corresponding to each of the three zones. This requires at least two more equations governing the relation of the temperatures to each other.

The relation between the volume of each zone and the total volume within the cylinder used in Equations 69 is expanded here, providing for an additional means to relate the zone temperatures to one another:

Relation between the Characteristics of the Zones and Control Volume after Ignition	$m_{cv}^k \cdot R_{cv}^k \cdot T_{cv}^k = m_u^k \cdot R_u^k \cdot T_u^k + m_f^k \cdot R_f^k \cdot T_f^k + m_b^k \cdot R_b^k \cdot T_b^k$	(107)

Since the mass and gas constant of each zone are known, as well as the bulk gas constant and temperature within the cylinder, the only unknown variables are again the temperatures of the three individual zones.

The final relation needed is a value for the temperature of a single zone. In this case, it is assumed that the temperature of the fuel zone will remain initially constant after combustion begins:

Fuel Temperature Assumption, without further Injection	$T_f^k = T_f^{ig-1}$	(108)

where T_f^{ig-1} is the temperature of the fuel at the instant before combustion begins. It was assumed earlier that the fuel zone would functionally begin at the temperature of vaporization of the injected fuel, and that any further changes in temperature would be modeled by a balance of internal energy. As a result, the temperature of the fuel zone at the onset of combustion cannot be stated with certainty. However, this assumption will not greatly affect the RHR since the majority of the mass within the fuel zone is transferred to the burned zone due to combustion. Moreover, the fuel zone mass will also be relatively small in comparison to the mass of the unburned zone, and so will not greatly contribute to the RHR through the rate of change of internal energy.

In the event that fuel is still being injected during combustion, Equation 108 is changed to the following form:

Fuel Temperature Assumption with Fuel Injection	$$T_f^k = \frac{\left(m_f^{k-1} - \frac{dm_{fb}^k}{d\theta}\cdot\Delta\theta\right)\cdot T_f^{k-1} + \frac{dm_{fa}^k}{d\theta}\cdot\Delta\theta\cdot T_{vap}^k}{m_f^k}$$	(109)

where $dm_{fb}^k/d\theta$ and $dm_{fa}^k/d\theta$ are the changes in fuel mass due to combustion and injection (respectively) at the current time step. Equation 109 takes the form of a mass average of the temperature of the fuel remaining with the fuel zone and the fuel added by injection at the current time step. In the event that injection ceases, this simplifies to:

Fuel Temperature Assumption, after Injection	$$T_f^k = T_f^{k-1}$$	(110)

In this way, Equation 110 mirrors Equation 108 almost exactly, except that the fuel zone temperature is frozen at an arbitrary point given by the end of injection, instead of the onset of combustion.

To iterate, the program again makes use of the Newton-Raphson method, using equations similar to those shown earlier (Equations 70-76). However, the temperature of the burned zone is chosen as the independent variable (as opposed to the temperature of the unburned zone), and Equation 71 is written to include the internal energy of the burned zone:

Definition of *g* for the Newton-Raphson Method, after Ignition	$$g\big\vert_{x_n} = U_u + U_f + U_b - U_{cv} = 0$$	(111)

In this case, the internal energy of the fuel zone is not considered to be a function of the temperature of the burned zone in order to simplify the numerical analysis, and the internal energy of the control volume is known through the thermodynamic characteristics of the bulk gas. The equation for $g'\vert_{x_n}$ follows suit:

Definition of *g′* for the Newton-Raphson Method, after Ignition	$$g'\big\vert_{x_n} = \frac{dg\big\vert_{x_n}}{dT_b^k} = \frac{dU_b}{dT_b^k} + \frac{dU_u}{dT_b^k} = \frac{dU_b}{dT_b^k} + \frac{dU_u}{dT_u^k}\frac{dT_u^k}{dT_b^k}$$	(112)

The burned and unburned zone temperatures are then related to each other rearranging Equation 107:

Relationship between the Unburned, Fuel, and Burned Zone Temperatures	$$T_u^k = \frac{\left(m_u^k + m_f^k + m_b^k\right)\cdot R_{cv}^k\cdot T_{cv}^k - m_b^k\cdot R_b^k\cdot T_b^k - m_f^k\cdot R_f^k\cdot T_f^k}{m_u^k\cdot R_u^k}$$	(113)

By taking the derivative of Equation 113 with respect to the burned zone temperature, a relation similar to that given in Equation 75 is found:

Rate of Change of Unburned Temperature with respect to Burned Temperature	$$\frac{dT_u^k}{dT_b^k} = \frac{-m_b^k \cdot R_b^k}{m_u^k \cdot R_u^k}$$	(114)

This results in the following iterative relationship for the burned gas temperature:

Newton-Raphson Method after the Start of Combustion	$$T_b^{n+1} = T_b^n - \frac{U_u + U_f + U_b - U_{cv}}{m_b^k c_{v,b}^n - m_u^k c_{v,u}^n \cdot \frac{m_b^k \cdot R_b^k}{m_u^k \cdot R_u^k}}$$	(115)

The program then iterates Equation 115 until the burned zone temperature converges, at which point the unburned zone temperature is solved through Equation 113.

At this point, the system of equations governing the combustion event can be solved for at any time *k* after the change in chemical species due to combustion has been calculated. The volume of each of the three zones can be solved directly through the ideal gas model:

Ideal Gas Approximation for an arbitrary Zone	$$\forall_i^k = \frac{m_i^k \cdot R_i^k \cdot T_i^k}{p^k}$$	(116)

With the volume and temperature known, all of the thermodynamic variables required to solve for the components of Equation 5 are now known at the point in time *k*. The program then steps forward in time, solves the change in species at the next time step, and calculates the next set of thermodynamic variables.

The program also calculates the AFT of the burning species, representing the temperature of the products of combustion if all of the energy released by the combustion reaction were applied to raising the temperature and pressure of the burned zone only. This is not representative of the actual event, as the energy released will be used immediately for various processes within the cylinder such as radiative heat transfer to the cylinder walls. As a result, the AFT cannot be used directly for the temperature of the burned zone. Instead, the AFT can be used in order to highlight the changes in combustion due to various phenomena for the user, as well as providing a means to assess radiative heat transfer. Because it is dependent on the amount of material combusting, any change in the rate of combustion (Equation 85) will cause a similar change in the AFT. Alternatively, the AFT can be lowered due to the inert products of

combustion from previous cycles being entrained into the combustion zone. These species lower the temperature by absorbing energy released in the reaction without reacting and releasing any chemical energy. In addition, the AFT can be used in the modeling of dissociation of chemical species and is a useful tool in the simulation of NO_x production [153].

The AFT is calculated using a balance of internal energy or enthalpy of the products and reactants of combustion within a control volume, and is used to calculate the heat of the reaction if no energy was transferred out of the burned zone by any means. The choice of which particular balance to use is dependent on the nature of the reaction being modeled. In the case of an internal energy balance, the reaction is assumed a constant volume process. Alternatively, an enthalpy balance includes the possibility of work being done on the burned zone, and so will produce a lower value of temperature as some energy is used to change the size of the control volume. In an IC engine, where the volume changes rapidly, a constant volume process would be more indicative of an instantaneous process (such as knock), which is an unrealistic expectation for a CI engine. As a result, a balance of enthalpy is more realistic than a balance of internal energy since the expansion of the combusting material is allowed and combustion is allowed to progress at a given rate; therefore, enthalpy is used in the calculation of the AFT [153, 154].

This balance begins by calculating the total enthalpy of each species within each of the zones of the control volume:

Enthalpy of a single Species	$H_{j,i}^{k} = n_{j,i}^{k} \cdot \bar{h}_{j,i}^{k}$	(117)

where $\bar{h}_{j,i}^{k}$ is the molar enthalpy of a species solved in Equation 40 for a specific point in time k, and $n_{j,i}^{k}$ is the number of moles of that species entrained or produced at that point in time. From here, the total enthalpy of a zone can be solved:

Enthalpy of a single Zone	$H_{i}^{k} = \sum_{j} H_{j,i}^{k}$	(118)

The final step is the balance of products and reactants of combustion, through the enthalpy of the three zones:

Balance of Enthalpy	$H_u^k + H_f^k = H_b^k$	(119)

Since the states of the unburned and fuel zones are already fixed, the program only needs to iterate the temperature of the burned zone in order to provide an estimate of the AFT of the reaction. In the enthalpy balance, the enthalpy of the chemical species of the unburned and fuel zones make up the reactants on the left side of Equation 119, while the enthalpy of the species of the burned zone make up the products on the right side. The program provides a guessed value for the temperature of the products without heat transfer to the other zones, while using the temperature of the unburned zone for calculating the enthalpy of the reactants. The program then solves for the product temperature iteratively, adjusting the temperature appropriately until the enthalpy calculation is balanced, and the final AFT is stored at the current time step.

Once the program reaches EVO, the mass, volume, temperature, and gas constant of each zone is catalogued for all points between IVC and EVO, as well as the mass of each species within the zones. Finally, the program saves the degree at which combustion begins, as well as the identity of the ignition delay correlation used. Additionally, the chosen end of combustion is saved, as well as the peak AFT, and a scalar value of the mass of fuel left unburned at EVO. The program also generates a plot of the adiabatic flame temperature throughout the combustion event. It should be noted that the AFT is primarily a function of the rate of change of species from reactants into products of combustion. Within this model, all of the changes in species are controlled by the Arrhenius expression governing the rate of combustion of fuel (Equation 85). As a result, when the rate of combustion decreases, the flame temperature will also tend to decrease.

The program then uses the mass of fuel left to calculate the mass fraction burned from the previous combustion cycle:

Mass Fraction Burned	$Y_{mb} = 1 - \frac{m_{f,rem}}{m_f}$	(120)

where $m_{f,rem}$ is the mass of fuel remaining at the end of the combustion cycle. This value is then compared to the combustion efficiency provided by the emissions analysis and Equation 50. To increase or decrease

the combustion speed of the process in order to achieve the correct mass fraction burned, the program changes the coefficient *K* in the expression for the fuel mass burn rate, given in Equations 83 and 85. The program then goes through two sets of iterations until the mass fraction of fuel burned and the provided combustion efficiency are equal.

The first iteration used is an approximation using the Newton-Raphson method. In this case, the variable *x* is replaced with the coefficient *K* used by the program to control the speed of combustion, and the function *g* is given by the following:

Change in Mass Fraction Burned Between Iterations	$g\big\vert_{x_n} = Y_{mb} - Y_{mb,a} = 0$	(121)

where $Y_{mb,a}$ is the actual mass fraction burned, obtained through a separate emissions analysis (i.e., combustion efficiency via Equation 49), and which is treated as a constant. Therefore, the solved mass fraction burned is assumed a function of *K* alone, and is simplified:

Definition of Mass Fraction Burned for a given Iteration	$Y_{mb}\big\vert_{K_n} = Y_{mb,n}$	(122)

where $Y_{mb,n}$ is the mass fraction burned associated with a given coefficient K_n.

At this point, the program develops an approximation for $g'|_{x_n}$. In reality, the mass fraction burned is a function of many separate variables, and the calculation of the actual derivative of the mass fraction burned would be significantly more difficult to derive. As a result, the program instead uses a finite difference approximation in place of the actual derivative:

Rate of Change of Cumulative Heat Release with respect to time.	$g'\big\vert_{x_n} = \frac{Y_{mb,n} - Y_{mb,n-1}}{K_n - K_{n-1}}$	(123)

This approximation changes the iterative method from Newton-Raphson into the secant method, but the computation is ultimately the same at this point. Combining Equations 120-123 allows the secant method to be rewritten explicitly for use in the model:

Newton-Raphson Iteration for Changing the Rate of Combustion	$K_{n+1} = K_n - \frac{Y_{mb,n} - Y_{mb,a}}{\left(\frac{Y_{mb,n} - Y_{mb,n-1}}{K_n - K_{n-1}}\right)} \; for\, n \geq 1$	(124)

It can be seen that in order to calculate the value of K_{n+1}, two previous iterations are required, such that the expression for K_2 is written as follows:

Newton-Raphson Method, First Iteration	$K_2 = K_1 - \frac{Y_{mb,1} - Y_{mb,a}}{\left(\frac{Y_{mb,1} - Y_{mb,0}}{K_1 - K_0}\right)}$	(125)

As a result, the program requires two iterations of the combustion function to "prime" the secant method approximation. The first of these two iterations uses a default value of K_0 to find $Y_{mb,0}$. At this point, the program compares the value obtained for $Y_{mb,0}$ and compares it to the actual mass fraction burned in order to provide a better guess for K_1. Once a value of K_1 is decided, the program then finds the associated mass fraction burned $Y_{mb,1}$, and is then able to use the approximation given by Equation 124 to iterate successive values of K_{n+1}. The program continues until the change in the mass fraction burned between successive iterations is negligible (1E-5).

3.3.8 Post Processing and Data Storage

Following the end of the combustion-related calculations, the program calculates the work output, internal energy, and heat transfer of the system from IVC to EVO. The system calculates the instantaneous change in work between two time steps through a numerical approximation of Equation 14, using the trapezoidal rule [3]:

Rate of Work Done, Single Zone	$dW_i^k = 0.5 \cdot \left(p^k + p^{k-1}\right) \cdot (\forall_i^k - \forall_i^{k-1})$	(126)

The total work done within the control volume is found similarly, and uses the change in volume of the cylinder as a whole instead of the change in volume of a zone. Alternatively, the change in work done at a given crank angle is equal to the sum of the work done by each zone:

Rate of Work Done, Control Volume	$dW_{cv}^k = 0.5 \cdot \left(p^k + p^{k-1}\right) \cdot (\forall_{cv}^k - \forall_{cv}^{k-1}) = \sum_i dW_i^k$	(127)

The total amount of work done in a zone, or over the total control volume, is the sum in the change in work between time steps for the zone, or for the total volume:

Cumulative Work Done, Single Zone	$W_i = \sum_k dW_i^k$	(128)

Cumulative Work Done, Control Volume	$W_{cv} = \sum_k dW_{cv}^k$	(129)

Additionally, the program calculates the gross power output of the system (in kW) by dividing the work done per cycle by the total time of the cycle:

Gross Power Output	$P_g = W_{cv} \cdot 10^{-3} \cdot \frac{N\,rev}{1\,min} \cdot \frac{1\,min}{60\,sec} \cdot \frac{1\,cycle}{n_R\,rev} = W_{cv} / t_{cycle}$	(130)

With the work known, the program calculates a number of engine characteristics, such as the gross indicated mean effective pressure ($IMEP_g$, in bar) and brake-specific fuel consumption ($BSFC_g$, in $g \cdot kW^{-1} \cdot h^{-1}$):

Indicated Mean Effective Pressure, Gross	$IMEP_g = W_{cv} / \forall_d \cdot 10^{-5}$	(131)
Brake Specific Fuel Consumption, Gross	$BSFC_g = \frac{\dot{m}_f}{P_g} \cdot \frac{3600\,sec}{1\,hr} \cdot \frac{1000\,g}{1\,kg}$	(132)

The change in internal energy follows an approximation similar to that used for the change in work, following Equation 10:

Rate of Change in Internal Energy, Single Zone	$dU_i^k = T_i^k \cdot c_{v.i}^k \cdot \left(m_i^k - m_i^{k-1}\right) + m_i^k \cdot c_{v.i}^k \cdot \left(T_i^k - T_i^{k-1}\right) + T_i^k \cdot m_i^k \cdot \left(c_{v.i}^k - c_{v.i}^{k-1}\right)$	(133)

Summing over all three zones will allow for calculation of the change in internal energy between steps, the total internal energy within a zone over the cycle, and the total internal energy within the cylinder volume:

Rate of Change in Internal Energy, Control Volume	$dU_{cv}^k = \sum_i dU_i^k$	(134)
Cumulative Change in Internal Energy, Single Zone	$U_i = \sum_k dU_i^k$	(135)
Cumulative Change in Internal Energy, Control Volume	$U_{cv} = \sum_k dU_{cv}^k$	(136)

The rate of change in energy due to fuel injection and vaporization follows Equation 25:

Rate of Change in Fuel Enthalpy from Injection	$h \cdot dm_{f,inj}\Big\|^k = \left[h_{fg} + \left(T_{vap} - T_{inj}\right) \cdot c_f + \left(T_f^k - T_{vap}\right) \cdot c_{p,f}^k\right] \cdot \dot{m}_{f,inj} \cdot t_{step}$	(137)

utilizing the mass flow rate of injection multiplied by the size of the time step. The total change is therefore:

Cumulative Change in Fuel Enthalpy from Injection	$dH_{inj} = \sum_k h \cdot dm_{f,inj}\Big\vert^k$	(138)

The approximation for the change in heat transfer between time steps follows Equations 16 and 23 closely. However, heat transfer is presumed to occur between the walls and the bulk gas as a whole, so the change in heat transfer cannot be broken down into zones. The overall heat transfer is dependent on whether or not the luminous flame exists, as determined by the existence of the adiabatic flame temperature:

Rate of Convective Heat Transfer	$dQ_{ht,con}^k = h_c^k \cdot \frac{t_{step}}{\Delta\theta} \cdot A_s^k \cdot \left(T_{cv}^k - T_w^k\right)$	(139)
Rate of Emissive Heat Transfer	$dQ_{ht,rad}^k = \sigma \cdot \frac{t_{step}}{\Delta\theta} \cdot A_s^k \cdot \left[\varepsilon_g \left(T_{cv}^k\right)^4 - \alpha_w \left(T_w^k\right)^4\right] \; for \; \varepsilon_g \left(T_{cv}^k\right)^4 > \varepsilon_{fl} \left(T_{fl}^k\right)^4$	(140)
Rate of Luminous Heat Transfer	$dQ_{ht,rad}^k = \sigma \cdot \frac{t_{step}}{\Delta\theta} \cdot A_s^k \cdot \left[\varepsilon_{fl} \left(T_{fl}^k\right)^4 - \alpha_w \left(T_w^k\right)^4\right] \; for \; \varepsilon_g \left(T_{cv}^k\right)^4 < \varepsilon_{fl} \left(T_{fl}^k\right)^4$	(141)
Total Rate of Heat Transfer	$dQ_{ht}^k = dQ_{ht,con}^k + dQ_{ht,rad}^k$	(142)

The emissivity of the flame is set to 0.6, as recommended by Woschni [111]. Finally, the total heat transfer for the volume is defined as the sum of the change in heat transfer between time steps over the entire cycle:

Cumulative Heat Transfer	$Q_{ht} = \sum dQ_{ht}^k$	(143)

As the change in heat transfer can only be calculated for the bulk gas, the temperature used for heat transfer must be the temperature of the bulk gas within the control volume (T_{cv}^k). The coefficient h_c^k is calculated using three separate functions; one each for Woschni's and Hohenburg's correlations, and one for the average of the two correlations. The emissivity of the gas is calculated using (through Equation 17), and the absorptivity of the cylinder walls is taken from tabulated values (normally 0.37 for steel) [134]. The surface area of the cylinder at a given time is also known through Equations 19-21.

The model can now calculate the overall RHR of the system. The change in heat release between two time steps is defined as the sum of the changes in internal energy, work, and heat transfer between those same two time steps:

Rate of Heat Release	$dQ_{hr}^{k} = dU_{cv}^{k} + dW_{cv}^{k} + dQ_{ht}^{k} + h \cdot dm_{f,inj}\Big\vert^{k}$	(144)

Finally, the total energy released from the system is the sum of the change in HR between time steps over the entire cycle:

Cumulative Heat Release	$Q_{hr} = \sum dQ_{hr}^{k}$	(145)

At this point, the program calculates a gross measure of energy accountability, relating the total amount of HR indicated by the program with the approximate amount of energy expected from the combustion of a known amount of fuel:

Gross Energy Accountability	$\eta_q = \frac{Q_{hr}}{m_{f,cons} \cdot Q_{LHV}} = \frac{Q_{hr}}{m_f \cdot Y_{mb} \cdot Q_{LHV}}$	(146)

where $m_{f,cons}$ is the total amount of fuel used up in the reaction (which is equal to the total mass of fuel injected multiplied by the mass fraction burned and the lower heating value). Any value of η_q other than one indicates a mismatch in the amount of energy that should be liberated from combustion of a set amount of fuel. Hence, the program will adjust the convective heat transfer coefficients, resolving Equations 139-143, before recalculating the total RHR given in Equation 144, the sum of HR from the cycle through Equation 145, and finally recalculating the energy accountability. For example, if η_q is found to be above one, then the amount of energy being given off by the fuel is above the energy content of the burned fuel. The program repeats this process until the total amount of HR matches the total possible energy content of the combusted fuel.

Note that energy accountability η_q and the combustion efficiency η_c are not equivalent. The combustion efficiency is a ratio of the total energy actually provided to the theoretical maximum energy output of the fuel, and gives an indication of the total mass fraction burned over the cycle. Meanwhile, the gross energy accountability is a ratio of the actual energy output of the model to the energy input of the

true amount of fuel consumed, and acts as a measure of the model's reliability, rather than the engine's actual efficiency.

From this information, the program is able to calculate the various efficiencies of the engine cycle. From its definition, the program calculates the gross thermal efficiency of the engine cycle, using the calculated HR as Q_{in}:

Gross Thermal Efficiency	$\eta_t = W_{out} / Q_{in} = W_{cv} / Q_{hr}$	(147)

Next, the program calculates the gross fuel conversion efficiency, or the ability of the engine to extract energy from the fuel molecules, using Q_{lhv}, P_g, and the mass flow rate of fuel:

Gross Fuel Conversion Efficiency	$\eta_f = \frac{P_g}{\dot{m}_f \cdot Q_{lhv}}$	(148)

From these efficiency values, the program calculates the gross combustion efficiency of the engine cycle by rewriting the equation for the constant ζ (Equation 48) used for determining the global chemical reaction.

Experimental Combustion Efficiency	$\eta_c = 1 - \frac{\zeta}{\xi}$	(149)

In this way, the final combustion efficiency will match the combustion efficiency measured by the program used to record the pressure trace. This value is also compared to the theoretical combustion efficiency, given as the ratio between the fuel and thermal efficiencies:

Theoretical Combustion Efficiency	$\eta_c = \eta_f / \eta_t$	(150)

The program then exports the collected outputs into a final text file detailing the test for the user.

3.3.9 Graphical User Interface

The model was built in MATLAB in three tiers. The first tier takes the form of a graphical user interface (GUI), and is responsible for collecting information from the user in order to run the program, as well as displaying information upon completion of a full iteration of the HR program. The GUI is subdivided into multiple subsections, allowing for the toggle from different ignition delay correlations, cylinder wall temperature settings, fuels, and engines. In addition, the user has the option to change a

number of variables to improve model speed and stability, and can choose to show extra figures, or save the results of the iteration. Finally, the user must specify the files to be read in for use in the program (such as the pressure trace, and the testing specifications used). When the computation of the engine HR is completed, the GUI displays a graph of the work, heat transfer, and change in internal energy over a single cycle, as well as displaying numerical values for the components of HR, gross engine characteristics, and additional useful information on the cycle (see Figure 13). The GUI also serves to display warning messages if a file necessary for the HR computation is not available.

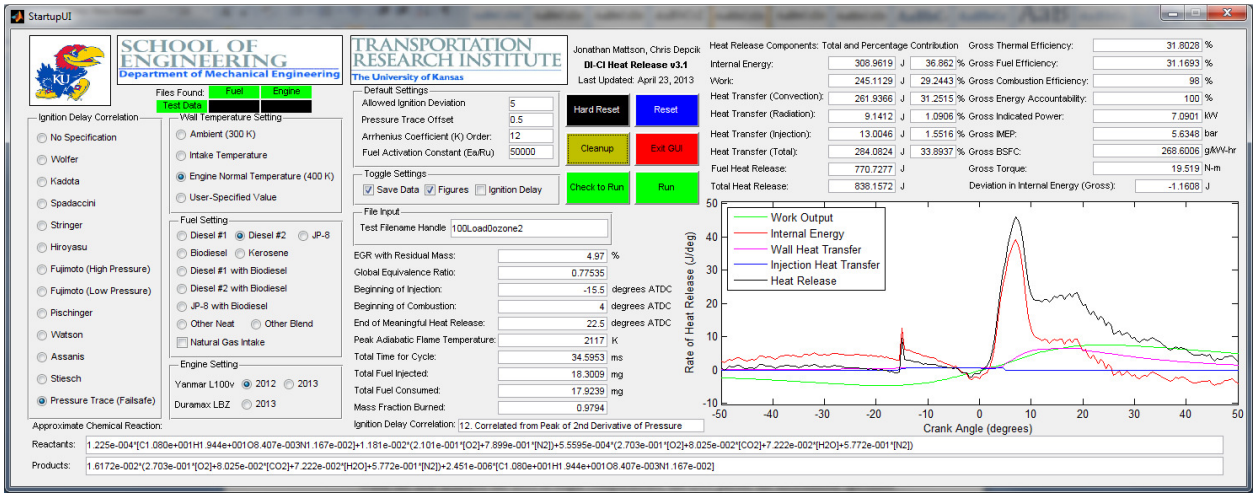

Figure 13. The GUI used as an interface between the User and the HR model in MATLAB.

When the user instructs the GUI to begin computations, the GUI passes the information specified by the user to the second tier of the program, which serves as the primary code for reading and analyzing the input data. This information is then communicated to the third tier, which consists of multiple sub-functions, each of which is responsible for a unique set of calculations. This third tier of small, individualized functions are much more straightforward to replace and update, and are written such that the output of one function will serve as the input of subsequent functions, with the goal of providing all of the necessary thermodynamic information needed to calculate each of the terms provided in Equation 5 for the close portion of the engine cycle. The second tier then serves to collect and organize these outputs into a single result, which can then be saved for later use. The second tier is also responsible for creating a

number of graphs and figures that the user can access for more detailed information on the engine cycle, such as the temperature, mass, or volume of the zones within the cylinder.

3.4 Results and Discussion

It was necessary to perform an initial validation of the program against existing data from testing of diesel fuel in a Yanmar 435 cc diesel engine. All tests were done with diesel fuel #2 ($C_{10.8}H_{18.7}$) in the chemical reaction calculations with an assumed lower heating value of 43,000 kJ kg^{-1}. No EGR was used in any of the tests and the engine operated unthrottled at 16.75 N-m of net torque for the engine load.

This earlier testing provided a number of pressure traces appropriate for use in the program (the engine parameters can be found in Table 8). Associated with this data were engine parameters including the influence of the pumping loop not factored into the HR program that could be compared against the program's output, such as output power, net brake-specific fuel consumption ($BSFC_n$), fuel conversion efficiency, combustion efficiency, and thermal efficiency. Additionally, the experimental program used to gather the pressure traces also calculated W_{cv}, as well as $IMEP_g$ [11].

Table 8. Yanmar L100v Engine Parameters.

Engine Bore [cm]	8.6
Stroke [cm]	7.5
Displacement [cc]	435
Connecting Rod Length [cm]	18.8
Crank Arm Length [cm]	3.8
Clearance Volume [cc]	21.611
Compression Ratio	21.2
Injection Timing [° ATDC]	-15.5
Intake Valve Closing [° ATDC]	-122
Exhaust Valve Opening [° ATDC]	144
Residual Fraction	0.0497
Engine Strokes per Cycle	4

The output W_{cv} of the engine was found to be 244 J $cycle^{-1}$, identical to the work given by the program used to read the pressure traces. Similarly, $IMEP_g$ from the HR program was found to be 5.619 bars in comparison to 5.607 bars, as expected since the experimental program does not include a pressure trace filtering process. The HR calculations allow for comparison of the work in each of the three zones (see Figure 14). The burned zone provides 437 J $cycle^{-1}$ in gross work, while the unburned zone results in

-192.94 J cycle^{-1} of work. The fuel zone did not have a significant amount of work, providing only -0.122 J cycle^{-1}. This is due to the small presence of the fuel mass within the cylinder during the entirety of the combustion cycle. Together, the work done accounted for 29.47% of the anticipated HR.

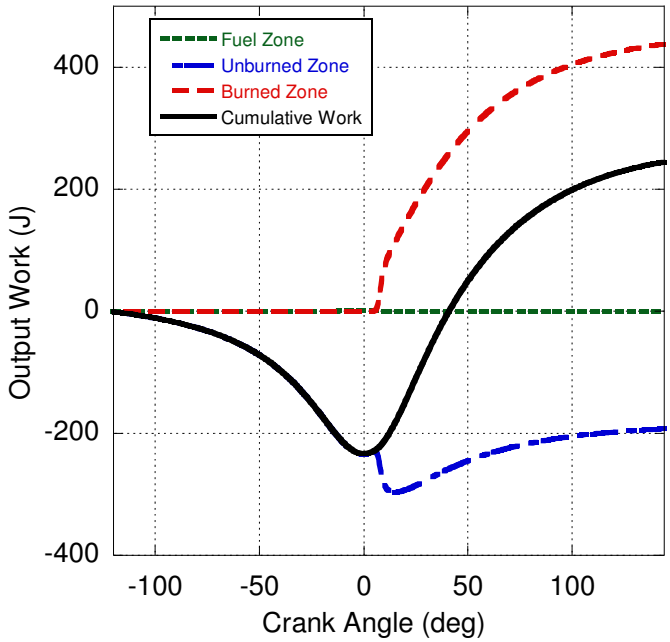

Figure 14. Summation of work done per time step by (or on) the fuel, unburned, burned, and total volumes from IVC to EVO, during a 100% engine load test without turbocharging.

The three correlations for convective heat transfer used by the program resulted in very similar patterns of heat transfer for the system, with the Woschni correlation providing the most amount of heat transfer. In calibration, h_c was raised to be 15.9% higher than indicated by the original calculation of the average of the two coefficients. This resulted in a net 280 J cycle^{-1}of convective heat transfer out of the system, and 250 J cycle^{-1} after ignition (see Figure 15). Heat transfer by radiation was small, at only 7.13 J cycle^{-1}, and heat transfer due to the injection of fuel accounted for an additional loss of 12.7 J cycle^{-1}. Radiation was largely due to flame luminosity during combustion, which was also the only portion of the cycle where the Stark Number for the system fell below 100. While low, this amount of radiative heat transfer is not unexpected, as radiative heat transfer has occasionally been neglected in CI engines [111]. All together, heat transfer to the cylinder walls, and through injection accounts for 301 J cycle^{-1} of the

total HR, indicating a 36.29% loss due to heat transfer. Of this heat transfer, 93.0% was due to convection, 2.37% was due to radiation, and the remaining 4.22% was due to the injection of fuel.

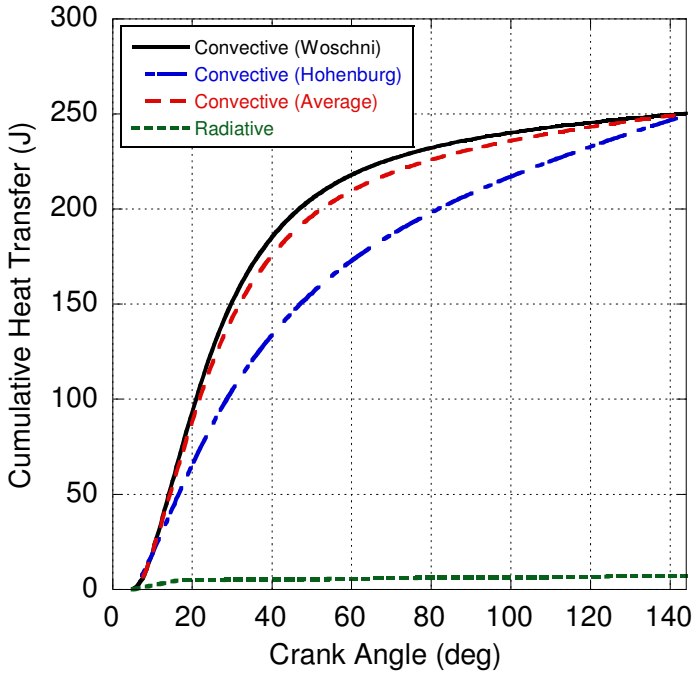

Figure 15. Cumulative heat transfer to the cylinder walls after ignition until EVO using calibrated correlations for heat transfer during a 100% load test without turbocharging.

The gross change in internal energy was found to be 283.94 J cycle^{-1}, representing the energy left unused within the cylinder that is lost to the exhaust when EVO occurs (see Figure 16). The vast majority of the change in internal energy is found within the burned zone, with a gross change in internal energy of 338.78 J cycle^{-1}, with the unburned zone balancing the system with a gross change of -55.4 J cycle^{-1}. This loss of energy in the unburned zone is due to mass that is transferred due to entrainment and combustion. The change in the fuel zone, at 0.55 J cycle^{-1} from IVC to EVO, is again much smaller than the change experienced by the burned zone. However, the fuel zone does experience a large positive change due to injection, and an equally large change from combustion, due to the rapid change in the total mass of the fuel zone. The components of internal energy account for 34.23% of the anticipated HR.

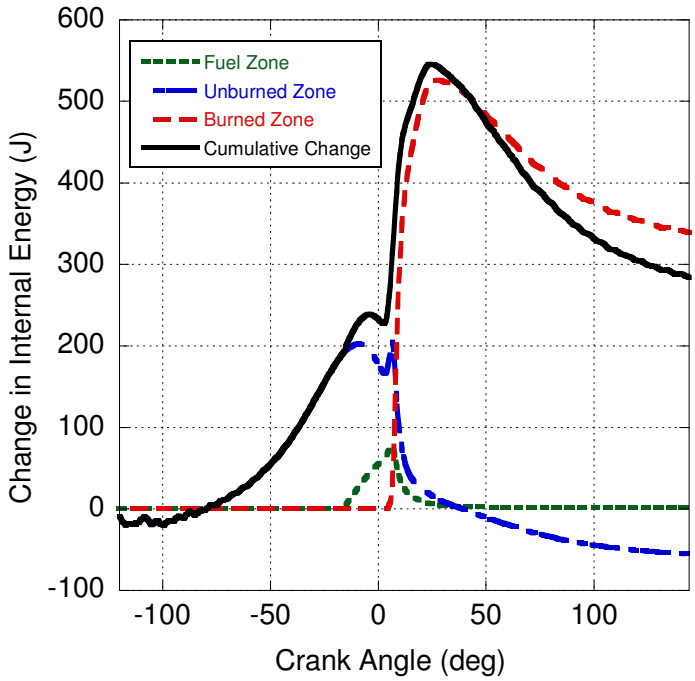

Figure 16. Summation of the change in internal energy per time step from IVC to EVO for the fuel, unburned, burned, and total volumes during a 100% engine load test without turbocharging.

The cumulative HR calculated by the program was 829.5 J cycle^{-1} after calibrating the heat transfer coefficient. Of this heat release, 771 J cycle^{-1} were from the combustion of fuel, and the remainder was due to convective heat transfer to the walls before the onset of combustion. The error in calculated and anticipated HR (by Equation 146) amounted to a difference of $8 \cdot 10^{-4}$%. From this, η_t was found to be 31.70%, η_f was 31.08%, and η_c was 98%. The difference between the theoretical η_c and the anticipated efficiency was less than 0.07%.

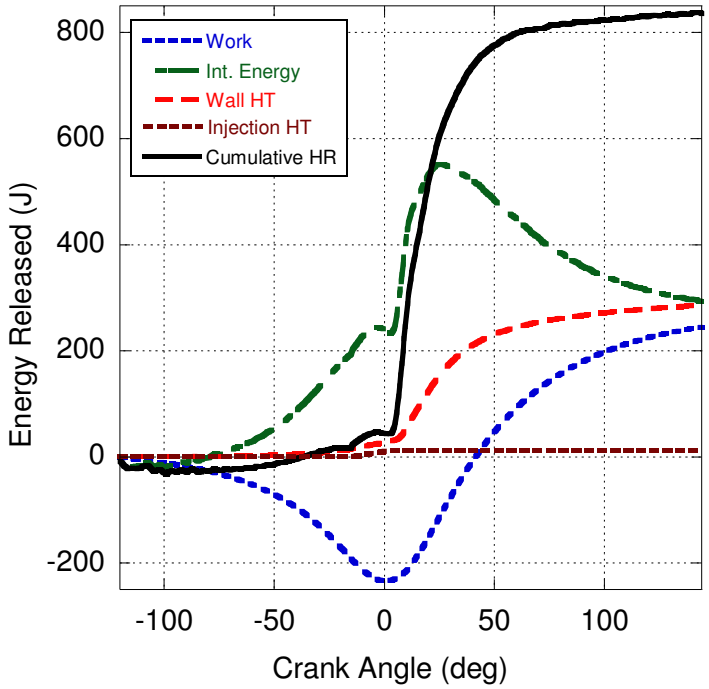

Figure 17. Components and summation of HR from IVC to EVO during a 100% engine load test without added turbocharging.

3.4.1 Variable Loading

In order to explore the fidelity of the HR program, experimental data from two separate load sweeps (one with turbocharging, and one without) were analyzed. Neither case utilized EGR. For the non-turbocharged case, as the amount of load increased (from 0.5 N-m to 16.75 N-m of net torque), the time of ignition moved forwards by one degree of crank angle from 6° to 5° ATDC. This movement of the ignition event is in part due to the engine slowing down as load increased (an aspect of the experimental setup that employed a generator rather than a dynamometer). Additionally, there is an increase in the amount of heat transfer in the cylinder causing hotter walls due to more fuel burned [11]. This increases heat transfer to the fuel vapor, subsequently promoting earlier ignition. Additional fuel was injected to allow for the engine to meet the prescribed loading, causing an increase in equivalence ratio from 0.270 at no load to 0.768 at full load. This change in equivalence ratio is also shown through the change in AFT, which rose from 1106 K in the unloaded engine to 2121 K in the fully loaded engine.

Over the loading study, HR rose from 262 to 830 J cycle^{-1}, and the RHR changed by approximately 67% (see Figure 18), with a cumulative change in internal energy rising from 30 to 284 J cycle^{-1} as load was increased. Heat transfer increased from 163 to 210 J cycle^{-1}, and output work also increased from 71 J cycle^{-1} at no load to 244 J cycle^{-1} at full load. As a result, $IMEP_g$ changed from 1.62 bar at no load to 5.62 bar at full load.

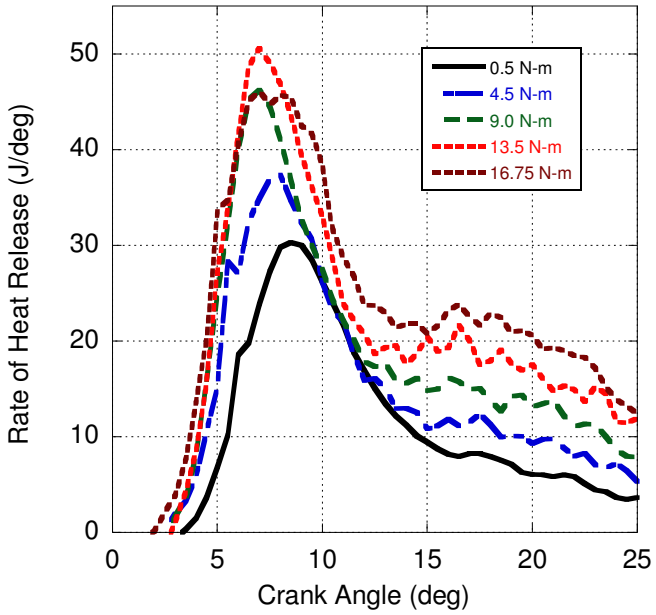

Figure 18. Rate of Heat Release from TDC to 25° ATDC at various engine loads under naturally aspirated conditions.

The gross output engine characteristics showed a general increase in efficiency as load increased (see Table 9). Some characteristics (primarily η_t and η_c) peaked at 13.5 N-m of load. Additionally, $BSFC_g$ was at its minimum at this load. Decreases in engine efficiency from further increases in loading were generally small. This loss in efficiency is largely due to the combustion event being air limited at high loads, making it more difficult for fuel to mix effectively with air. In addition, decreased engine speeds at high loading increase the amount of time available for heat transfer. This loss in efficiency can also be seen in the change in RHR of the diffusion burn at about 10° ATDC, at which point the RHR of the tests diverge and indicate a higher energy output from the higher loading. The premixed spike of the fully

loaded test is also significantly lower than the test at 13.5 N-m, but is also significantly longer, again indicating air-limited combustion.

Table 9. Engine output characteristics for varying engine load, without turbocharging.

Engine Load [N-m]	0.5	4.5	9.0	13.5	16.75
Thermal Efficiency [%]	29.05	29.69	31.95	32.49	31.70
Fuel Conversion Efficiency [%]	25.59	28.23	31.02	31.85	31.08
Combustion Efficiency [%]	88.06	95.07	97.07	98.06	98.07
Power Output [kW]	2.11	3.13	4.59	6.04	7.07
Gross Torque [N-m]	5.62	8.39	12.36	16.37	19.47
$IMEP_g$ [bar]	1.622	2.421	3.568	4.724	5.619
$BSFC_g$ [g/kW-hr]	327.2	296.6	269.9	262.8	269.3
Equivalence Ratio	0.270	0.362	0.487	0.626	0.768
Peak Cylinder Temperature [K]	1313	1376	1510	1608	1715

Tests with turbocharging yielded improved results. In these tests, the output load was matched to the five tests done without turbocharging, in order to compare the change in efficiency at each load. The time of ignition moved forward from 4° to 3° ATDC as load was increased (see Figure 19). Combustion started sooner with turbocharging, most likely due to the increased pressure and temperature within the cylinder leading to a lower overall amount of energy required for fuel autoignition. The peak cylinder temperature rose from 1313 to 1715 K with loading, with the decreased temperature over the naturally aspirated tests due to the decreased fuel flow rate, as well as the slightly increased flow rate from the turbocharger. This decrease is also mirrored in the lower equivalence ratios of the turbocharged tests, which ranged from 0.270 to 0.768 as loading was increased.

All efficiencies showed the same general trend as in tests without turbocharging, except that differences in efficiency between 13.5 and 16.75 N-m were negligible as combustion did not suffer as much from air limiting (see Table 10). Like the tests without turbocharging, the differences in efficiency can be traced to the RHR as a function of load. Again, the RHR for 13.5 and 16.75 N-m of load were significantly different, although they diverged from each other earlier (around 8° ATDC). The initial premixed spike in RHR grew as a function of load, before falling slightly at the highest loading, as the increased air from turbocharging inhibited the onset of air limiting. The differences in HR between

turbocharged and non-turbocharged tests was most striking at full load, where the total work done by the engine was identical, but the cumulative HR decreased by 7.5% with turbocharging, and the peak premixed RHR fell by almost 25%.

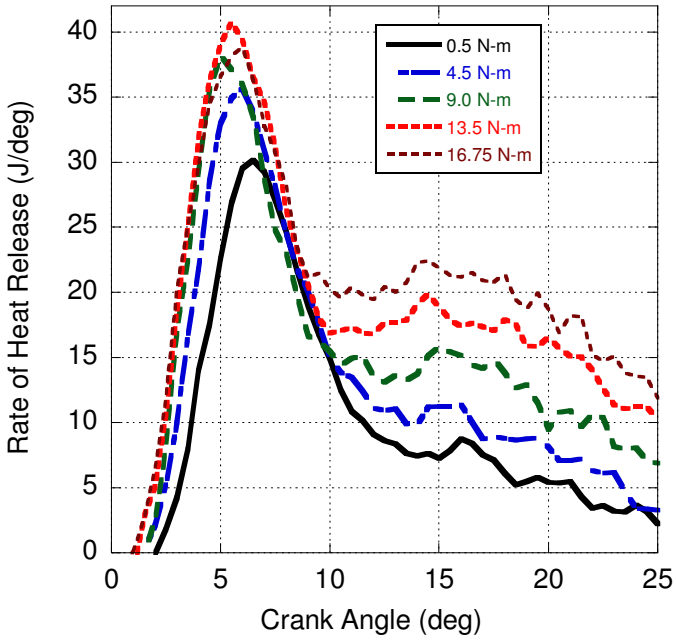

Figure 19. Rate of Heat Release from TDC to 25° ATDC at various engines load with added turbocharging.

Table 10. Engine output characteristics for varying engine load, with turbocharging.

Engine Load [N-m]	0.5	4.5	9.0	13.5	16.75
Thermal Efficiency [%]	27.62	31.79	33.69	34.60	34.37
Fuel Conversion Efficiency [%]	24.60	30.22	33.04	33.93	33.70
Combustion Efficiency [%]	89.06	95.07	98.07	98.07	98.07
Power Output [kW]	2.00	3.17	4.63	6.06	7.13
Gross Torque [N-m]	5.31	8.48	12.43	16.46	19.52
$IMEP_g$ [bar]	1.532	2.449	3.588	4.751	5.635
$BSFC_g$ [g/kW-hr]	340.4	277.0	253.4	246.7	248.4
Equivalence Ratio	0.253	0.323	0.429	0.540	0.661
Peak Cylinder Temperature [K]	1303	1376	1476	1565	1694

The cumulative mass fraction burned for each cycle was also plotted to show both the change in amount of fuel consumed within the cylinder, as well as to show the changing rate of combustion as the engine cycle progresses further from TDC. In general, the cumulative mass fraction burned at the end of

the cycle reflected the combustion efficiency of the cycle (see Figure 20). Additionally, the mass fraction burned tended to level off at around 30° ATDC, and was consistent across all engine loadings.

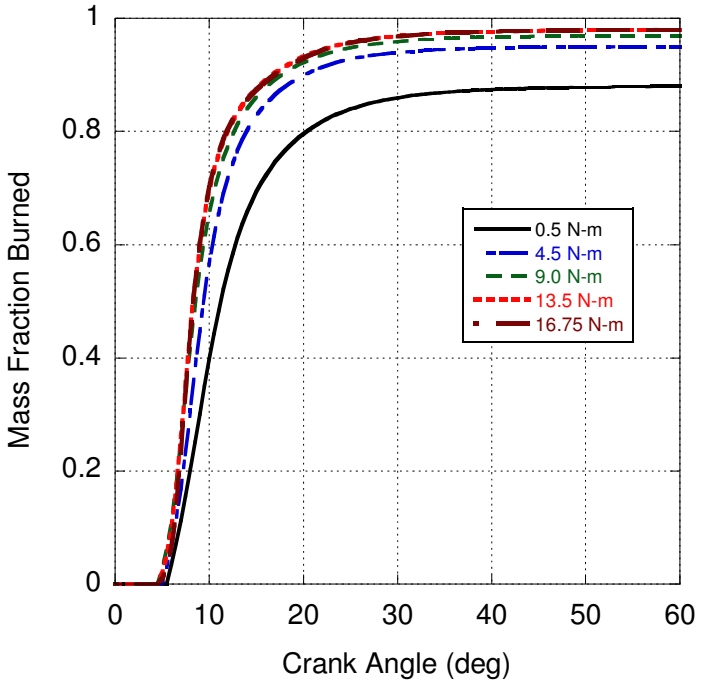

Figure 20. Cumulative mass fraction burned for varying loads, from TDC to 60° ATDC in tests without turbocharging.

3.4.2 Ignition Delay Correlation

The points of ignition anticipated by the ignition delay correlations were evaluated for tests without turbocharging at various engine loads, and are given in Table 11. The ignition delay correlation for low pressures provided by Fujimoto, Watson, and Assanis predicted the onset of combustion consistently within three degrees of crank angle of the timing expected by the maximum of the 2nd degree of the pressure trace. Of the available models, the correlation provided by Assanis (at low load) and Fujimoto (at high load), predicting the onset of combustion around one to two degrees of the pressure trace indicator. The remaining correlations were largely unable to predict the onset of combustion, most likely because the correlations were developed for constant-volume or single-droplet combustion tests, and do not account for other phenomena that may influence ignition delay.

Table 11. Onset of combustion with corresponding authors, as well as the point of ignition indicated by the pressure trace, evaluated in tests without turbocharging.

Engine Load	0.5	4.5	9.0	13.5	16.75
Engine Speed [RPM]	3591	3565	3545	3524	3470
Wolfer [135]	-3.0	-2.5	-3.5	-3.0	-4.0
Kadota [108]	-	-	-	-	-
Spadaccini [142, 143]	-14.5	-14.5	-14.5	-14.5	-14.5
Stringer [136]	-3.0	-2.5	-3.0	-3.0	-4.0
Hiroyasu [106]	-13.5	-13.5	-13.0	-13.0	-13.0
Fujimoto (High Pressure) [145]	-5.0	-5.0	-5.5	-5.0	-6.0
Fujimoto (Low Pressure) [145]	3.0	3.5	3.0	3.0	1.5
Pischinger [146]	-8.5	-8.0	-8.5	-8.5	-9.0
Watson [141]	0.0	0.0	-0.5	-0.5	-1.0
Assanis [134]	3.5	4.5	4.5	5.5	5.0
Stiesch [104]	14.0	15.5	13.0	12.5	12.0
Pressure Trace Indication	3.5	2.0	2.0	2.0	2.0

In turbocharging tests, very few correlations provided meaningful results, as expected due to an inability to account for the effects of mixture quality inherent with turbocharging [118]. The correlations that provided reasonable success in comparison to the pressure trace method are listed in Table 12. Again, the low pressure correlation provided by Fujimoto provided the best results, although the correlations of Watson and Assanis also fell within two to three degrees of the pressure trace indication.

Table 12. Onset of combustion with corresponding authors for varying percentages of rated engine load, as well as the point of ignition indicated by the pressure trace, for tests with turbocharging.

Engine Load	0.5	4.5	9.0	13.5	16.75
Engine Speed [RPM]	3598	3569	3558	3514	3488
Stringer [136]	-3.5	-3.0	-4.5	-4.0	-6.0
Fujimoto (High Pressure) [145]	-5.5	-5.5	-6.5	-6.0	-7.5
Fujimoto (Low Pressure) [145]	2.5	2.5	1.5	2.0	-0.5
Watson [141]	-1.0	-1.0	-1.5	-1.5	-3.0
Assanis [134]	2.5	3.0	3.0	4.0	3.0
Pressure Trace Indication	1.5	0.5	1.0	0.5	0.5

For low engine loading, the end of combustion was largely the same for all of the polytropic prediction methods (given by Equation 81), as well as the indication given by the drop in the AFT (signifying that the reaction was decelerating rapidly), and the minimum value of the 1st derivative of the pressure trace, as shown in Table 13. The AFT measurements tended to place the end of combustion consistently somewhere between 16° and 18° ATDC. As loading increased, the polytropic expansion

predictions gradually began to diverge from the others. For a given polytropic exponent, the duration of combustion increased as load was increased. Lower polytropic coefficients experienced a larger jump in combustion length between engine load settings, while higher coefficients experienced almost no difference as load was increased. Generally, a higher polytropic exponent indicated an end point of combustion in agreement with the AFT and 1st derivative of the pressure trace. In addition, the polytropic exponent in agreement with the pressure trace and AFT values increased as engine loading was increased, from a value of 1.2 at no engine load to 1.35 at full load. It is anticipated that the exponent would approach a value consistent with the expansion of pure air, indicating the more complete combustion of the cylinder contents (particularly fuel) as load is increased.

Table 13. End of combustion as indicated by the 1st and 2nd derivatives of the pressure trace, polytropic expansion, and AFT. All values are in degrees ATDC, except where marked.

Engine Load [% Load]	0.5	4.5	9.0	13.5	16.7
Engine Speed [RPM]	359	356	354	352	3470
Minimum of $dp/d\theta$	16.5	15.5	18.5	21.5	24.0
Minimum of $d^2p/d\theta^2$	11.0	10.0	9.5	9.5	10.0
Expansion, n=1.200	15.5	21.0	24.0	35.5	37.5
Expansion, n=1.225	15.0	20.0	23.5	33.5	37.5
Expansion, n=1.250	14.5	18.0	23.5	30.5	37.0
Expansion, n=1.275	14.0	14.0	22.5	27.0	32.5
Expansion, n=1.300	13.0	13.0	21.0	25.5	27.0
Expansion, n=1.325	12.5	12.0	13.5	23.5	24.5
Expansion, n=1.350	11.5	11.0	11.5	20.5	22.5
Expansion, n=1.375	6.0	10.5	10.5	10.5	12.0
Expansion, n=1.400	6.0	5.5	9.5	4.5	11.0
Back-step Polynomial	45.0	47.0	47.0	47.5	50.0
RHR Indication	16.0	15.5	16.5	17.5	19.0
90% of Total HR	26.0	36.5	38.5	47.5	58.0

3.4.3 Pressure Filtering

The program's calculations vary only slightly from the values collected by the pressure trace program. Much of this variance is most likely due to the unfiltered nature of the raw results provided by

the pressure trace. Additionally, the effect of the filtering used within the program can slightly lower the peak cylinder pressures, lowering all of the output HR terms slightly.

To this end, the program was rerun, with some filtering processes disengaged. After the unfiltered runs, the cumulative changes in internal energy were compared, as the change in internal energy is most susceptible to poor filtering of the pressure trace. On a test of the Yanmar L100v without turbocharging, the difference in the cumulative change in internal energy differed by 13 J cycle^{-1}, with the internal energy becoming more unstable as it approached EVO. In similar tests with turbocharging enabled, the unfiltered run showed a difference in the change in internal energy of 14.9 J cycle^{-1}, a net error of 8.69%. Like the tests without turbocharging, the cumulative change in internal energy became unstable at ignition, with error increasing as the cycle approached EVO.

3.4.4 Fuel Testing

The next testing done to validate the program was a comparison of various fuels other than traditional diesel fuel. As a result, the program was run using various previously acquired pressure traces from tests with jet propellant #8 (JP-8), n-heptane, neat unused cooking oil (UCO100), neat jatropha methyl-ester (JME100), and two blends of jatropha biodiesel with diesel fuel (JME5 for 5% biodiesel, and JME20 for 20% biodiesel), in addition to a baseline test of #2 diesel fuel. Each of the fuels was used in five different tests at various engine loads, in the same way as the tests described previously, with the exception of n-heptane, which could not be used for loads higher than 9.0 N-m. All tests were done without turbocharging, and the associated RHR can be seen in Figure 21 (0.5 N-m), Figure 22 (4.5 N-m), Figure 23 (9.0 N-m), Figure 24 (13.5 N-m), and Figure 25 (16.75 N-m). Diesel fuel served as the baseline for all tests, and was the only neat fuel to exhibit a decrease in ignition delay as engine load was increased due to the effects discussed earlier (see Figure 26). Ignition delay at no load was 6.5° ATDC, and fell to 5.0° ATDC at full load.

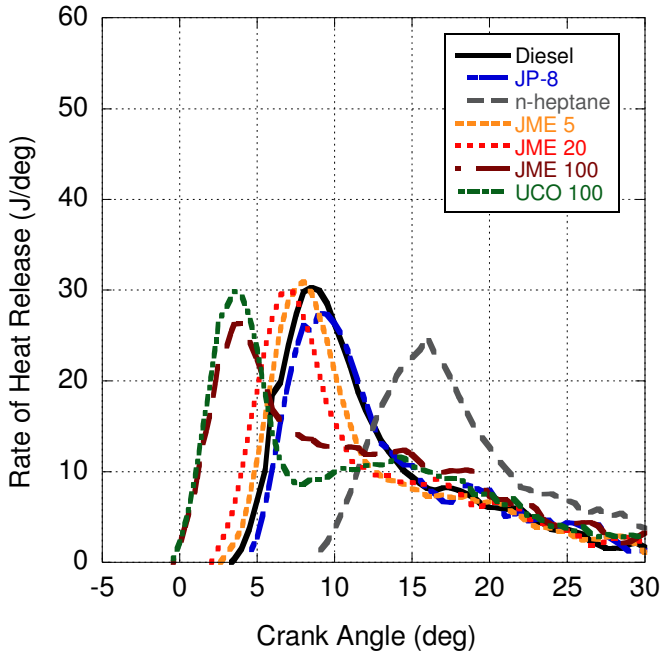

Figure 21. Rate of Heat Release at 0.5 N-m of loading for various fuels. Engine operated unthrottled and without turbocharging.

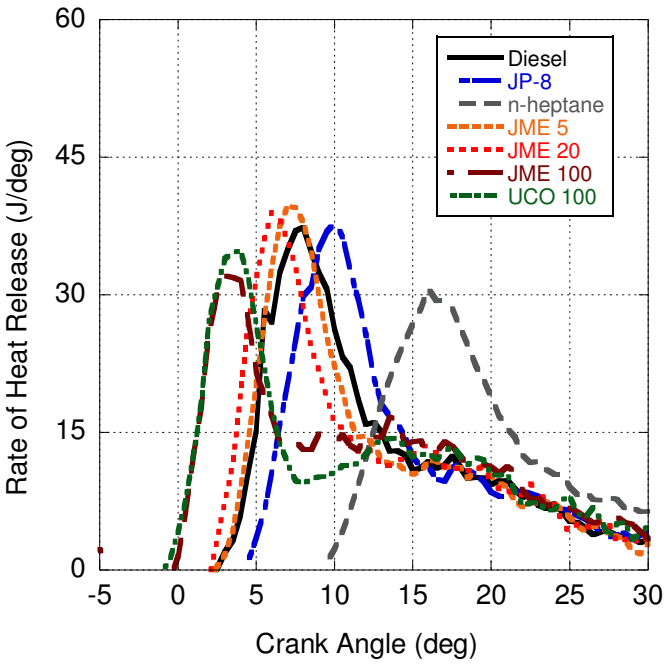

Figure 22. Rate of Heat Release at 4.5 N-m of loading for various fuels. Engine operated unthrottled and without turbocharging.

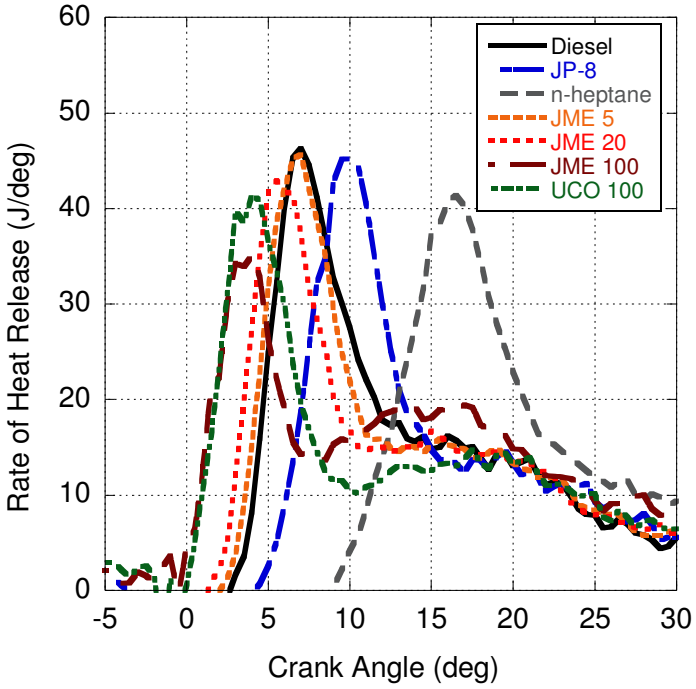

Figure 23. Rate of Heat Release at 9.0 N-m of loading for various fuels. Engine operated unthrottled and without turbocharging.

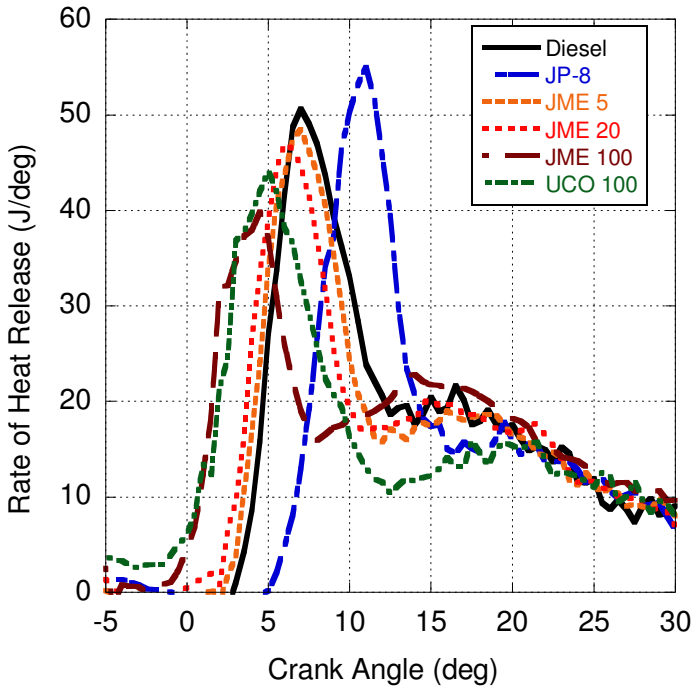

Figure 24. Rate of Heat Release at 13.5 N-m of loading for various fuels. Engine operated unthrottled and without turbocharging.

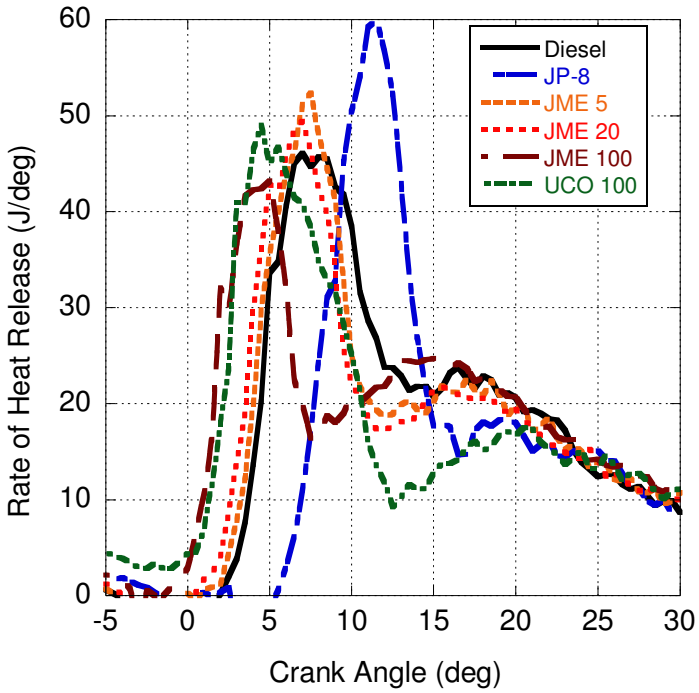

Figure 25. Rate of Heat Release at 16.75 N-m of loading for various fuels. Engine operated unthrottled and without turbocharging.

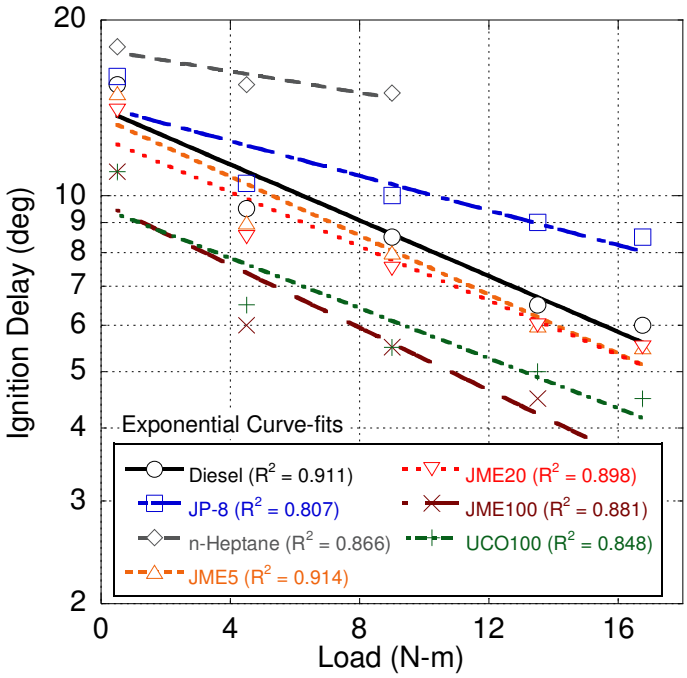

Figure 26. Ignition timing for fuel tests without turbocharging at varying engine loads, as indicated by the pressure trace.

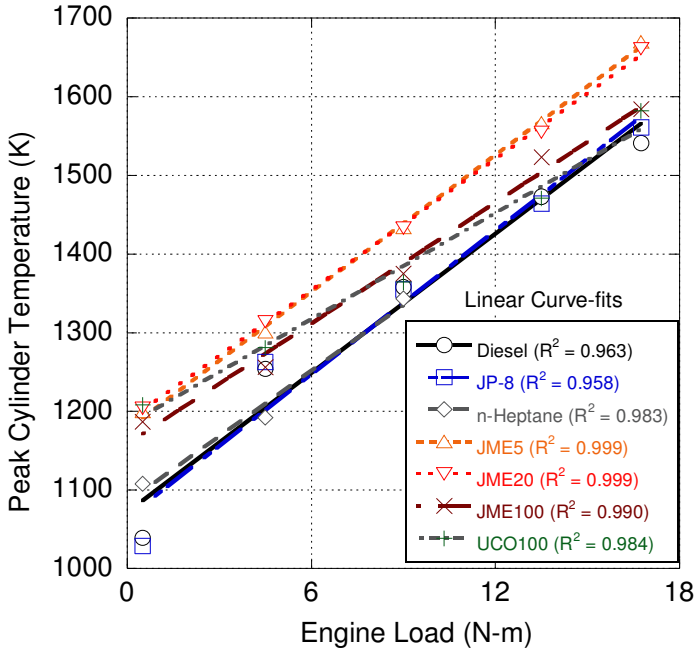

Figure 27. Peak cylinder temperature for fuel tests without turbocharging at varying engine loads.

Before a comparison can be done, it is necessary to understand the changes expected based off of the physical and chemical differences between the fuels used. To describe the ignition delay of a fuel species, researchers often use the Cetane Number of the fuel, with higher values corresponding to a (generally) shorter ignition delay. In terms of the physical ignition delay, viscosity will affect the ability of the fuel to break up and atomize after injection, and higher viscosity will lead to a more prolonged atomization. After fuel break up is achieved, then the fuel volatility (quantified through the fuel's flash point) will affect the readiness of the fuel to vaporize within the cylinder, with higher flash points indicating less volatile fuels. After the physical ignition delay period is exceeded, chemical effects begin to play a part. This is most apparent in the energy content of fuel, but can also be seen in other various chemical aspects such as the oxygen content of the fuel, or the number of double bonds present within the fuel molecule, both of which are properties largely unique to fatty acid methyl esters within biodiesel fuels.

While the factors that bring about changes in ignition delay vary widely, their effect is a net shift in combustion timing towards or away from TDC. In this way, fuels with shorter ignition delays generally experience higher peak pressures and temperatures.

Fuel ignition delay, however, is not the only property that can affect combustion timing. In the case of a mechanical fuel injection system, as was used during testing, changes in fuels can bring about changes in the injection profile. For example, changes in fuel density cause changes in the amount of mass injected in the cylinder, due to most fuel injection systems operating on a volumetric basis. As density increases, more mass is injected into the cylinder, resulting in a higher fuel consumption, as well as a higher temperature. Related to the density is the bulk modulus of compressibility, which can bring about changes to injection timing itself in mechanical fuel injection systems, which rely on the propagation of a pressure wave through the fuel media which moves the injector needle, allowing fuel to flow into the cylinder. Fuels with higher density (and typically higher bulk moduli of compressibility) will be injected somewhat earlier, leading to combustion closer to TDC, and higher peak temperatures. Fuel viscosity also plays a small part in injection timing as well, particularly if viscosity is low enough for fuel to leak through the pumping mechanism, leading to a slower rise in pressure and delaying injection timing, resulting in later and lower temperature combustion. A summary of the literature values of each of these characteristics for a number of fuels is presented in Table 14 [70, 155].

Table 14. Literature characteristics of various fuels and fuel blends tested. All values measured at standard pressure and 300 K.

Fuel Choice	Diesel	JP-8	n-Heptane	JME5	JME20	JME	UCO
Density [kg/m^3]	831	801	680	849	860	882	878
Cetane Number	42.3	44.5	56.0	45.8	46.0	51.0	52.8
Flash Point [K]	319	333	269	398	431	441	473
Kinematic Viscosity [cSt]	2.27	1.29	0.719	3.43	3.61	4.42	4.85
Lower Heating Value [kJ/kg]	41530	42700	44600	41380	40910	38450	36210
Oxygen Content [%]	-	-	-	0.6	2.3	11.0	10.5

Of the two alternate mineral fuels, JP-8 showed characteristics most similar to diesel fuel, as expected due to its similar composition [156]. While the Cetane Number and lower heating values for JP-8 are slightly higher, the density, flash point, and viscosity all lead to a slightly increased ignition delay, resulting in a delayed combustion event, and which is backed by the findings of the HR model. The n-heptane fuel presents a more extreme version of these same differences: while the Cetane Number, lower

heating value, and flash point all indicate that n-heptane would be a more useful fuel, the very low viscosity and density serve to counter these extreme benefits, resulting in a large delay in combustion timing between diesel and n-heptane. This is primarily due to the effect of low density and viscosity on the fuel injection event, causing fuel to be injected much later than is desired.

The two neat oxygenated fuels both showed characteristics very different from diesel fuel. The viscosity and flash points were significantly higher than diesel for both fuels, and the energy content is generally lower than diesel, resulting in a long physical ignition delay due to prolonged break up and vaporization. However, the high Cetane number and density serve to lower ignition delay significantly [157, 158]. In addition, the high oxygen content seen in biodiesel fuels (typically on the order of 10%) serves to drastically lower the chemical ignition delay, with the net effect of lowering the ignition delay of the biodiesel fuels below that diesel in spite of their less optimum characteristics [104, 106, 134].

The two blended fuels showed characteristics similar to diesel fuel, but with some added benefits of jatropha biodiesel. In particular, both blends saw increases in density, Cetane Number, flash point, and viscosity, with only slight penalties to energy content. In addition, the small percentage of biodiesel fuel served to yield significant oxygen content to the fuel, resulting in a net decrease in ignition delay that grew larger with increasing biodiesel content.

The change in physical and chemical properties of the fuels also caused a change in behavior with changes in load. Generally, a fuel will see a shorter ignition delay as load is increased, and this change is usually not linear, particularly in mechanical injection systems (see Figure 26). As load is changed, peak temperature is also shifted, although the relationship between load and temperature is typically more linear (as higher temperatures are a direct result of additional fuel) as shown in Figure 27. This peak temperature change produces an exponential change in ignition delay, as given by the Arrhenius ignition delay function (see Equation 77), in addition to the changes in ignition timing due to the mechanical pumping system. The net effect of these changes in peak temperature and ignition delay is then reflected directly in the changing RHR of the fuels.

These non-linear changes in ignition delay are readily apparent in each of the fuels, and can be traced back to their properties. Both the JP-8 and n-heptane suffered as load was increased, in spite of their higher Cetane Numbers, due to their lower densities and viscosities delaying injection timing, resulting in a delayed ignition timing (despite a shorter ignition delay). This limitation was particularly severe for n-heptane, to the degree where the engine could not operate at loads higher than 9.0 N-m. The oxygenated fuels both suffered from the same delays in injection timing (and ignition timing) as load was increased, although in this case it was most likely due to the increased density and viscosity. In effect, the neat alternative fuels saw less of a fall in ignition delay than diesel fuel, due to later injection.

The two blended fuels exhibited characteristics very similar to mineral diesel fuel. In addition, both blends benefitted from the high diesel component, in that neither fuel suffered from increases in ignition timing as load was increased, highlighting the similarity between their fuel properties to diesel fuel. In addition, this shows the ability of low-content biodiesel blends to balance oxygen content, Cetane Number, and increased density (which are beneficial to ignition delay) with the negative effects of higher viscosity, higher flash point, and lower energy content. Both fuels also saw decreases in ignition delay as load was increased, much in the same manner as mineral diesel fuel.

3.4.5 Exhaust Gas Recirculation

A final round of validation was done with tests with varying percentages of cooled EGR used. In these tests, the engine load was set to a given percentage of rated load under normal operating conditions using diesel fuel #2. Then, EGR was added, and the fuel flow rate was adjusted slightly in order to return the load to its chosen specifications. Load was varied from 4.5 N-m to 16.75 N-m (25% to 100% of rated load). The resulting RHR for these tests can be seen in Figure 28 (4.5 N-m), Figure 29 (9.0 N-m), Figure 30 (13.5 N-m), and Figure 31 (16.75 N-m).

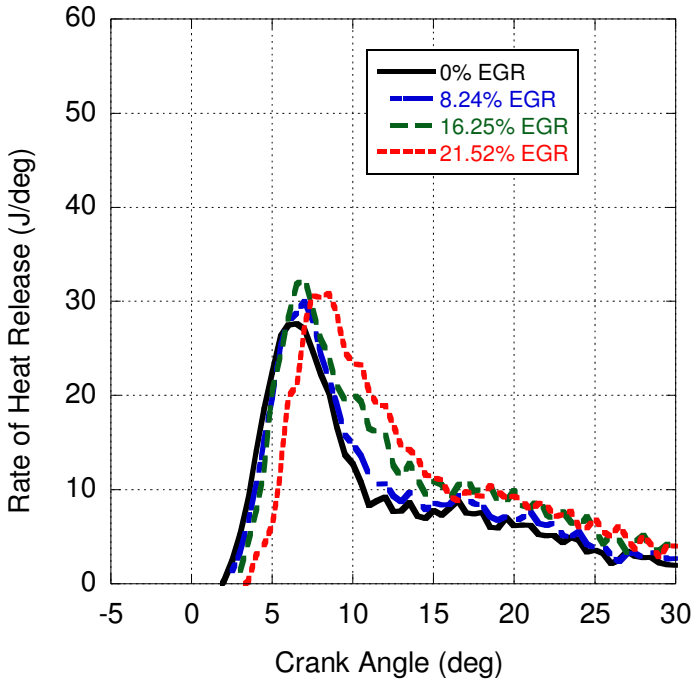

Figure 28. Comparison in the RHR for varying percentages of EGR, without turbocharging, and at 4.5 N-m of engine load.

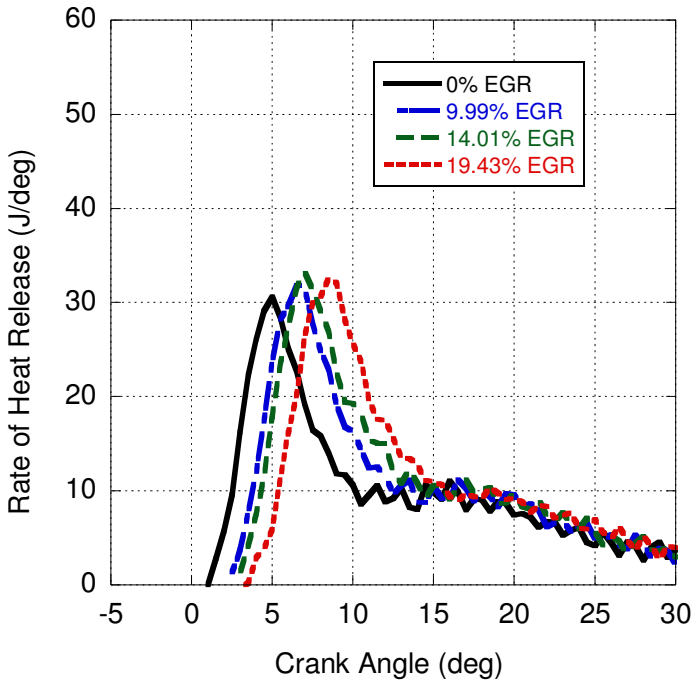

Figure 29. Comparison in the RHR for varying percentages of EGR, without turbocharging, and at 9.0 N-m of engine load.

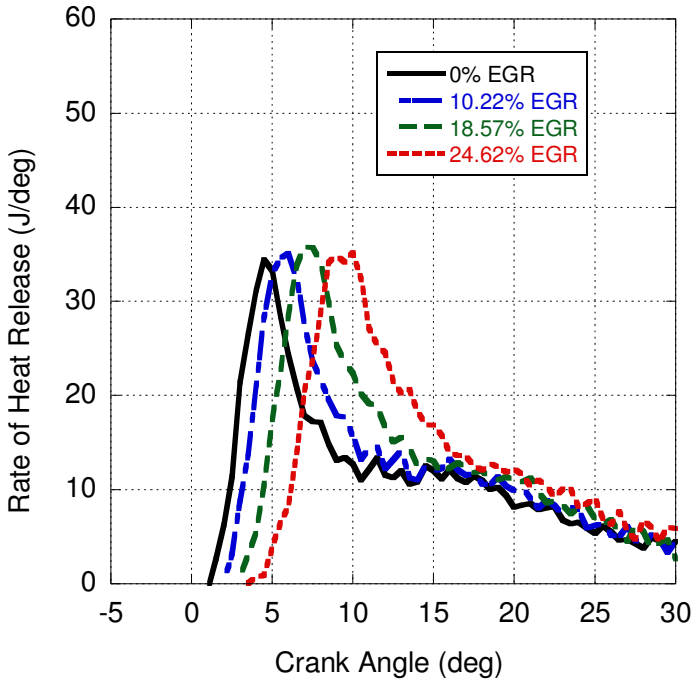

Figure 30. Comparison in the RHR for varying percentages of EGR, without turbocharging, and at 13.5 N-m of engine load.

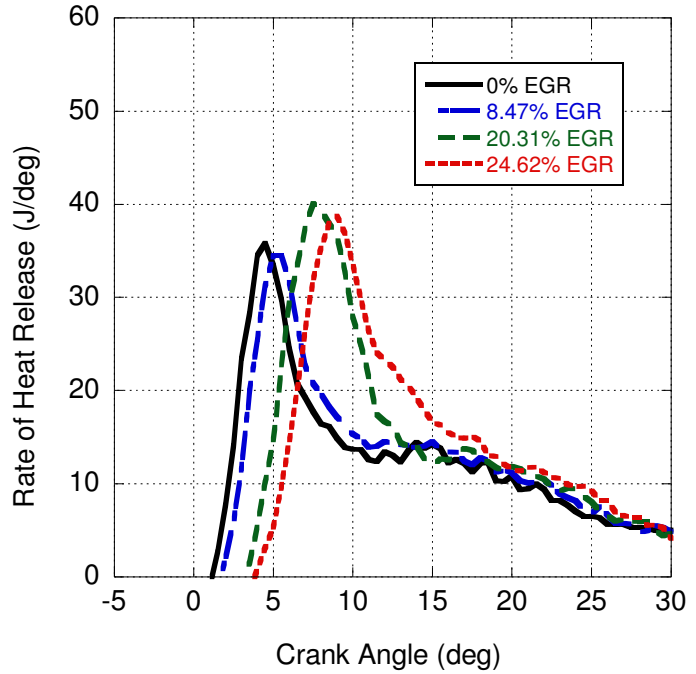

Figure 31. Comparison in the RHR for varying percentages of EGR, without turbocharging, and at 16.75 N-m of engine load.

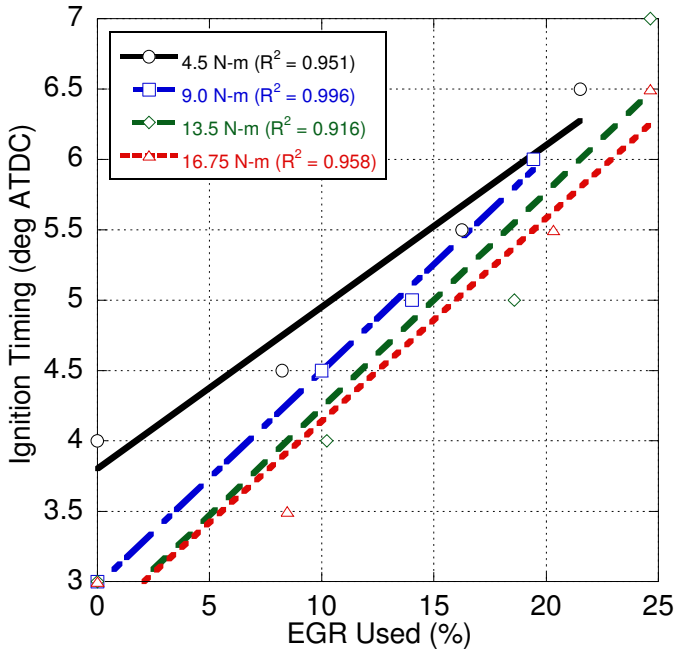

Figure 32. Comparison in ignition timing for varying percentages of EGR at each engine load. Tests run on a throttled engine without turbocharging.

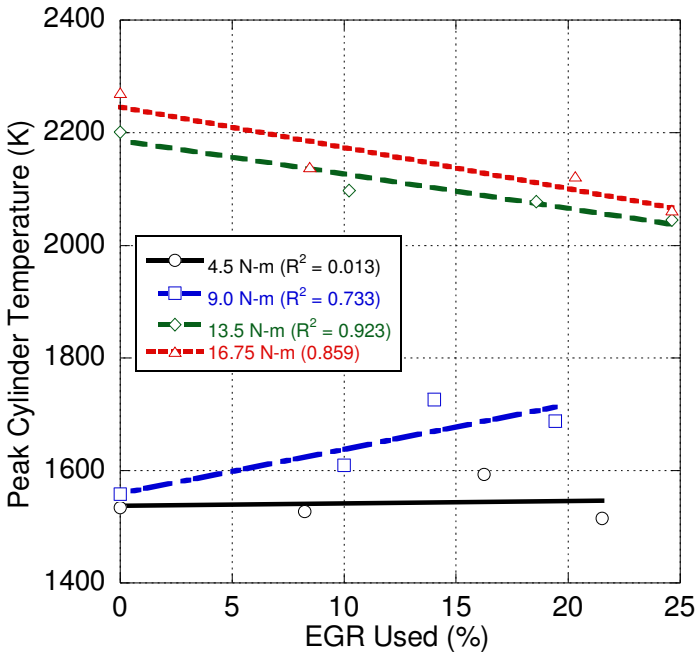

Figure 33. Comparison in the peak cylinder temperature for various percentages of EGR at each engine load. Tests run on a throttled engine without turbocharging.

The primary change in operating conditions as EGR was increased were increases in ignition delay (see Figure 32), most likely due to the diluting effects of EGR slowing the rate of combustion [159,

160]. At lower loads, peak RHR during the premixed spikes were nearly identical at all loads, with slightly higher peak RHR in some tests with EGR due to more fuel needed to sustain the engine load (and shown through the small rise in BSFC alongside the use of EGR). In addition, a slight degradation in thermal and fuel conversion efficiencies were found as expected. At a given percentage of EGR, the timing of ignition tended to decrease slightly as engine load was increase (see Figure 32), analogous to the trends without EGR in Figure 18.

At high engine loads, peak cylinder temperature decreased as more EGR was used resulting in a later and slower combustion process (see Figure 33). This was mirrored by a drop in measured nitrogen oxide emissions with increasing EGR (the primary reason for employing EGR). However, at low engine loads, the peak cylinder temperature tended to increase as more EGR was added. This is likely due to a change in experimental conditions in the original data collection, as the throttling of the engine had to be adjusted between the higher and lower load experiments due to a weld failure (explained in [10]). Therefore, the cylinder temperature results are presented here for completeness in description of the HR model; however, the data will need to be retaken. The literature documents that the higher load EGR trends with ignition delay and cylinder temperature are correct [161]. The HR model results, therefore, help indicate issues that arise during experimentation, ensuring that accurate and consistent data is collected.

3.5 Conclusions

The HR program presented offers a valuable addition to CI engine testing, allowing for a variety of differing testing procedures. The 0-D, three-zone equilibrium model allows for the calculation of heat release from the conservation of mass and energy through the engine cycle. The program uses an established Arrhenius-based model to predict the rate of combustion of fuel, removing the need for the user to establish the duration of the combustion event. In addition, the model is calibrated to the engine cycle's cumulative mass fraction burned, calculated experimentally from the engine emissions, adding to model stability in the transfer of mass and energy between the three zones of the control volume.

The model provides for the prediction of numerous gross engine output specifications, calculating output power and torque, thermal losses, and values which can be used to measure the efficiency of the engine cycle. Established ignition delays and methods for computing the end of combustion are also given for comparison and later use. Most importantly, the program allows for significant variations in fuel choice and operating conditions. Comparisons are made within the program to the pressure-reading program through various output characteristics (such as thermal and fuel conversion efficiencies, as well as BSFC and IMEP) to ensure model fidelity.

While ignition delay correlations are not always able to predict the onset of combustion effectively, the predictions offered by a few authors are able to place ignition within a few degrees of the expected timing. In addition, the model is protected through the use of the 2^{nd} derivative of the pressure trace. The lack of accuracy in ignition delay during turbocharged conditions is particularly apparent, but is not unexpected as other authors have reported similar findings, due primarily to changes in mixture quality over the cycle, as well as added turbulence. This necessitates an ignition delay correlation that can operate in the conditions associated with engine turbocharging and supercharging.

The program successfully calculates the components of cumulative HR from the calculated combustion efficiency for the engine cycle, and consistently delivers values supported by both the pressure reading program, and those established within the literature. In addition, the model allows for variation in fuel choices (including mineral diesels, oxygenates, and other fuels), EGR, and some inlet conditions. When paired with an emissions analyzer, the HR program offers a way to categorize the amount of energy released by combustion, and allows for a complete analysis of output characteristics, emissions, efficiency, and energy from a DI-CI engine.

Chapter IV: Efficiency and Emissions Mapping for a Single-Cylinder, Direct Injected Compression Ignition Engine

Jonathan M. S. Mattson*[1], Michael Mangus[1], Christopher Depcik[1]

[1] University of Kansas, Department of Mechanical Engineering

* Corresponding author: jmsmattson@gmail.com

4.1 Abstract

A timing sweep to correlate the location of Maximum Brake Torque (MBT) was completed on a single-cylinder, direct injected compression ignition engine that was recently upgraded to a high-pressure rail injection system for better engine control. This sweep included emissions monitoring for carbon dioxide, carbon monoxide, particulate matter, hydrocarbons, and oxides of nitrogen. This emissions analysis provided for the calibration of a heat release model, as well as the opportunity to relate MBT timing to brake-specific emissions production. The result of this timing sweep was a relatively linear correlation between injection delay and peak pressure timing. In addition, a number of other MBT timing methodologies were tested indicating their applicability for immediate feedback upon engine testing. Emissions were either strongly correlated to MBT timing (with emissions being minimized in the vicinity of MBT), or were completely independent of MBT. In addition, the end of the MBT timing envelope was linked to increased fuel consumption, as well as a rise in aromatic hydrocarbon emissions. Ideal fuel economy with lowered NO_x and PM emissions can be achieved for timings just after MBT, but will lead to production of hydrocarbon emissions that present difficulties to catalysis.

4.2 Introduction

The optimization of engine performance has always been a central aspect of the study of internal combustion engines. Within direct injected (DI) compression ignition (CI) engines, the primary modes of performance control are through the adjustment of injection timing, the number of injections, and the quantity and flow rate of fuel. For a singular injection strategy, changing injection timing leads to a relatively predictable variation in the initiation of ignition since the ignition delay of a fuel will be

somewhat linear for a given engine design, fuel, and load [162-164]. Controlling timing is important in setting the location of the peak cylinder pressure, which is known to be of great importance to engine performance due to the interrelationships between pressure and the other thermodynamic variables that control the conversion of energy into useful work. Within spark-ignition (SI) engines, the timing of spark ignition is set to a condition known as Maximum Brake Torque (MBT), where the engine is producing the maximum amount of work for a given input of fuel. For SI engines, this state has been empirically shown to occur when peak pressure exists at around 15 degrees of crank angle after top dead center (ATDC) [165, 166]. In SI engines, MBT is usually linked directly to spark timing [3]. Within CI engines, a similar condition exists that typically occurs at an earlier peak pressure timing, and varies widely as a function of ignition delay, engine and injector design, and injection pressure [164, 167-169]. Since the direct method of control by the researcher (e.g., the injection timing) is not explicitly linked to MBT due to changes in ignition delay, MBT timing itself is variable. Therefore, MBT timings for CI engines are often based on milestones in the pressure trace that occur after ignition (such as peak pressure, peak RHR, or CA50 that are discussed later in this section) [167].

In the immediate vicinity of MBT timing (in either direction), engine operation will show a slight decrease in efficiency, creating a "timing envelope" around the MBT state. Before this envelope (aka advanced injection), engine efficiency decreases because the engine is not effectively transferring the rise in pressure into output work. Hence, advanced timings tend to exhibit higher brake-specific fuel consumption (BSFC) [3]. After the envelope (aka delayed injection), experiments demonstrate a rapid drop in engine performance, whereby the cylinder volume is expanding too rapidly for combustion to build up suitable pressure [3]. This also results in an increase in BSFC, as the engine struggles to meet the desired power output [167].

Two primary methods exist for the correlation of MBT timing. The first is through the association of MBT with certain points of the pressure trace, most notably the timing of peak pressure [165, 169]. Alternatively, the peak value of the 1st derivative of the pressure trace (representing the point of highest

rate of change in the pressure) may be used [165, 167, 170]. In these methods, the in-cylinder Rate of Heat Release (RHR) does not need to be calculated [3].

The output power and injection timing can also be linked to the RHR or cumulative heat release (HR) of a CI engine (see Figure 34) [169]. Through the RHR, the timing of different phases of combustion can be determined. Additionally, the magnitude of these combustion phases (particularly the premixed spike) can be used to diagnose the efficacy of combustion. As a result, models used to calculate the RHR from an IC engine are important tools in any laboratory setting. These models vary widely in scope and detail, but most make use of an in-cylinder pressure trace captured through testing. The use of RHR for MBT timing is typically centered on the crank angle at which point 50% of the available fuel mass has been consumed by combustion, and often represented as CA50 [165, 170]. Alternative percentages of consumed fuel have also been used (particularly CA45 for 45% of fuel mass consumed) [167]. The calculation of mass fraction burned is closely tied with the calculation of engine HR, and so portions of certain RHR models can be used for MBT optimization [170].

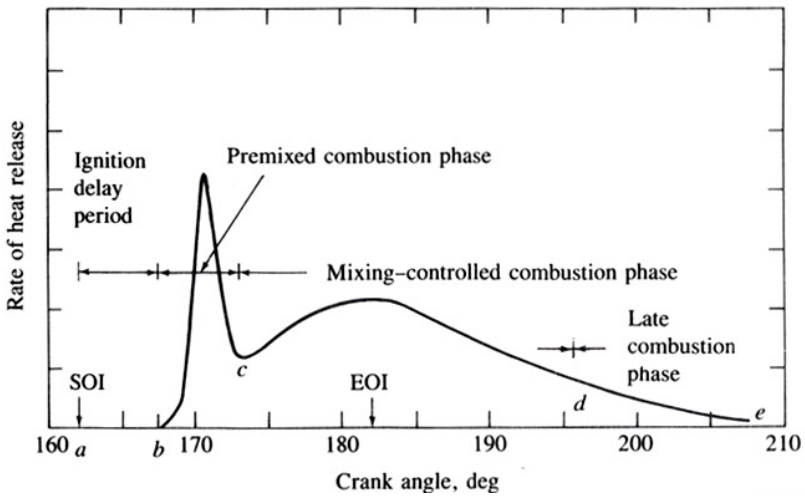

Figure 34. Example of Rate of Heat Release and combustion phases found in a compression ignition engine, from Heywood [3].

Mass fraction burned has also been estimated directly from the pressure trace, starting with the Rassweiler-Withrow model for SI engines [92]. A similar method developed by Zhu et al. calculates the

net pressure change within the cylinder, and is applicable to both SI and CI engines in correlation of MBT timing [165]:

Change in Net Pressure	$\Delta p_i = \left\{ p_{i+1} - p_i \cdot \left[\frac{\forall_i}{\forall_{i+1}} \right]^{1.3} \right\} \cdot \left[\frac{\forall_i}{\forall_{ig}} \right]$	(151)

where p and $\forall$ are the pressure and volume within the cylinder, i corresponds to the current crank angle, and $\forall_{ig}$ corresponds to the volume at ignition. The net pressure (p_{net}) is then given by the following:

Cumulative Net Pressure	$p_{net,i} = p_{net,i-1} + \Delta p_i$	(152)

Using Equation 152, MBT timing is found by using the net pressure as a surrogate for mass fraction burned, after it is first normalized to the combustion efficiency of the engine cycle [165].

Other researchers have associated MBT timing with the net apparent HR [3, 93, 167]. These models are a notable alternative to cumulative HR models, and often calculate the RHR from the change in the ratio of specific heats, or directly from the pressure trace (as is the case with the Rassweiler-Withrow model) [87, 92]. These models do not take heat transfer into account, which is normally calibrated to the model after the net changes in work and internal energy have been found. While this calibration is necessary in order to ascertain the total RHR of an engine, it also has the opportunity to introduce uncertainty in the mass fraction burned analysis. In using the net apparent HR for correlation with MBT timing, fewer computational resources are used, and the model also avoids the uncertainties associated with calibrating heat transfer coefficients, potentially providing a more reliable basis for linear MBT timing correlation [92, 167, 171]. Because heat transfer is neglected, the moment where 50% of cumulative HR is achieved does not align to the calculated CA50 timing given by the net apparent HR model. However, this shift does not appear to affect the empirical validity of the method [167].

Regardless of how an MBT correlation is found, the application is the same; when the engine is found to be operating at MBT (usually found through maximum torque or minimum BSFC, depending on methodology), the crank angle at which an MBT correlation is achieved can then be used later to set injection timing such that MBT is assured. For example, if using a CA50 correlation, the researcher firsts

performs an injection sweep in order to find the MBT state at a given engine load, and the crank angle at which CA50 occurs for MBT. When calibrating the engine later, the researcher then adjusts the injection timing to ensure that CA50 occurs at the correct crank angle for a given load to bring about MBT, replicating the conditions of the earlier injection sweep. Also, if the MBT timings for multiple loads are known, MBT at an intermediate load can be calibrated by interpolating between two known MBT timings. The appropriate choice of correlation is then dependent on what can be measured during operation: if the mass fraction burned profile is not known during engine operation, then a CA50 correlation will be of no use for calibration of MBT timing. The correlations as functions of engine load typically exhibit linear behavior, and so the correlation with the least deviation from linearity is considered most useful. In addition to maximizing the work potential of the engine through MBT timing, investigating injection and peak pressure timing is useful in understanding engine emissions production. Emissions are related to the completeness of combustion, as well as the peak temperature within the cylinder that is related to the pressure through the ideal gas law. With knowledge of the emissions for a given injection timing, as well as the brake specific output of the engine, it is possible to adjust and control emissions during normal engine operation without significantly sacrificing output power [3, 169].

To this end, an empirical study was accomplished in order to diagnose the relationship between peak pressure and a singular fuel injection strategy for a single-cylinder DI-CI engine. This analysis was done utilizing systems that capture the in-cylinder pressure trace and exhaust engine emissions, as well as the previously described HR model. With respect to engine optimization, the timing of peak pressure for a given loading was chosen as the primary means to which MBT timing could be correlated since it was readily available in the experimental setup. The peak pressure-indicated MBT timing was then compared to other important cycle timings, in an effort to produce an ideal method that correlates MBT operation with a single injection timing strategy for a DI-CI engine. This testing showed that the HR-indicated CA50 MBT timing methodology offers a promising means to correlate MBT timing. In addition, the MBT timings associated with net HR and peak pressure location are the most useful, given their established accuracy and linear behavior. Brake specific emissions of many species tend to be minimized

at (or immediately after) MBT timing, particularly for emissions of partially oxidized species such as hydrocarbons (HC) and carbon monoxide (CO). Additionally, the end of the MBT timing "envelope" may be marked by a sudden rise in the fraction of aromatic HC species composing the brake-specific total hydrocarbon (THC) emissions.

4.3 Experimental Setup

For a complete fuel sweep, the authors used an expanded procedure, based on methods used in previous engine testing [10, 11]. This procedure allows for a complete analysis of an engine's performance, including the measurement of emissions and the calculation of the cumulative HR. In addition, the procedure builds upon itself, and each subsystem provides engine specifications that overlap with the other systems, offering additional surety in the quality of the procedure's results.

The engine chosen for the mapping is a Yanmar L100v single-cylinder DI-CI engine [10, 11]. The current engine has been modified significantly, in order to increase the number of testing modes available (see Table 15) and to interface with other supplementary systems for emissions analysis [10]. The primary changes to the engine itself include a blocking of the internal passage used for Exhaust Gas Recirculation (EGR), in order to facilitate external EGR experimentation. Additionally, the original in-line fuel injection system (mechanical unit injector) has been replaced with a high-pressure rail injection system, controlled by a Bosch MS15.1 engine control unit (ECU) that provides variable and multiple injection timings,, duration, and flow rate. The engine was operated unthrottled and without added aftertreatment.

Table 15. Yanmar Engine Specifications.

Manufacturer and Model	Yanmar L100V
Type	Vertical Direct-Injection Compression Ignition
Engine Intake	Naturally Aspirated
Cooling	Air-Cooled
Cycle	4-Stroke
Displacement [cc]	435
Number of Cylinders	1
Number of Valves	1 Intake, 1 Exhaust
Bore [mm]	86
Stroke [mm]	75
Connecting Rod length [mm]	118
Crank Radius [mm]	38
Clearance Volume [m^3]	2.1611×10^{-5}
Cylinder Head/Piston Area [m^2]	0.0058088
Compression Ratio	21.2
Injection Timing	Variable
Continuous Rated Output [hp]	8.3 SAE
Continuous Rated Output [kW]	6.2
Rated Speed [RPM]	3600
Injector Pressure	Variable, Limited to 200 MPa
Engine Oil Used	Shell 15W-40

Engine loading is applied and monitored through a Dymond Series 12 horsepower AC dynamometer, supplied by DyneSystems, Inc, with operational information displayed in Table 16. Engine torque is measured using a FUTEK rotary transducer (model #TRS-605) mounted between the engine and dynamometer. Additional instrumentation is achieved through multiple thermocouples and pressure transducers in order to measure ambient, intake, and exhaust temperatures and pressures. In-cylinder pressure is measured through a Kistler 6052C pressure transducer (measured at 43.2 kHz), and a Kistler 2614B encoder is used to determine the corresponding crank angle. Inlet air mass flow is measured using a Merriam laminar flow element (model #50MW20-2), and an Omega differential pressure transducer (model #PX277-30D5V). Fuel flow rate is determined through a Micro-Motion Coriolis flow meter (model #CMF010M) [11].

Table 16. Dynamometer Specifications.

Manufacturer and Model	DyneSystems,Inc. Dymond Series 12
Continuous Torque [ft-lbs]	21.1
Continuous Power [hp]	12
Speed Range [RPM]	0-7500
Voltage [V]	480
Phase	Three Phase
Frequency [Hz]	60
Controller	DyneSystems,Inc. Inter-Loc V OCS

Measurement of engine operating characteristics was done through a National Instruments (NI) based system recording at a rate of 10 Hz for two minutes, and a separate NI system was used to capture the pressure trace. In order to negate errors caused by small cyclic variations in engine operation, 60 consecutive thermodynamic cycles are captured for the pressure trace, corresponding to 120 engine revolutions at a resolution of 0.5° of crank angle.

A third NI system is used for the characterization of engine emissions through an AVL SESAM Fourier Transform Infrared (FTIR) spectroscopy emissions analyzer. The unit functions by retrieving a sample of the engine emissions, which is then filtered for particulates to keep them from damaging the sensing equipment. At this point, the sample is diverted into three separate emissions analyzers. The first is a Flame Ionization Detector (FID), which measures total hydrocarbons (THC) within the emissions sample. The analyzer ionizes the remaining hydrocarbons in a hydrogen-air flame, and produces a current proportional to the concentration of carbon compounds within the sample. The second emissions reading technique is through the FTIR spectroscopy measurement. In this method, the unit takes advantage of the emission of light in the infrared spectrum by the gas molecules when excited by a laser, which will produce emission spectra unique to the composition of the exhaust gas. However, this measurement technique cannot take the emissions spectra of diatomic molecules into account. Because these molecules have a single bond, they vibrate in a linear fashion, and so it becomes impossible to accurately measure the spectrum of these molecules without knowing their orientation. Therefore, within the SESAM system, this leads to the third emissions measurement system: a Magnos 106 sensor for the measurement of diatomic oxygen.

Through these three subsystems, the emissions analyzer has the ability to measure THCs, CO and nitrogen oxides (NO_x), accounting for the most important classifications of diesel emission species. THC emissions can also be further split into subgroups in order to account for distinct families of emitted HCs; e.g., aldehydes, ketones, alkanes, partially oxidized fuel, and the related species of benzene, toluene, ethylbenzene, and xylene (known collectively as BTEX) [172]. Measurements are recorded at a frequency of 1 Hz over 5 minutes, concurrent to the recording of engine performance and in-cylinder data. Finally, Particulate Matter (PM) emissions are measured using an AVL 415S Variable Sampling Smoke Meter. In order to maintain accuracy across multiple engine operating conditions, the sampling duration was varied according to engine loading in order to maintain a filter blackening number of approximately four (as per AVL recommendations).

4.3.1 Heat Release

Engine HR is an essential component of any diagnostic testing. For this study, the zero-dimensional equilibrium model constructed previously was used for the calculation of MBT characteristics. The combustion efficiency used in the calibration of the HR model (Equation 50) is found using the AVL SESAM FTIR and Smoke Meter emission measurements, and is calibrated to the emission of hydrogen (H_2), carbon monoxide (CO), and THCs. The simulation then uses this calculation of combustion efficiency to iterate until reaching a convergence of combustion efficiency and cycle mass fraction burned, as discussed earlier.

4.3.2 Procedure

For the mapping, the authors chose to perform a fuel injection sweep of the engine at a single speed, with the goal of finding the appropriate timing of fuel injection for peak cylinder pressure [3, 165]. In addition, engine emissions were monitored across the injection sweep, in order to provide a trend of emissions with respect to injection timing and load. The engine was operated at 1800 revolutions per minute (RPM) for the sweep, with engine load adjusted from 0.5 N-m (when unloaded), to 18 N-m (the

maximum rated load at 1800 RPM) in increments of 25% of rated load (approximately 4.5 N-m). This culminated in five total fuel sweeps for the engine.

For an individual sweep, the injection timing was advanced in the engine cycle such that the peak pressure timing was no earlier than 6° ATDC, or the peak pressure itself was no higher than 65 bar. These bounds were set by the authors due to the anticipated timing of MBT (expected to be after 6° ATDC), and also out of concern over reliability at high pressures indicated from prior experience in using the engine [11]. At this first injection timing, the amount of fuel injected was adjusted in order to achieve one of the five desired output loads. After waiting for the engine to come to steady state (assumed to occur when the exhaust and oil temperatures changed by less than 1% in 60 seconds), the in-cylinder pressure, engine performance characteristics, engine emissions, and particulates were catalogued. At this point, the injection timing was moved closer to TDC in one-degree increments, with the fuel injection mass flow rate changed in order to hold the engine load constant. This resulted in engine combustion moving further into the expansion stroke. The engine was allowed to return to steady state, and the measurements were repeated. This process would continue until the engine experienced a large drop in performance upon delaying the injection timing. This decline was typically indicated by a large increase in fuel flow rate in order to meet the desired engine load, as the engine had left the MBT timing envelope.

After the emissions data was collected, the combustion efficiency was found using Equation 50, using H_2, CO, and THC measurements from the engine exhaust. This combustion efficiency, as well as the pressure trace, was then fed into the HR model for processing of gross engine characteristics, as well as the various characteristics used to correlate the MBT timing. Since engine loading was kept constant across the injection sweep, MBT timings were correlated to the peak pressure timing that brought about the minimum gross brake specific fuel consumption ($BSFC_g$) as indicated by the HR model that excludes the pumping work of the cycle. Alternatively, MBT timing could be found through the maximum fuel conversion efficiency (whereby the highest amount of fuel energy is being used for work), or the

minimum equivalence ratio (by finding where the engine has the highest ratio of air to fuel, and is related to $BSFC_g$), both of which were determined by the HR model.

Alternate MBT timings were calculated using the 1st derivative of the pressure trace and the CA50 measurement computed through the net pressure method (discussed earlier). Because of the requirement of a higher crank angle resolution in order to determine CA45, the measurement was neglected in favor of the more widely used CA50 metric. In addition, CA50 measurements were determined by the HR model using the indicated mass fraction burned, the cumulative HR with Woschni, Hohenburg, and averaged heat transfer coefficients, along with the net heat release excluding all heat transfer. These results were then compared to the peak pressure timings, with the goal of finding a linear correlation for MBT timing for the engine operating at 1800 RPM.

4.4 Results and Discussion

The pressure traces for each injection timing at a given load can be seen in Figure 35 (0.5 N-m), Figure 36 (4.5 N-m), Figure 37 (9.0 N-m), Figure 38 (13.5 N-m), and Figure 39 (18.0 N-m). Engine speed remained relatively constant at 1800±0.25 RPM for all tests, and injector pressure was held constant at 42±0.5 MPa.

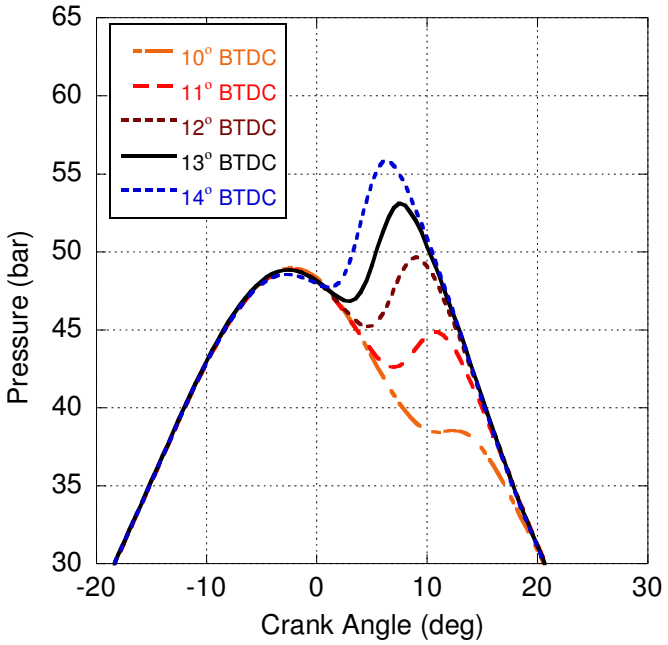

Figure 35. Pressure traces for varying injection timings at 0.5 N-m. Engine was operated unthrottled at 1800 RPM.

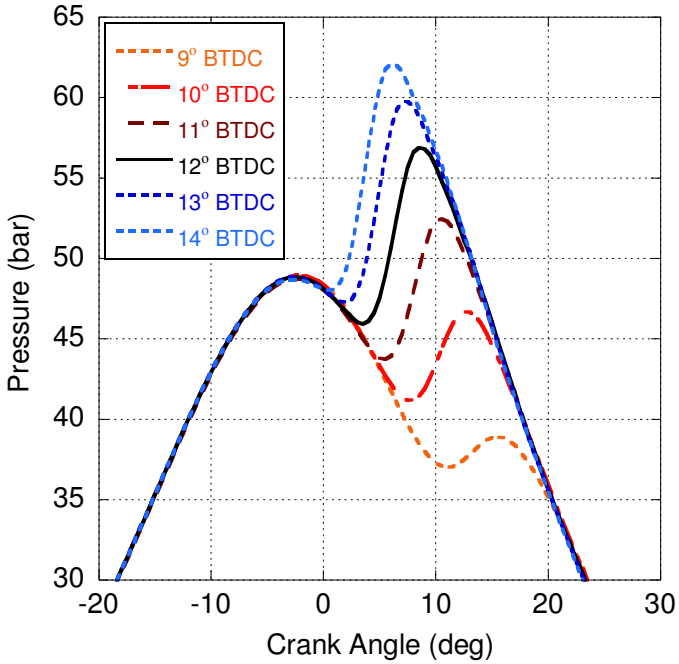

Figure 36. Pressure traces for varying injection timings at 4.5 N-m. Engine was operated unthrottled at 1800 RPM.

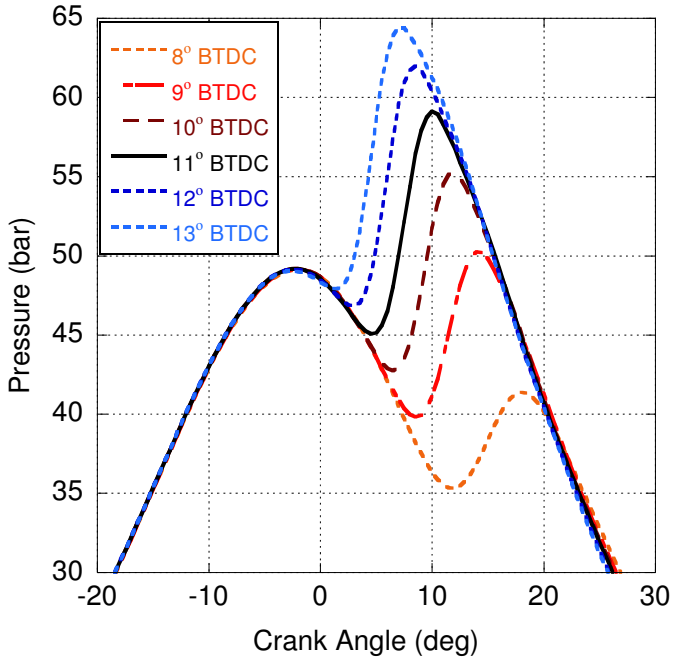

Figure 37. Pressure traces for varying injection timings at 9.0 N-m. Engine was operated unthrottled at 1800 RPM.

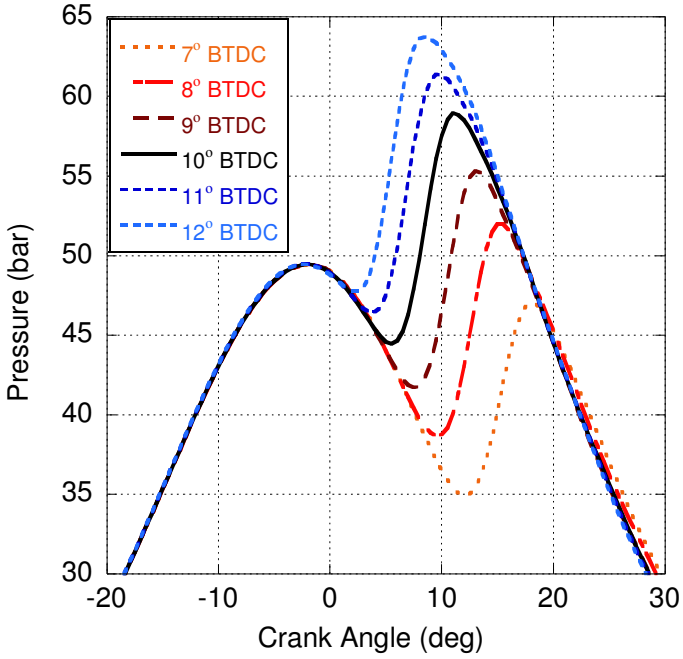

Figure 38. Pressure traces for varying injection timings at 13.5 N-m. Engine was operated unthrottled at 1800 RPM.

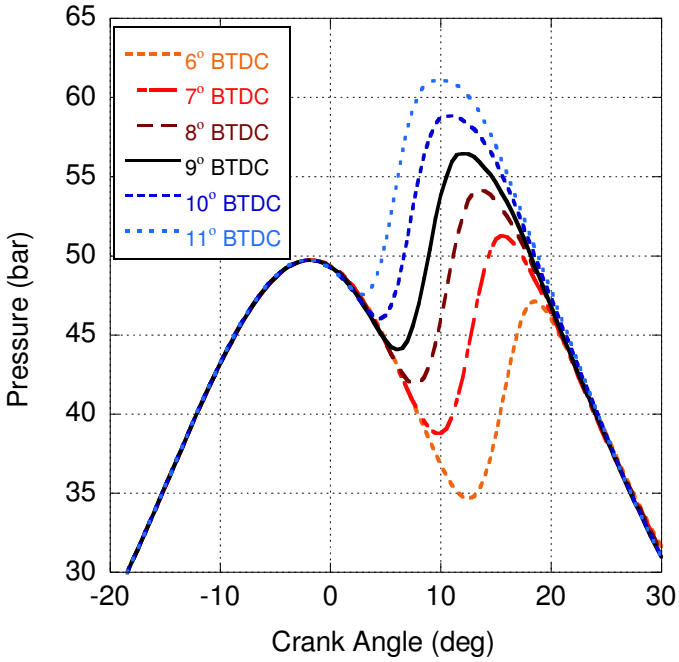

Figure 39. Pressure traces for varying injection timings at 18.0 N-m. Engine was operated unthrottled at 1800 RPM.

4.4.1 Performance and Rate of Heat Release

At 0.5 N-m, the thermal efficiency tended to increase as a function of peak pressure and ignition timing (see Table 17). Fuel conversion efficiency was at its maximum with injection between 13° and 12° BTDC (for a peak pressure location between 7.75° and 9.00° ATDC), and $BSFC_g$ and equivalence ratio were at their minimum within the same range, all indicating a more efficient use of fuel for this range of injection timings. Combustion efficiency trended downward as injection timing was delayed, indicating a loss in mass fraction burned for combustion further from TDC, and $IMEP_g$ trended upwards with later injection timings. Injection timing and peak cylinder temperature were directly correlated, due the increasing volume (and decreased availability) of the bulk gas as ignition delayed further and further after TDC. Exhaust temperatures for delayed combustion, reflecting a more prolonged premixed spike. These trends held for peak pressures less than 12.50° ATDC, at which point the engine was found to have exited the MBT envelope; i.e., thermal efficiency, fuel conversion efficiency, and $IMEP_g$ fell significantly, whereas $BSFC_g$ and equivalence ratio both rose significantly. The MBT timing of the peak pressure was

found to occur at approximately 8.5° ATDC, corresponding to the peak fuel conversion efficiency, as well as the minimum $BSFC_g$ and equivalence ratio. It is interesting to see that the non-linearity of engine combustion is readily evident with maximum thermal, fuel conversion, and combustion efficiencies all occurring at different injection timings. This illustrates the challenge of the engine calibrator as it indicates the balance between work output and emissions due to dissociation and partial combustion including the influence of chemical species on the ratio of specific heats during the expansion process.

Table 17. Gross engine output characteristics at 0.5 N-m of load for varying injection timings.

Injection Timing [° BTDC]	10	11	12	13	14
Ignition Timing [° ATDC]	5.5	4.0	2.5	1.5	0.0
Peak Pressure Timing [° ATDC]	12.50	10.75	9.00	7.75	6.25
Thermal Efficiency [%]	18.05	**18.68**	18.33	17.96	17.17
Fuel Conversion Efficiency [%]	14.36	16.08	16.48	**16.49**	15.91
Combustion Efficiency [%]	79.55	86.06	89.90	91.79	**92.65**
$IMEP_g$ [bar]	0.748	**0.767**	0.756	0.754	0.740
$BSFC_g$ [g kW^{-1} hr^{-1}]	583.2	520.7	508.0	**507.7**	526.3
Equivalence Ratio	0.183	0.167	0.161	0.160	0.164
Peak Cylinder Temperature [K]	928.7	978.0	1003.2	1030.4	1050.3
Exhaust Temperature [K]	387.7	383.7	381.2	380.5	381.2

When seen on an absolute scale, the peak RHR during the premixed phase of combustion decreased as injection timing was delayed (see Figure 40). In addition, the premixed spike seemed to increase in duration and blend with the diffusion burn portion of the cycle. This was likely due to the high rate of fuel flow into the cylinder by injection under lower temperatures promoting a longer ignition delay, allowing for much of the fuel to be injected and prepared in time for the premixed spike, while leaving less unburned fuel for the diffusion burn. Moreover, the high rate of expansion of the cylinder for crank angles further from TDC served to remove oscillations from the pressure trace, resulting in a smoother RHR for later injection timings. This is apparent at the most delayed injection timing (10° BTDC), where the premixed and diffusion portions of the combustion cycle have no discernible boundary between them.

For further analysis, the RHR was normalized by dividing the RHR at each crank angle by the cumulative HR of the engine cycle (see Figure 41), removing differences in RHR caused by increased fuel mass (or energy content). After this normalization, the optimum RHR was achieved with an injection

timing of 13° BTDC, corresponding with a peak pressure timing of 7.75, and therefore the MBT timing. At this injection timing, the peak in RHR occurred 6° ATDC (1.75° before the peak pressure location), at an absolute rate of 33.85 J/deg, or a normalized rate of 18% HR/deg (or 18% of the cumulative heat release per degree of crank angle).

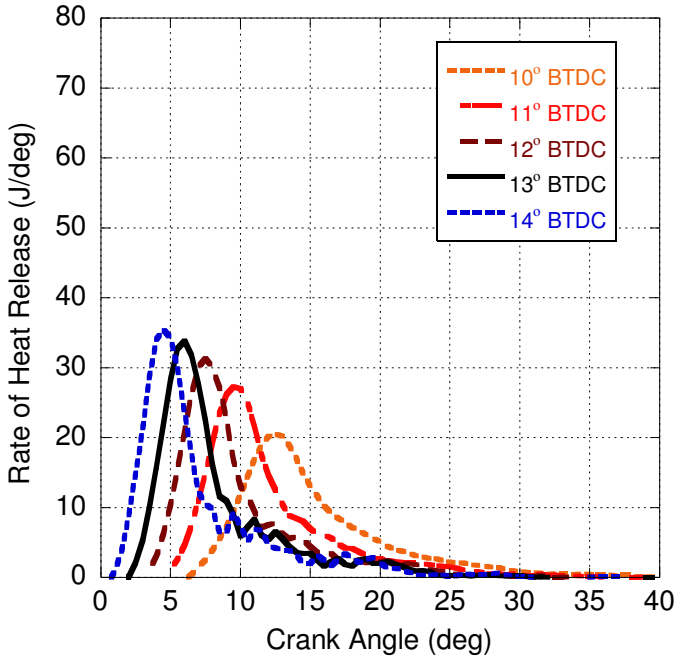

Figure 40. Rate of Heat Release for engine operating at 1800 RPM for 0.5 N-m of load, with varying injection timings.

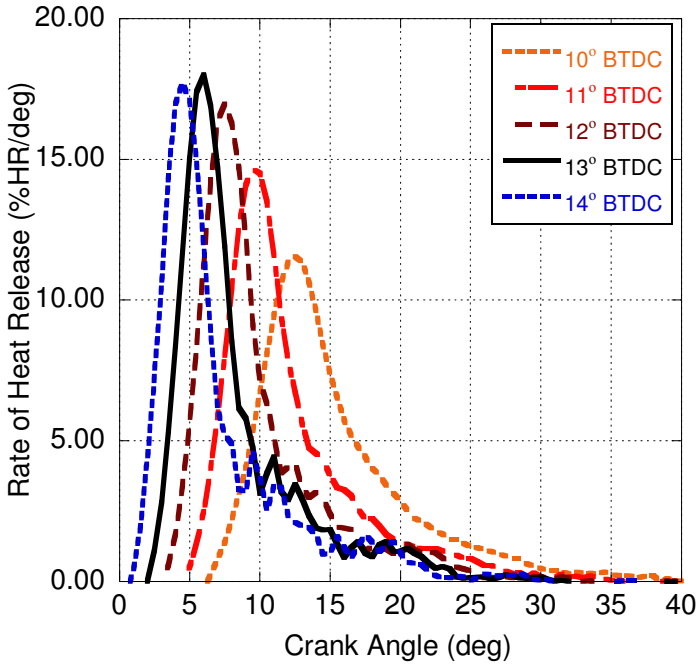

Figure 41. Normalized Rate of Heat Release for engine operating at 1800 RPM for 0.5 N-m of load, with varying injection timings.

The trends at 0.5 N-m were extended to 4.5 N-m. Later ignition timings (from delayed injection) were met with increases in thermal efficiency and decreased combustion efficiency (see Table 18). Fuel conversion efficiency was maximized corresponding to fuel injection at 12° BTDC (with peak pressure at 8.50° ATDC), and equivalence ratio and $BSFC_g$ experienced their minimum values at this timing. $IMEP_g$ increased along with peak pressure timing, and peak cylinder temperature again fell as combustion fell further delayed from TDC, while exhaust temperatures increased as combustion was more prolonged. The losses in efficiency and operating characteristics as the peak pressure timing exited the MBT timing envelope were less significant than in the tests with 0.5 N-m. MBT timing was correlated to a peak pressure timing of 9.0° ATDC.

Table 18. Gross engine output characteristics at 4.5 N-m of load for varying injection timings.

Injection Timing [° BTDC]	9	10	11	12	13	14
Ignition Timing [° ATDC]	6.5	5.0	3.5	2.0	0.5	-0.5
Peak Pressure Timing [° ATDC]	15.50	12.75	10.50	8.50	7.25	6.00
Thermal Efficiency [%]	**27.88**	27.49	26.92	26.75	26.17	25.60
Fuel Conversion Efficiency [%]	24.52	25.55	25.65	**25.83**	25.42	24.93
Combustion Efficiency [%]	87.95	92.92	95.31	96.57	97.12	**97.39**
$IMEP_g$ [bar]	**1.760**	1.709	1.688	1.687	1.660	1.650
$BSFC_g$ [g kW^{-1} hr^{-1}]	341.5	327.7	326.4	**324.2**	329.4	335.8
Equivalence Ratio	0.254	0.238	0.235	0.234	0.234	0.237
Peak Cylinder Temperature [K]	1040.0	1098.2	1120.7	1157.4	1154.3	1169.4
Exhaust Temperature [K]	437.9	428.0	424.6	422.6	421.0	419.1

Like the engine output trends, the qualitative differences between RHR at the 0.5 and 4.5 N-m loads were quite small. However, the changes in absolute RHR for the earliest three injection timings (14°, 13°, and 12° BTDC) were much smaller (see Figure 42 and Figure 43). At these injection timings, the diffusion burn amounts were nearly identical. At later injection timings (11° BTDC and beyond), the premixed and diffusion burn phased merged with no boundary apparent for fuel injection at 9° BTDC. Optimum RHR occurred for an injection timing of 12° BTDC in agreement with MBT timing (peak pressure timing 7.25° ATDC), for a RHR of 49.43 J/deg (17.58% HR/deg) at 5° ATDC that is 2.25° before the peak pressure location.

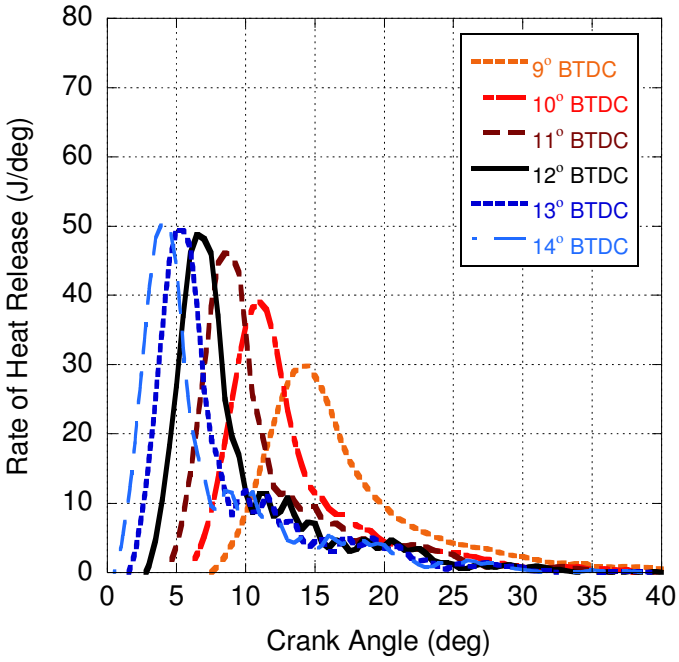

Figure 42. Rate of Heat Release for engine operating at 1800 RPM for 4.5 N-m of load, with varying injection timings.

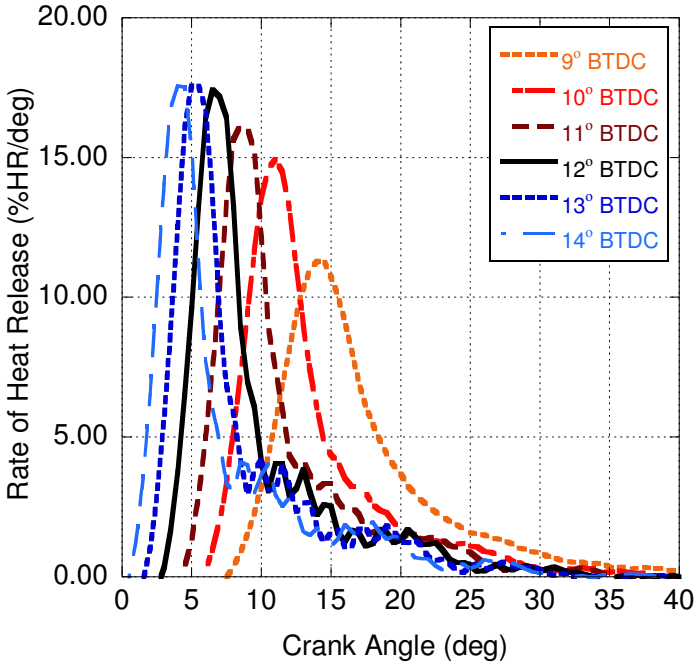

Figure 43. Normalized Rate of Heat Release for engine operating at 1800 RPM for 4.5 N-m of load, with varying injection timings.

For the 9.0 N-m engine load sweep, delaying injection resulted in steady increases in $IMEP_g$, and exhaust temperature as well as a general decrease in peak cylinder temperature and combustion efficiency

(see Table 19). Thermal efficiency rose before holding steady (with a very slight decrease) as injection timing was delayed past 11° BTDC. Fuel conversion efficiency followed a similar trend, although with a more noticeable decrease for injection timings delayed after 11° BTDC. $BSFC_g$ was at its minimum for this injection timing as well, for an MBT timing of peak pressure at approximately 10° ATDC. Minimum equivalence ratio occurred for injection slightly advanced from MBT; however, the equivalence ratio only differs by 0.001 in comparison to MBT timing. The MBT envelope was found to end for peak pressure timings between 14° and 18° ATDC (with injection timings between 9° and 8° BTDC, respectively).

Table 19. Gross engine output characteristics at 9.0 N-m of load for varying injection timings.

Injection Timing [° BTDC]	8	9	10	11	12	13
Ignition Timing [° ATDC]	7.5	6.0	4.5	3.0	1.5	0.5
Peak Pressure Timing [° ATDC]	18.00	14.00	12.00	10.00	8.50	7.25
Thermal Efficiency [%]	**32.42**	32.11	32.13	32.14	31.56	30.64
Fuel Conversion Efficiency [%]	30.90	31.34	31.59	**31.70**	31.15	30.29
Combustion Efficiency [%]	95.30	97.59	98.32	98.63	98.72	**98.84**
$IMEP_g$ [bar]	**2.902**	2.867	2.853	2.841	2.782	2.748
$BSFC_g$ [g kW^{-1} hr^{-1}]	271.0	267.1	265.0	**264.1**	268.7	276.4
Equivalence Ratio	0.339	0.331	0.327	0.325	0.324	0.328
Peak Cylinder Temperature [K]	1235.3	1246.8	1259.2	1277.8	1274.5	1285.6
Exhaust Temperature [K]	496.9	484.6	478.8	475.6	472.7	469.1

The premixed spikes for the four earliest injection timings (13° to 10° BTDC) were virtually identical (other than the crank angle offset due to injection timing), at an average peak RHR of 62.8±0.5 J/deg (see Figure 44). As injection timing was delayed in one degree increments for the first four timings, ignition delay tended to increase by 0.5-1.0° of crank angle, and peak RHR preceded peak pressure by an average of approximately 2°. When normalized for fuel mass and energy content, peak RHR was achieved with injection at 10° BTDC (slightly delayed versus MBT timing, see Figure 45) at 63.00 J/deg (16.50% HR/deg), and occurred at 10° ATDC. The peak RHR under MBT conditions (injection at 11° BTDC) achieved a higher absolute RHR at 63.37 J/deg, but a lower normalized RHR at 16.38% HR/deg, indicating a slightly more prominent diffusion burn.

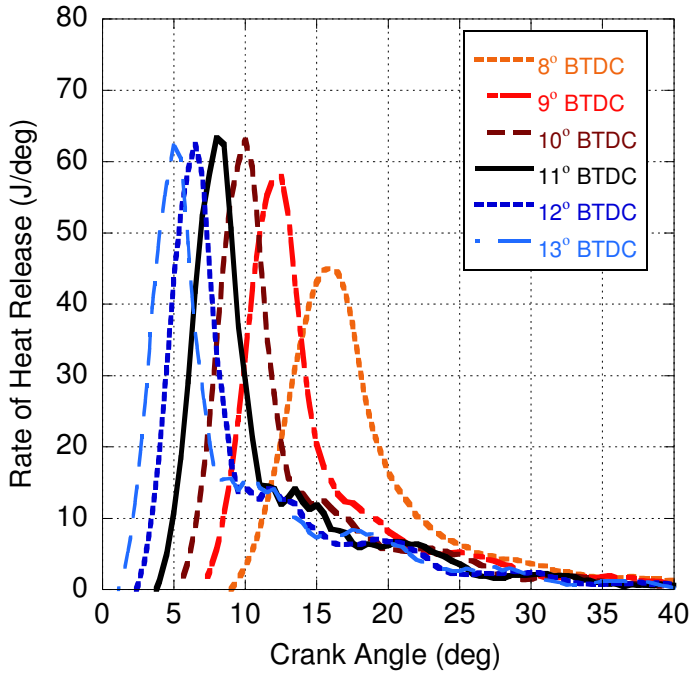

Figure 44. Rate of Heat Release for engine operating at 1800 RPM for 9.0 N-m of load, with varying injection timings.

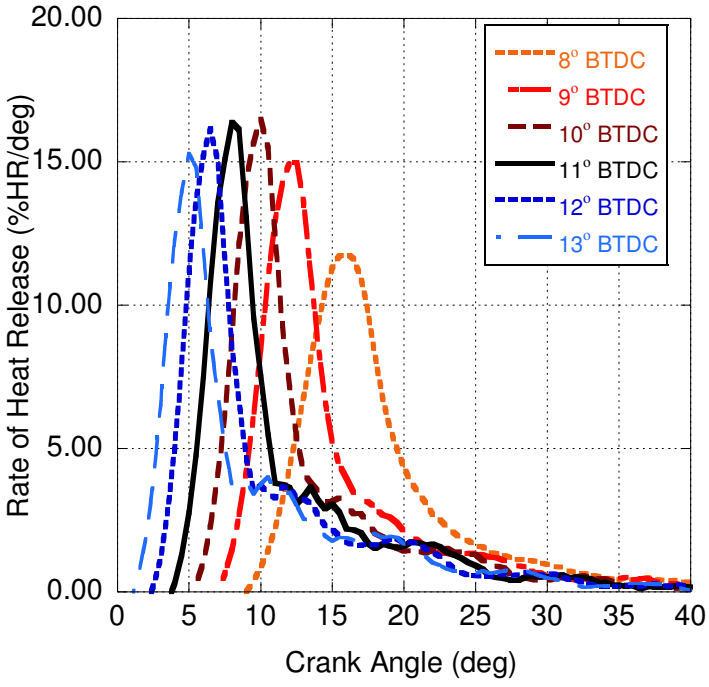

Figure 45. Normalized Rate of Heat Release for engine operating at 1800 RPM for 9.0 N-m of load, with varying injection timings.

The engine experienced some deviation from the prior trends in tests at 13.5 N-m of engine load (see Table 20). Peak cylinder temperature trended upwards as fuel injection timing was delayed, due to

the increasing amounts of fuel being injected into the cylinder in order to meet engine load, and exhaust temperature rose over the same range. At this point, it is believed that the injector was adding a significant amount of fuel to the cylinder after the onset of combustion that was not consumed in the premixed spike. This can be seen in Figure 46 and Figure 47 through the decrease in initial magnitude of the diffusion burn in the RHR as injection is delayed, ignition delay is prolonged, and the engine has slightly more time to add fuel that can be consumed in the premixed spike. $BSFC_g$ and equivalence ratio were both minimized at an injection timing of 10° BTDC, and both thermal and fuel conversion efficiency were maximized, leading to an estimated MBT timing of 10.25° ATDC. However, thermal and fuel conversion efficiency both showed high values for delayed injection, as well as a relatively low $BSFC_g$.

Table 20. Gross engine output characteristics at 13.5 N-m of load for varying injection timings.

Injection Timing [° BTDC]	7	8	9	10	11	12
Ignition Timing [° ATDC]	8.0	6.5	5.0	3.5	2.0	1.0
Peak Pressure Timing [° ATDC]	18.00	15.25	13.25	11.25	9.75	8.50
Thermal Efficiency [%]	33.97	**34.01**	33.29	**34.01**	33.67	33.29
Fuel Conversion Efficiency [%]	33.52	33.69	33.02	**33.78**	33.46	33.04
Combustion Efficiency [%]	98.67	99.03	99.18	99.32	**99.37**	99.27
$IMEP_g$ [bar]	**4.143**	4.084	3.903	3.984	3.957	3.898
$BSFC_g$ [g kW^{-1} hr^{-1}]	249.8	248.5	253.6	**247.8**	250.2	253.4
Equivalence Ratio	0.469	0.460	0.450	0.448	0.450	0.449
Peak Cylinder Temperature [K]	1453.4	1436.4	1408.8	1404.0	1422.4	1407.2
Exhaust Temperature [K]	566.6	554.5	546.0	542.8	539.6	533.6

The relatively high efficiency for delayed combustion can be attributed to a number of beneficial phenomena related to air mixing at higher loads. Delaying the injection timing leads to a longer ignition delay (13° to 15°) and an increased amount of time from ignition to the peak pressure (7.5° to 10°). Combined, this results in more mixing time available (air with fuel), subsequently promoting a more homogeneous mixture before combustion. This enhanced mixing helps offset the negative effects inherent in operating at delayed injection timings. This increasing efficiency is also indicated in the RHR for the engine as a function of injection timing (see Figure 46 and Figure 47). Unlike the previous loads, both absolute and normalized RHR trended downwards as injection timing was advanced, highlighting the stunting of premixed combustion caused by relatively lower air/fuel mixing levels. RHR peaked for

injection timings as late as 8° BTDC at 75.62 J/deg (14.36% HR/deg), corresponding to a peak RHR at 13° ATDC, and preceding peak pressure by 2.25° of crank angle. MBT timing experienced a peak RHR at 9° ATDC (preceding peak pressure by 1.25°), at 68.91 J/deg (12.98% HR/deg).

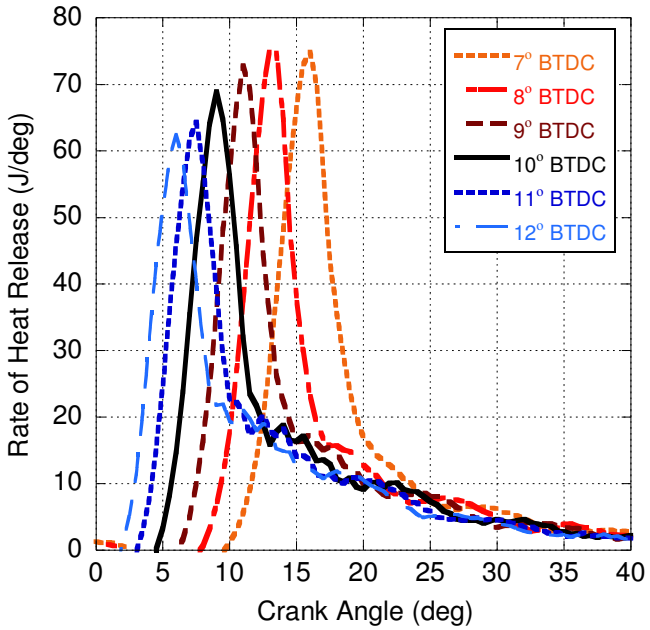

Figure 46. Rate of Heat Release for engine operating at 1800 RPM for 13.5 N-m of load, with varying injection timings.

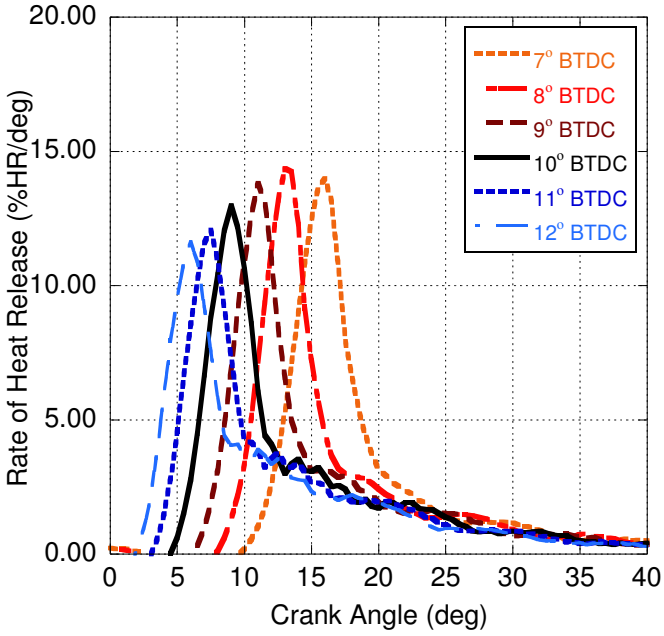

Figure 47. Normalized Rate of Heat Release for engine operating at 1800 RPM for 13.5 N-m of load, with varying injection timings.

The air-limiting phenomena and prolonged fuel injection present at 13.5 N-m were fully displayed at 18.0 N-m of engine load. All three efficiency values trended downwards as injection was delayed, although combustion efficiency remained well above 99% for all timings (see Table 21). $BSFC_g$ and equivalence ratio were both minimized at the earliest injection timing, and increased as combustion was allowed to take place later in the cycle. Peak cylinder temperature showed large variances and trended downwards as injection was delayed. $IMEP_g$ demonstrated similar variances to temperature, but generally trended upwards with increased delay. MBT timing occurred at the injection timing of 11° BTDC, corresponding to a peak pressure at 10° ATDC. More efficient engine operation could be possible for more advanced injection timings, but the authors' concerns over engine hardware (specifically due to limitations in peak pressure) prevented testing in the region that would result in peak pressures closer to TDC. Exhaust temperatures rose as injection was delayed further, as combustion became increasingly prolonged and complete, in addition to the additional fuel needed to keep the engine at load.

Table 21. Gross engine output characteristics at 18.0 N-m of load for varying injection timings.

Injection Timing [° BTDC]	6	7	8	9	10	11
Ignition Timing [° ATDC]	8.5	7.0	5.5	4.0	3.0	1.5
Peak Pressure Timing [°	18.50	15.50	13.50	12.25	11.00	10.00
Thermal Efficiency [%]	32.29	33.32	33.53	33.41	33.86	**33.93**
Fuel Conversion Efficiency [%]	32.06	33.13	33.34	33.24	33.70	**33.79**
Combustion Efficiency [%]	99.28	99.41	99.43	99.47	99.54	**99.58**
$IMEP_g$ [bar]	5.187	5.175	**5.195**	5.087	5.123	5.098
$BSFC_g$ [g kW^{-1} hr^{-1}]	261.2	252.7	251.1	251.9	248.4	**247.8**
Equivalence Ratio	0.627	0.609	0.610	0.600	0.600	0.595
Peak Cylinder Temperature [K]	1506.1	1521.4	1514.0	1534.0	1526.7	1556.3
Exhaust Temperature [K]	657.7	642.9	635.4	626.5	618.8	612.5

The peak value of both absolute and normalized RHR increased linearly with injection delay (see Figure 48 and Figure 49). Peak RHR existed for injection at 6° BTDC, occurring at 16° ATDC (preceding peak pressure by 2.5°) at 79.27 J/deg (11.15% HR/deg). Air-limiting combustion is seen in the relatively low percentage of RHR from premixed combustion, which increases with delayed injection due to augmented mixing effects. Note that between Figure 41 and Figure 49, the relative fraction of the heat

release due to the premixed spike is readily evident. As more fuel enters the cylinder in order to increase the engine load, it comes in the form of diffusion burn that occurs later in the engine cycle. The relative level of diffusion burn could be adjusted by increasing the fuel injection pressure, increasing the fuel flow rate dramatically (injector pressure during testing was held constant at 42 MPa, but could be adjusted to as much as 200 MPa). The peak RHR for MBT timing was located at 6.5° ATDC (3.5° before peak pressure timing), at 56.83 J/deg (8.22%HR/deg).

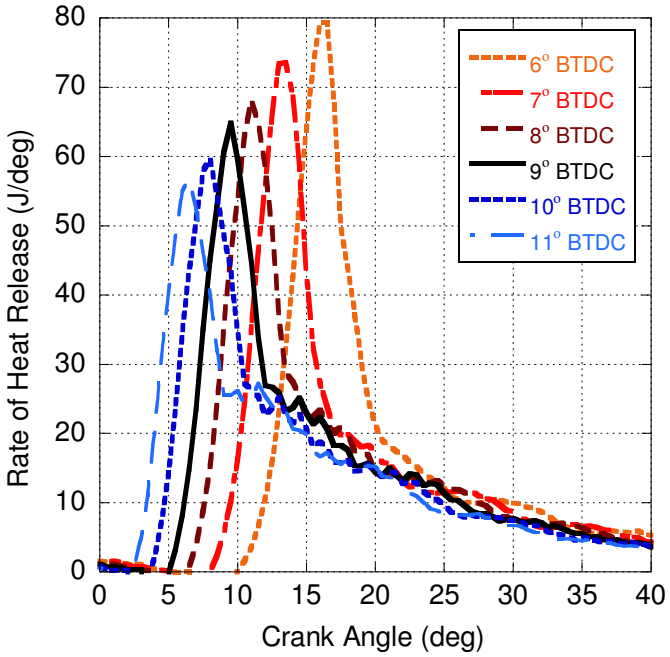

Figure 48. Rate of Heat Release for engine operating at 1800 RPM for 18.0 N-m of load, with varying injection timings.

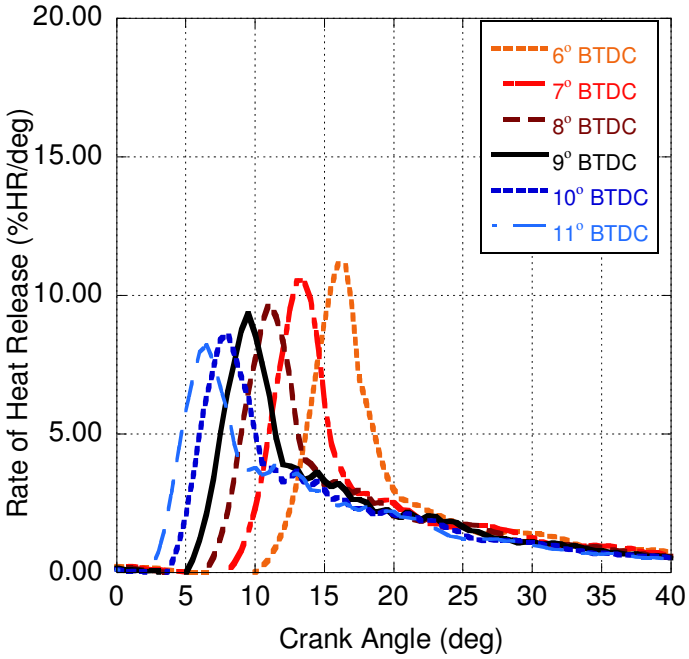

Figure 49. Normalized Rate of Heat Release for engine operating at 1800 RPM for 18.0 N-m of load, with varying injection timings.

The ignition timing, peak pressure location, and peak RHR location for MBT timing were linearly correlated for the loads lower than 18.0 N-m with R^2 values all greater than 0.97 (see Figure 50). For all five MBT timings, $IMEP_g$ rose linearly with load and $BSFC_g$ decreased reaching a level of 247.8 g $kW^{-1} h^{-1}$ at 13.5 and 18.0 N-m (see Figure 51). The linear increase for each of the three timings suggests that as the engine load (and fuel flow rate) increases, the engine's ability to overcome losses in availability from the rapid expansion of the piston also increases. This, in turn, allows the engine to sustain optimum combustion further from TDC, increasing the amount of torque that can be applied to the crankshaft (see Figure 52). This can also be seen in the change in normalized RHR for MBT timings; as engine load increases, the premixed spike loses magnitude, and the slope on either side of peak RHR decreases, as shown in Figure 53. In effect, the maximum heat release is sustained for a longer period. Note that the 18.0 N-m case was omitted from the linear correlations due to the authors' limitation of the pressure below 65 bar, potentially skewing the outcomes. The authors are attempting to contact the engine manufacturer in order to determine their specified maximum pressure for operation so that the efforts can be extended in the future.

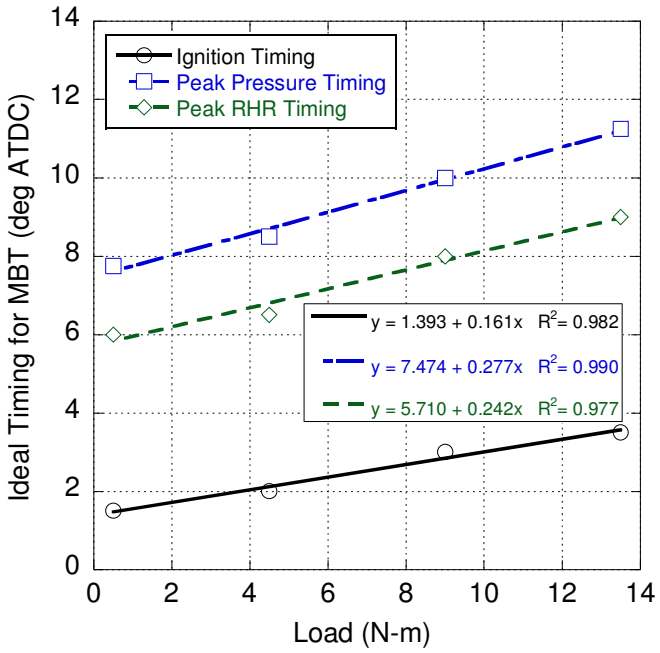

Figure 50. Ignition, peak pressure, and peak RHR timings for MBT at loads below 18.0 N-m.

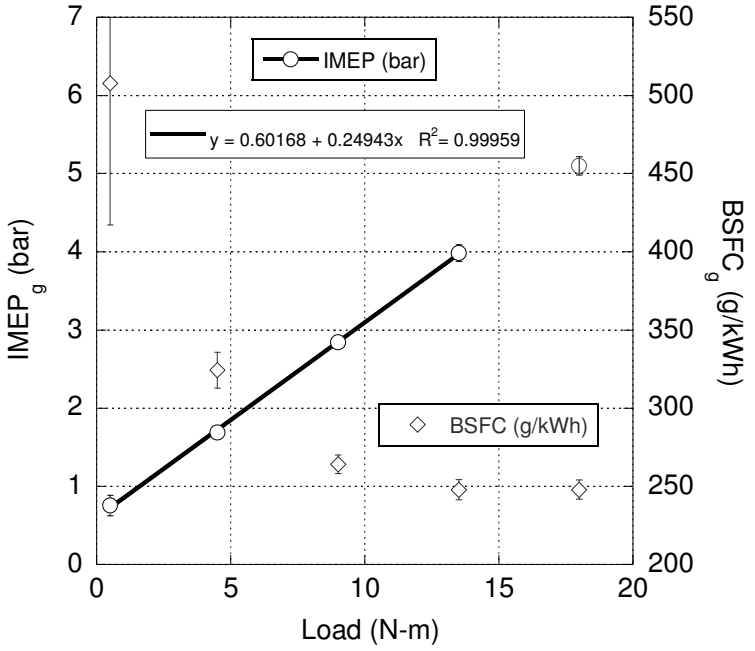

Figure 51. $BSFC_g$ and $IMEP_g$ for MBT timing at all loads.

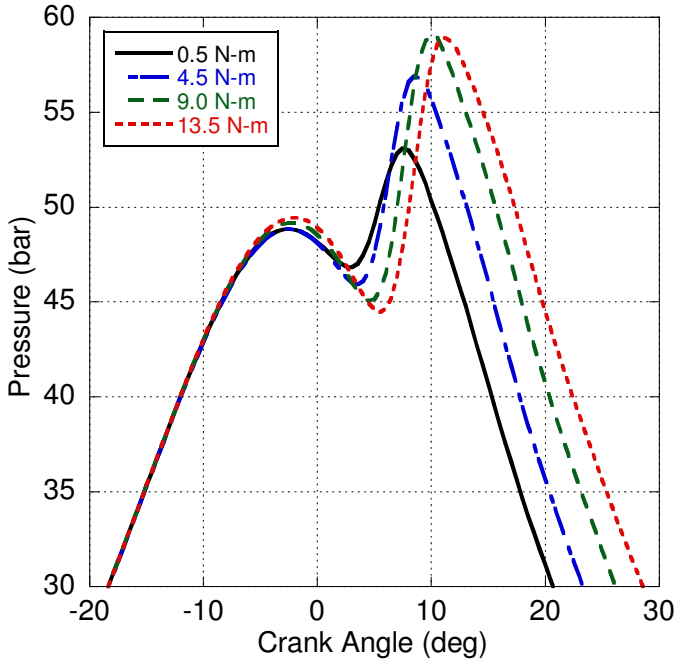

Figure 52. Pressure trace for MBT conditions at loads below 18.0 N-m.

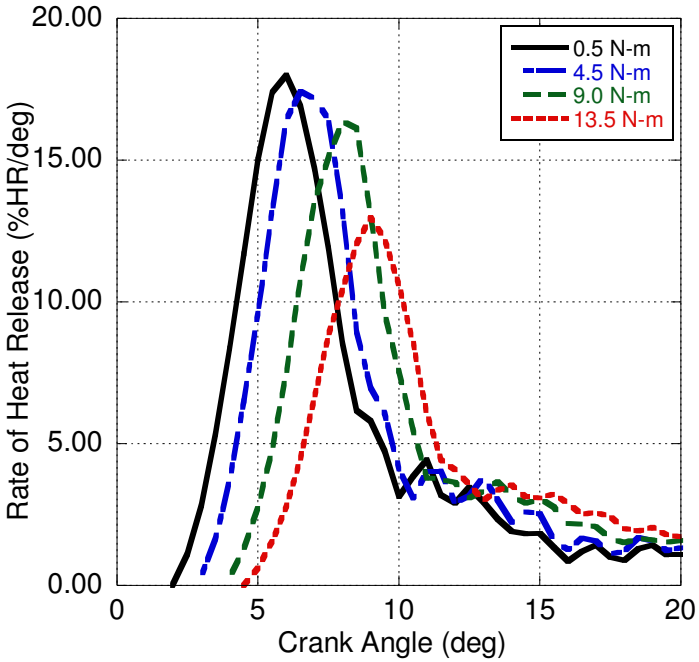

Figure 53. Normalized RHR for MBT conditions at loads below 18.0 N-m.

4.4.2 Injection, Ignition, Peak Pressure, and Peak Rate of Heat Release

The variations in ignition delay, peak pressure timing, and peak heat release timing with respect to injection timing at each load were compared in Figure 54. As injection was delayed, the injected fuel

spent less time at high pressures and temperatures, causing a nearly linear increase in ignition delay, with an average gain of 0.4° of ignition delay per degree of injection delay that held regardless of engine loading conditions (see Figure 54). For a given injection timing, ignition delay decreased with engine load because of the increased energy released to the chamber, causing hotter walls and promoting more heat transfer to the fuel as it initially mixes with air during injection.

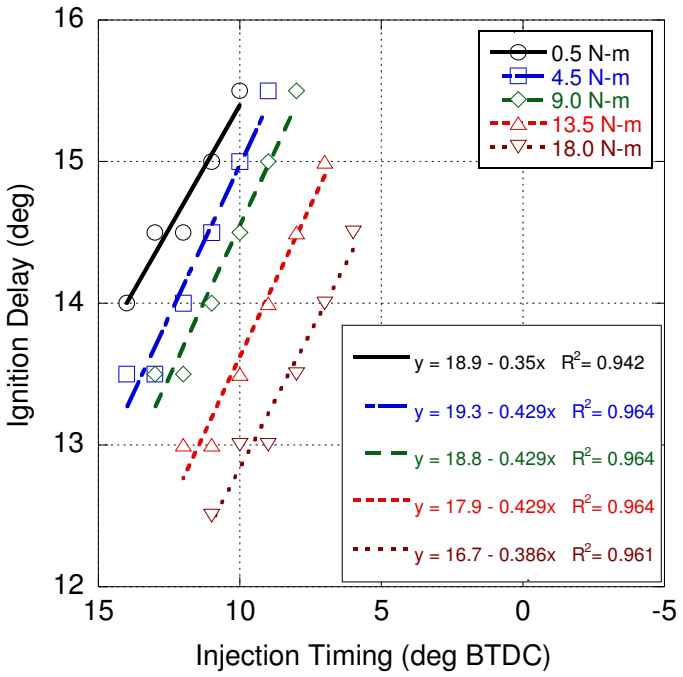

Figure 54. Relationship between Injection Timing and Ignition Delay at all engine loads.

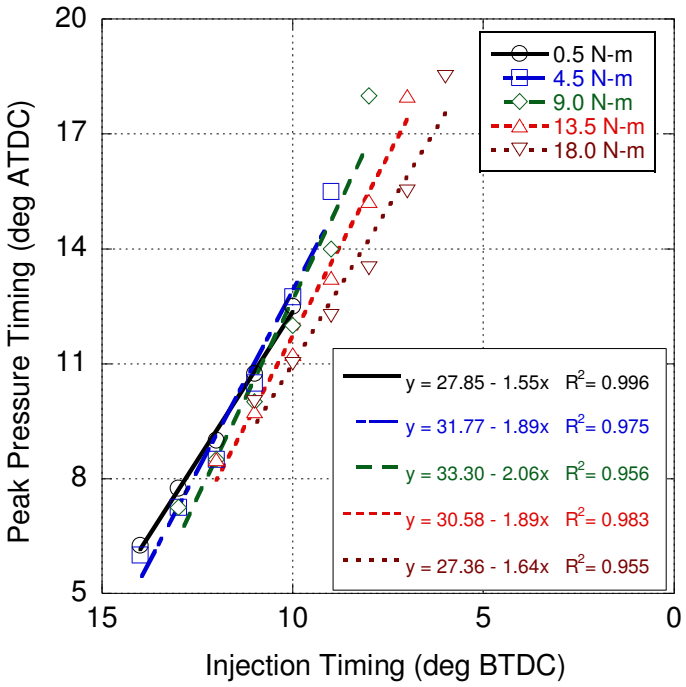

Figure 55. Relationship between Injection Timing and Peak Pressure Timing at all engine loads.

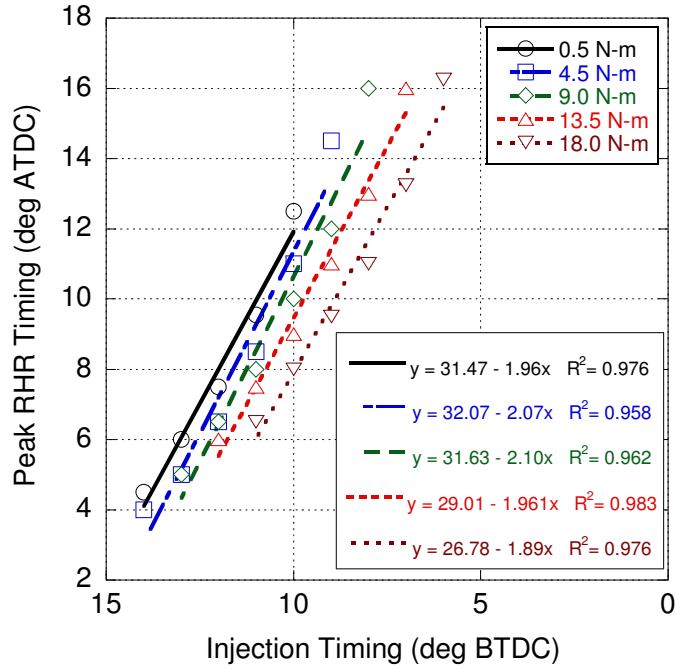

Figure 56. Relationship between Injection Timing and Peak RHR Timing at all engine loads.

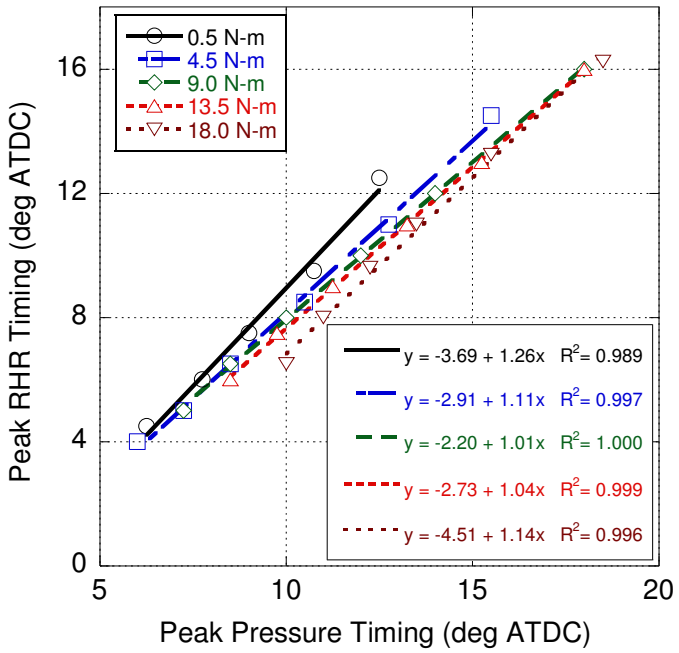

Figure 57. Relationship between Peak Pressure Timing and Peak RHR Timing at all engine loads.

Peak pressure and RHR timing both displayed a nearly linear correlation with injection timing, as shown in Figure 55 and Figure 56, respectively. As discussed earlier, the ignition delay increases linearly as injection is delayed, but this behavior alone cannot account for the increase in peak pressure delay seen in the change in slope with respect to loading seen in Figure 55. In addition, the slope of the RHR becomes noticeably less steep as injection is delayed, particularly immediately after ignition (see Figure 40-Figure 49). This suggests a slower acceleration of the rate of combustion once ignition occurs (also seen in decreasing slopes of the mass fraction burned profile not presented here), most likely due to the decreasing temperature within the cylinder from the piston expanding the working fluid, increasing the amount of energy needed to maintain combustion. As a result, for delayed injection timings, more energy liberated from the combustion of fuel must be used in order to continue the reaction, resulting in a delay in peak pressure and peak RHR. On average, there was a gain of 1.8° of peak pressure delay and 2.0° of peak RHR delay per degree of injection delay. At higher loads, where fuel is abundant and the temperature is relatively high, the peak pressure and peak RHR both occur sooner in the cycle because of a reduced ignition delay and timing. Peak pressure timing also showed a linear correlation with peak RHR timing, except for late injection at 0.5 N-m, and early injection at 18.0 N-m (see Figure 57). Generally,

peak RHR preceded peak pressure by 2.0-2.5° at 4.5, 9.0, and 13.5 N-m loading, with the gap between peak RHR and peak pressure increasing slightly with both engine load and injection delay.

4.4.3 MBT Timing Methods

The various MBT timing methods were compared against the peak pressure timing as a function of the injection timing. Each method produced a relatively linear correlation at engine loads below 18.0 N-m. For the peak value of the 1st derivative of the pressure trace, the change in pressure between crank angles was calculated directly, and the timing of the peak value in the vicinity of combustion was found, so as to exclude any peak value due to motoring behavior during the compression phase. For the various CA50 measurements, the mass fraction burned indicated by each method was compared, and the points at which the mass fraction burned exceeded 50% were catalogued. The two values were averaged for a third potential location, and the value closest to 50% mass fraction burned was used as the location of CA50. The MBT indicator timings can be seen in Figure 58 with respect to injection timing and Figure 59 with respect to engine load, and the equations and associated R^2 error of each trendline is given in Table 22 for Figure 58 and Table 23 for Figure 59.

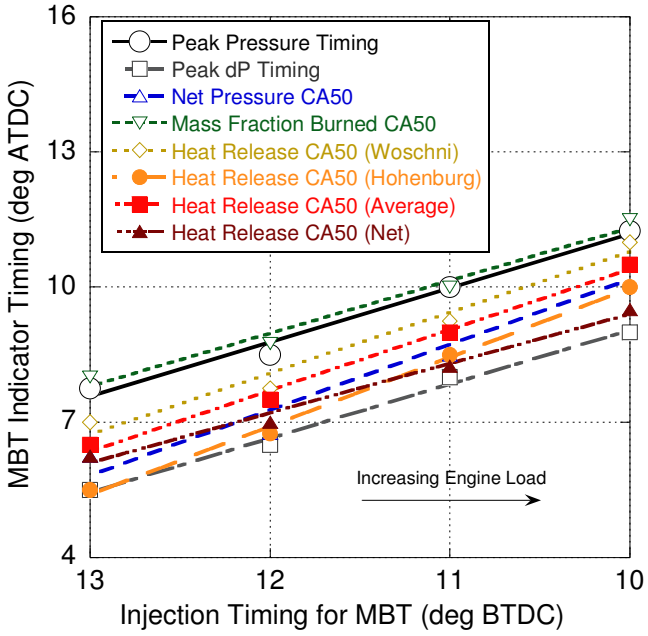

Figure 58. All timings for MBT indication methods for MBT injection timing for engine loads below 18.0 N-m at 1800 RPM.

Table 22. Equations of various linear MBT timing methods as a function of injection timing, with associated R^2 error from the gathered results.

MBT Timing Method	*m*	*B*	R^2
Peak Pressure	-1.20	23.18	0.985
Peak Pressure Derivative	-1.20	21.05	0.993
Net Pressure CA50	-1.45	24.68	0.945
Mass Fraction Burned CA50	-1.18	23.08	0.980
Heat Release (Woschni)	-1.35	24.28	0.972
Heat Release (Hohenburg)	-1.53	25.23	0.996
Heat Release (Average)	-1.35	23.90	0.992
Net Heat Release CA50	-1.10	20.40	0.988

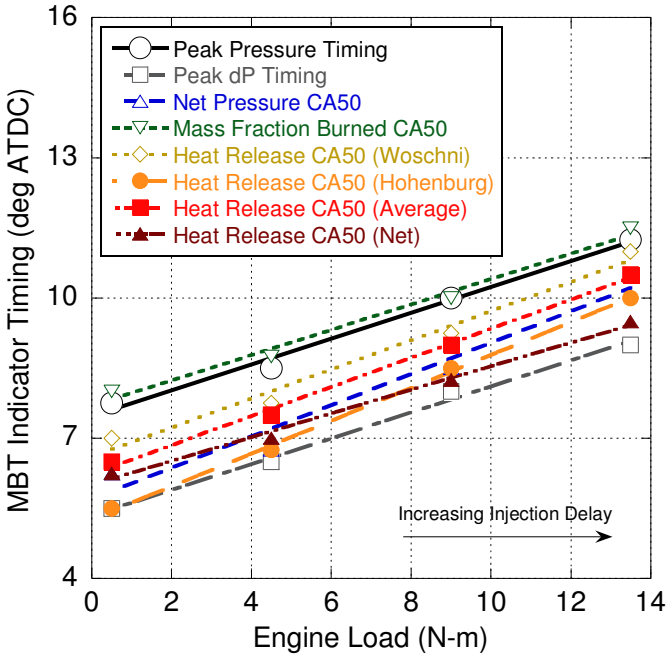

Figure 59. All timings for MBT indication methods for engine loads below 18.0 N-m at 1800 RPM.

Table 23. Equations of various linear MBT timing methods as a function of engine load, with associated R^2 error from the gathered results.

MBT Timing Method	*m*	*B*	R^2
Peak Pressure	0.277	7.474	0.990
Peak Pressure Derivative	0.276	5.353	0.994
Net Pressure CA50	0.335	5.695	0.957
Mass Fraction Burned CA50	0.271	7.700	0.987
Heat Release (Woschni)	0.316	6.608	0.980
Heat Release (Hohenburg)	0.351	5.276	0.998
Heat Release (Average)	0.311	6.238	0.996
Net Heat Release CA50	0.253	6.007	0.993

Of the methods used, the heat release methods for finding CA50 when using the Hohenburg and averaged heat transfer coefficients tended the most towards linearity. Net heat release CA50 also showed promise for correlation of MBT timing, with an R^2 only slightly lower than the peak pressure derivative in both cases, and slightly higher than the peak pressure method. Mass fraction burned CA50 and heat release CA50 with the Woschni coefficient showed less linearity, but were still within the realm of usability. The net pressure CA50 measurement showed a more obvious nonlinear behavior. Of the MBT methods used, the 1st derivative of pressure is the most preferred, given its high linearity and ease of use. Peak pressure is also highly preferred, due to its ease of implementation during experimentation. Net HR, as well as cumulative HR using the Hohenburg and averaged coefficients show promise, but may be more difficult to implement in real time for the purpose of calibration.

4.4.4 Emissions

The emissions catalogued during experimentation were also compared on a brake-specific basis, with each species tracked across the injection sweep at all engine loads. Brake-specific emissions of NO_x compounds generally fell as peak pressure timing was delayed due to the decreased cylinder temperatures encountered at later combustion timings (see Figure 60); i.e., thermal NO_x effect [3]. As a result, NO_x formation was largely independent of MBT timing. Only the last timing at 0.5 N-m encountered an increased brake-specific NO_x production after a delay in injection timing, which may reflect a slight loss of brake power for late injection timing (in effect, NO_x emissions were unchanged, but power production

fell). Additionally, this increase may be due to the prolonged combustion of the premixed spike seen in the RHR (see Figure 40), allowing the temperature to remain relatively high for a longer period, and providing a larger window for NO_x to form. Brake specific NO_x emissions fell with greater engine loads, due to large rises in engine output power without a significant change in temperature. Moreover, changes in NO_x emissions between timings at a given load became less pronounced as load was increased, with emissions at 0.5 N-m lowered by 42.4% (21.83 g/kWh) between maximum and minimum production; whereas, emissions at 18.0 N-m fell by only 15.0% (0.61 g/kWh) across the sweep. This is a function of the fuel injection process adding more energy in the diffusion burn phase in comparison to premixed (i.e., lower temperatures from the expanding cylinder volume and less residence time in the cylinder for the chemical kinetics based NO_x production process).

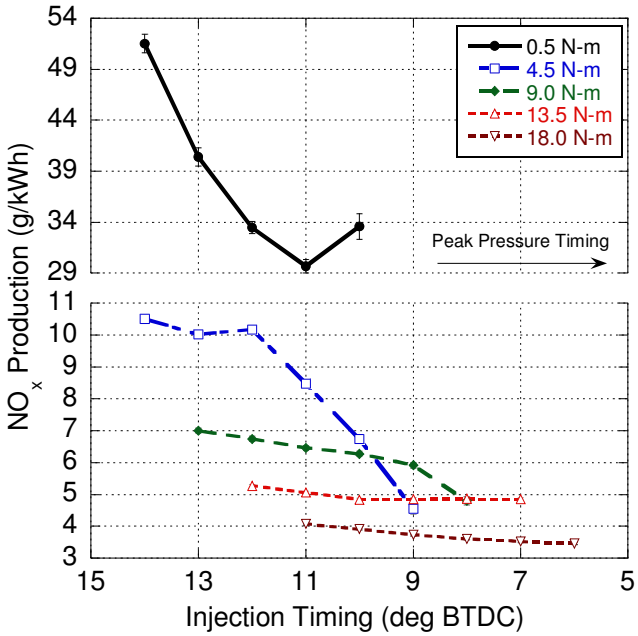

Figure 60. Brake specific production of NO_x for all tested engine loads at 1800 RPM.

Particulate matter (PM) emissions followed a trend separate from (but similar to) NO_x emissions. Like NO_x, PM emissions generally decreased as combustion was delayed further from TDC (lowering peak temperature), and was also largely independent of the increased efficiency of the MBT timings (see Figure 61), but did not display a great deal of consistency in the relationship between changes in timing and changes in PM, particularly at higher loads. This may be due in part to increasing uncertainties in

measurement as load was increased. Unlike NO_x production, which is linked to higher temperatures, PM emissions fell due to the lessened diffusion burn as injection and ignition timing were delayed. It is assumed that this is somewhat buffered by the fact that temperatures did decrease resulting in a slightly reduced PM oxidation rate. In addition, brake-specific PM emissions increased with larger loads, reflecting the more pronounced diffusion burn phases seen at higher loads (see Figure 46 and Figure 48). PM emissions at 0.5 N-m followed significantly different trends, showing a large net increase for late combustion timings. Like the increase seen in NO_x emissions, this is more due to the decrease in power production for later combustion, rather than an increase in emissions, and was magnified by the unsteady combustion experienced at 0.5 N-m. PM emissions between 0.5 N-m and 4.5 N-m showed no meaningful increase on an absolute scale, but power production at 4.5 N-m was much higher, leading to the decrease in brake-specific PM emissions between 0.5 and 4.5 N-m.

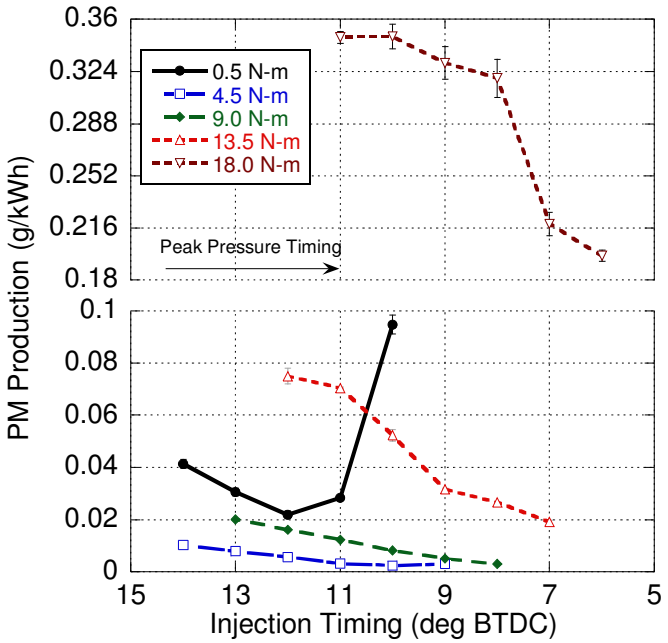

Figure 61. Brake specific production of PM for all tested engine loads at 1800 RPM.

CO and THC specific emissions (see Figure 62 and Figure 63) increased at all loads as injection was delayed, highlighting the decreased combustion efficiency for later combustion events as peak temperatures in the cylinder decrease. In addition, the increasing fuel flow rate (providing more hydrogen and carbon atoms) and the associated rise in equivalence ratio are both likely additional causes of the

increase in emissions of both CO and THC species. In the case of THC emissions, a longer ignition delay with delayed injection timings could result in more overleaning at the periphery of the fuel injection stream adding to its increased rate of emissions. For CO emissions, decreasing peak temperatures caused by delayed injection and combustion may buffer the increase in CO emissions slightly through a reduced dissociation level of CO_2 into CO. In addition, delayed injection timings will allow for better mixing of the fuel and air as the ignition delay increases; hence, CO and THC could decrease slightly because of this effect [3, 173]. Production of both groups fell with load because of the higher temperatures generated creating a greater potential for oxidation that outweighed the effects of increasing equivalence ratio. For CO, this is counteracted slightly by the increased potential for dissociation caused by higher peak temperatures. At low loads, increases in THC emissions could also be due to the relatively cool regions away from the fuel injector, increasing the possibility of flame quenching and resulting in inefficient combustion [4]. For highly delayed injection timings, the rapid rise in THC emissions was accompanied by the large increase in fuel flow rate used to signify that the engine had left the MBT timing envelope.

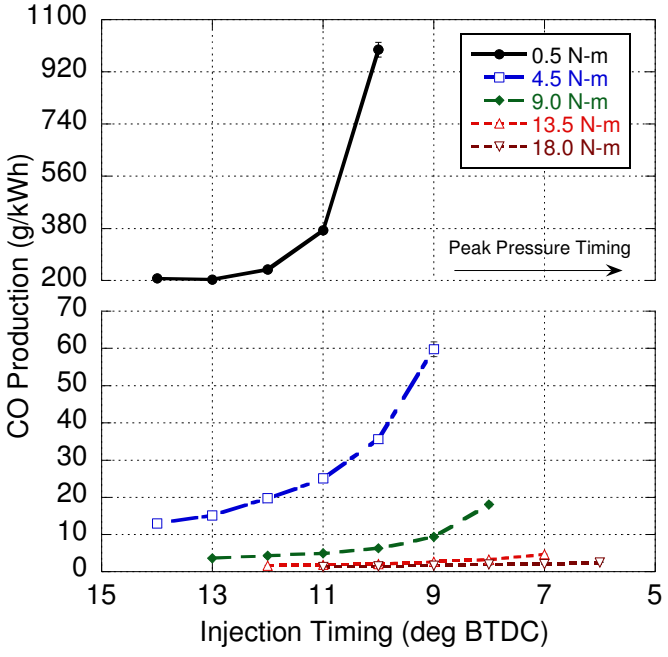

Figure 62. Brake specific production of CO emissions for all tested engine loads at 1800 RPM.

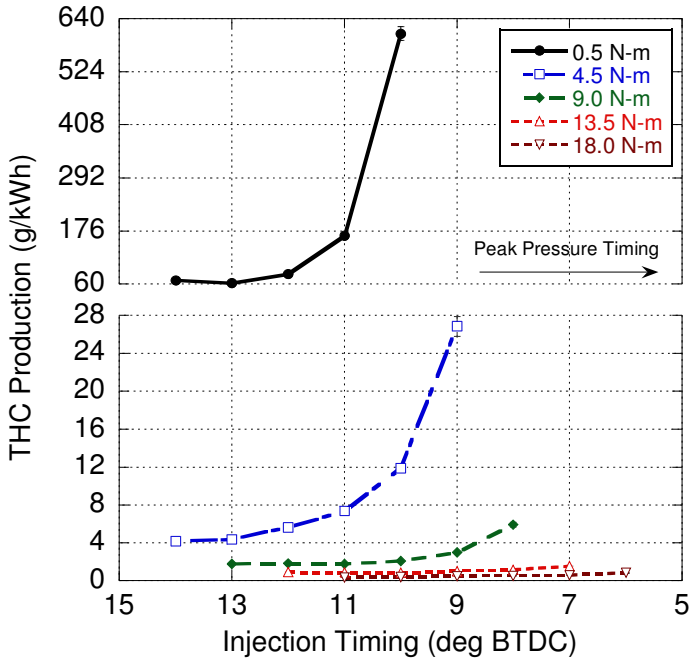

Figure 63. Brake specific production of THC emissions for all tested engine loads at 1800 RPM.

A speciation of THC emissions for a given load can be seen in Figure 64 (0.5 N-m), Figure 65 (4.5 N-m), Figure 66 (9.0 N-m), Figure 67 (13.5 N-m), and Figure 68 (18.0 N-m). THC emissions were broken down into subgroups according to similar volatility, chemical structure, and common reactions to catalysis [172]. Emissions of n-octanes represented partially oxidized fuel molecules, as well as some heavy HC species, and are given (on an absolute scale) in Figure 69. Aldehydes and ketones (A/K) were grouped together based on similar volatility, chemical structure, and ozone forming ability, and were largely represented by emissions of formaldehyde and acetaldehyde. Aromatic HCs were most likely formed most of emissions of BTEX compounds, as well as some higher-order polycyclic aromatic HCs composed from the benzene ring structure (C_6H_6). Slow-oxidizing compounds represented species resistant to catalysis, and included emissions of acetylene, ethene, ethane, propene, and other low-carbon number emissions. Methane was separated from the slow-oxidizing compounds, due to its unique resistance to catalytic measures. For all loads, the cumulative THC emissions and the sum of the various emissions components were largely in agreement, and the measurements only disagreed with each other at low loads, most likely due to higher uncertainty from high cyclic variation in engine operation at 0.5 and 4.5 N-m.

For combustion timings at all loads, the largest portion of THC emissions was from n-octanes that had survived combustion or only undergone partial oxidation. As THC emissions increased for later injection timings, the absolute magnitude of n-octanes also increased as well, while the fraction of n-octane emissions as a part of the THC emissions decreased. This may indicate that the emission of n-octane emissions are largely due to flame quenching as combustion moves towards cooler parts of the cylinder, and is also shown in the decrease in n-octane emissions at higher loads, where flame quenching is less likely in the high temperature environment.

The decreasing fraction of n-octanes within THC emissions highlights the falling combustion efficiency seen for significantly delayed injection timings [4, 174]. In essence, the temperatures within the cylinder are lower and more fuel is added providing a greater capacity for more partial oxidation combustion reactions. This is buffered slightly by an increased mixing level due to longer ignition delays. These species are largely represented by A/K species, as well as slow-oxidizing compounds. The fraction of THC emissions taken up by methane also increased, although never by more than 2% over the course of the injection sweep.

Aromatic emissions showed a great amount of variability. For injection timings in the vicinity of MBT, emissions of aromatics were minimized (and often below readable levels). However, for injection timings at the either extreme of the tested ranges, aromatic emissions saw marked increases. In addition, these increases were typically sudden, as aromatics ballooned from 1-2% to over 10% of THC emissions over a 1° change in injection timing. At both extremes, aromatic emissions seemed to come at the expense of n-octanes. In the case of highly advanced injection, this is most likely due to poor mixing of the injected fuel due to a shorter ignition delay, increasing the partial oxidation of fuel molecules to form aromatics without also forming aldehydes, ketones, or slow-oxidizing species. In addition, the conditions at these extremes were more favorable to allow for the continued existence of the aromatic compounds, keeping them from breaking down into lower carbon number HCs. For highly delayed injection, the formation of aromatics is through partial oxidation of fuel, as well as kinetic reactions between the various slow-oxidizing compounds promoted by the prolonged heat of delayed combustion and increased

exhaust temperatures [175]. Emissions of aromatics for delayed injection also appeared to lower the fraction of A/K species slightly and slow-oxidizing compounds within the exhaust emissions. This behavior may indicate a correlation between MBT and aromatic HC emissions. However, any correlation technique based on aromatic emissions levels may be difficult because of the low levels of aromatic emissions present, which are often below the measurment threshold of lab equipment.

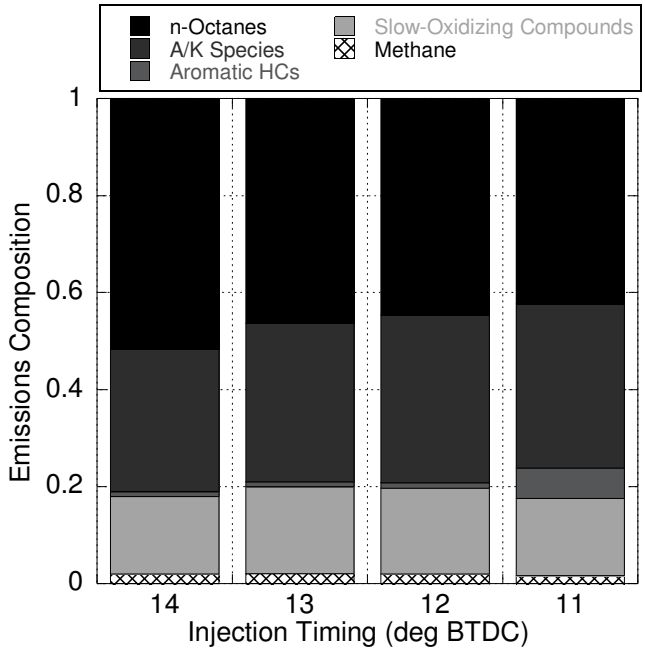

Figure 64. Fractional composition of THC species at 1800 RPM at 0.5 N-m.

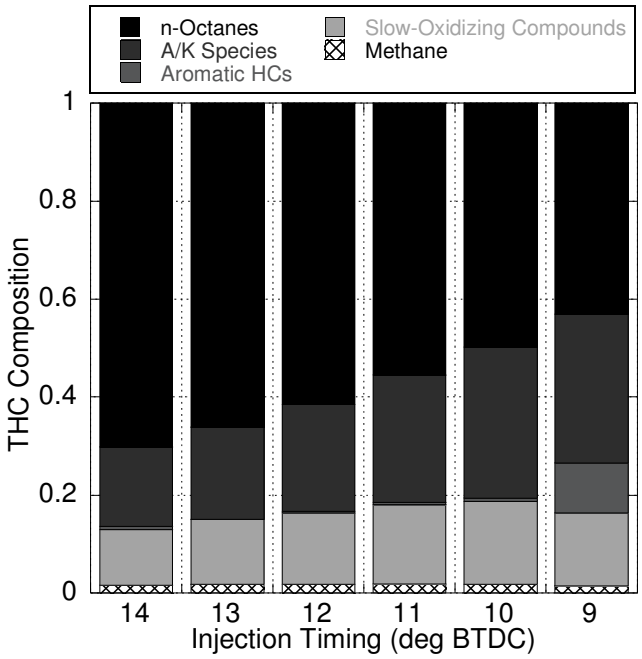

Figure 65. Fractional composition of THC species at 1800 RPM at 4.5 N-m.

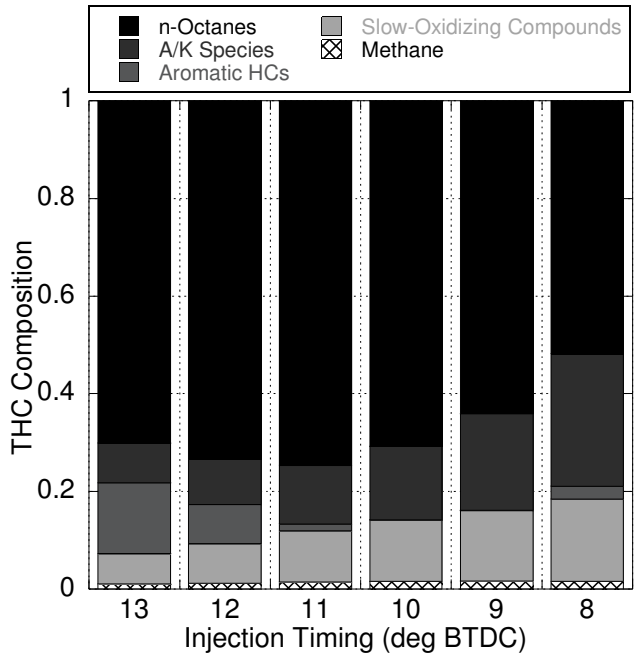

Figure 66. Fractional composition of THC species at 1800 RPM at 9.0 N-m.

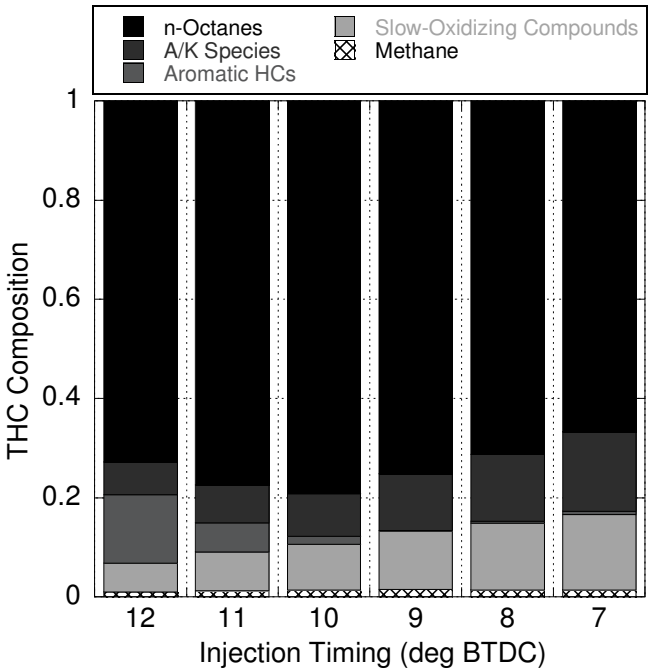

Figure 67. Fractional composition of THC species at 1800 RPM at 13.5 N-m.

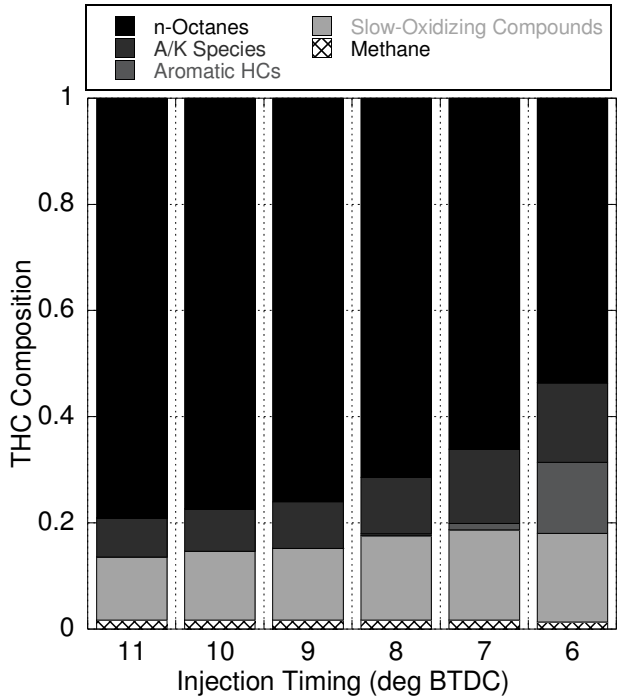

Figure 68. Fractional composition of THC species at 1800 RPM at 18.0 N-m.

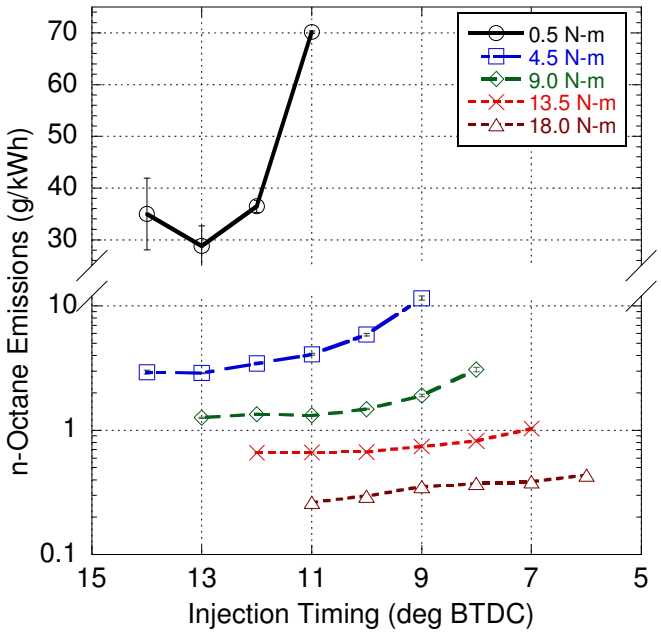

Figure 69. Emissions of n-octane for all engine loads at 1800 RPM.

4.5 Conclusions

A number of MBT timing correlations utilizing a novel HR model have been explored for a DI-CI engine, and exhibit similar behavior to the established peak pressure and net HR methodologies. The benefit of these timing strategies is a reduced calibration time for the same engine operating at speeds other than 1800 RPM. The peak pressure and 1st derivative of the pressure trace are the most promising methods for MBT timing, due to their high linearity and ease of use. The HR indicated correlations may have higher linearity, but would be difficult to use without a real-time HR model available during engine operation. Although MBT timing could not be conclusively found at the highest engine load due to peak pressure limitations, the effective MBT timing was estimated by extrapolating the timing locations from lower loading situations.

Operating within the MBT timing envelope is beneficial for both power production and limiting of emissions. $BSFC_g$ increases slightly on either side of MBT, particularly at loads above 4.5 N-m. At the highest engine loads, where air-limited combustion is encountered, MBT timing is less certain, as the changes in engine operation from variations in injection timing are small. Once the engine has left the

MBT envelope, however, engine operation becomes notably less efficient. The end of this timing envelope is marked by a large increase in fuel flow rate, as well as a rapid rise in CO and THC emissions.

Measured emissions of NO_x and PM are generally removed from MBT timing considerations, as emissions of both species are more dependent on engine load and cylinder temperature in comparison to the fraction of pre-mixed and diffusion burned phases. This is evident by NO_x emissions decreasing with delayed injection timings even though the pre-mixed spike increases. As a result, emissions of NO_x compounds and PM are lowered as injection is delayed, even if the engine exits the MBT timing envelope altogether. CO and THC emissions are minimized in the vicinity of MBT timing. In addition, aromatic HC species tend to be minimized (often to negligible amounts) for injection timings slightly later than MBT, and n-octane emissions are maximized as a fraction of THC emissions at MBT timing. All other HC species appear to generally increase with delayed combustion until the engine leaves the MBT envelope, at which point the fraction of aromatics begins to climb at the expense of the other THC species. However, the competing emissions production (NO_x and PM vs. THC and CO) within the MBT envelope presents a challenge in finding the precise location at which one should operate. It is most likely that operation would be later than MBT, in order to decrease NO_x and PM emissions, and would come at the expense of increased THC and CO emissions. Most notably, changes in the emissions of these species caused by variation in injection timing may increase dependency on aftertreatment devices in order to meet emissions regulations, which can be problematic for control of more resistant HC species (e.g.; BTEX and methane), and would most likely be further complicated by the use of biofuels that can significantly change the engine-out emissions profile.

References

1. Owen, N.A., O.R. Inderwildi, and D.A. King, *The status of conventional world oil reserves—Hype or cause for concern?* Energy Policy, 2010. 38(8): p. 4743-4749.
2. Chapman, I., *The end of Peak Oil? Why this topic is still relevant despite recent denials.* Energy Policy.
3. Heywood, J.B., *Internal Combustion Engine Fundamentals,* 1988: McGraw-Hill, Inc. 930.
4. Bhusnoor, S.S., M.K.G. Babu, and J.P. Subrahmanyam, *Studies on Performance and Exhaust Emissions of a CI Engine Operating on Diesel and Diesel Biodiesel Blends at Different Injection Pressures and Injection Timings*, 2007, SAE International.
5. Genzale, C.L., L.M. Pickett, and S. Kook, *Liquid Penetration of Diesel and Biodiesel Sprays at Late-Cycle Post-Injection Conditions.* SAE Int. J. Engines, 2010. 3(1): p. 479-495.
6. Bittle, J.A., B.M. Knight, and T.J. Jacobs, *The Impact of Biodiesel on Injection Timing and Pulsewidth in a Common-Rail Medium-Duty Diesel Engine.* SAE Int. J. Engines, 2009. 2(2): p. 312-325.
7. Sharp, C.A., S.A. Howell, and J. Jobe, *The Effect of Biodiesel Fuels on Transient Emissions from Modern Diesel Engines, Part I Regulated Emissions and Performance*, 2000, SAE International: SAE Techincal Paper 2000-01-1967.
8. Sharp, C.A., S.A. Howell, and J. Jobe, *The Effect of Biodiesel Fuels on Transient Emissions from Modern Diesel Engines, Part II Unregulated Emissions and Chemical Characterization*, 2000, SAE International: SAE Techincal Paper 2000-01-1968.
9. U.S. Environmental Protection Agency, *A Comprehensive Analysis of Biodiesel Impacts on Exhaust Emissions*, 2002.
10. Ragone, J.C., *Emission Reduction and Assisted Combustion Strategies for Compression Ignition Engines with Subsequent Testing on a Single-Cylinder Engine*, in *Department of Mechanical Engineering*2012, University of Kansas: Lawrence, KS.
11. Mangus, M.D., *Design, Construction, and Validation of an In-Cylinder Pressure Recording System for Internal Combustion Engine Analysis*, in *Department of Mechanical Engineering, School of Engineering,* 2012, University of Kansas: Lawrence, Kansas.
12. *Federal Register; Tuesday, January 17, 2006; Rules and Regulations*, 2006. p. 2810-2842.
13. *Fegeral Register; Thursday, October 16, 2008; Rules and Regulations*, 2008. p. 61358-61363.
14. *Clean Air Act - Mobile Source Civil Penalty Policy*, in *7521-7590*2009.
15. Barths, H., C. Antoni, and N. Peters, *Three-Dimensional Simulation of Pollutant Formation in a DI Diesel Engine Using Multiple Interactive Flamelets*, 1998, SAE International.
16. U.S. Environmental Protection Agency, *Automobile Emissions: An Overview*, 1992, EPA National Vehicle and Fuel Emissions Laboratory: Ann Arbor, MI. p. 4.
17. Chagger, H.K., et al., *The nature of hydrocarbon emissions formed during the cooling of combustion products.* Fuel, 1997. 76(9): p. 861-864.
18. U.S. Environmental Protection Agency, *Consumer Factsheet on: BENZENE*, 2010.
19. U.S. Environmental Protection Agency, *Benzene; TEACH Chemical Summary*, 2009.
20. Bayliss, D., J. Jinot, and B. Sonawane, *Toxicological Review of Benzene (Noncancer Effects)*, 2002, U.S. Environmental Protection Agency.
21. Clinton, M. and American Petroleum Institute, *API Toxicological Review: Benzene*, 1948.
22. U.S. Department of Energy, *4: The BTX Chain: Benzene, Toluene, Xylene* 2012.
23. New Hampshire Department of Environmental Services, *Toluene: Health Information Summary*, 2005.
24. *The Clean Air Act*, 2004.
25. Forster, P., et al., *Chapter 2: Changes in Atmospheric Constituents and in Radiative Forcing.* Climate Change 2007: The Physical Science Basis, 2007.
26. Kuo, J.C.W., C.R. Morgan, and H.G. Lassen, *Mathematical Modeling of CO and HC Catalytic Converter Systems*, 1971, SAE International: SAE Technical Paper 710289.

27. Depcik, C. and D. Assanis, *One-Dimensional Automotive Catalyst Modeling.* Progress in Energy and Combustion Science, 2005. 31(4): p. 308-369.
28. Gottberg, I., et al., *New Potential Exhaust Gas Aftertreatment Technologies for "Clean Car" Legislation*, 1991, SAE International: SAE Technical Paper 910840.
29. Montreuil, C.N., S.C. Williams, and A.A. Adamczyk, *Modeling Current Generation Catalytic Converters: Laboratory Experiments and Kinetic Parameter Optimization - Steady State Kinetics*, 1992, SAE International: SAE Techincal Paper 920096.
30. Edelbauer, W., S. Kutschi, and J.C. Wurzenberger, *xD+1D Catalyst Simulation-A Numerical Study on the Impact of Pore Diffusion.* SAE Int. J. Engines, 2012. 5(3): p. 1459-1476.
31. Morin, J.-P., et al., *Toxic Impacts of Emissions from Small 50cc Engine Run under EC47 Driving Cycle: A Comparison between 2-Stroke and 4-Stroke Engines and Lube Oil Quality and Ethanol Additivation.* SAE Int. J. Engines, 2011. 4(2): p. 2490-2497.
32. Cooper, B.J., *Challenges in Emission Control Catalysis for the Next Decade.* Platinum Metals Review, 1994. 38(1): p. 2-10.
33. Adams, K.M., et al., *Laboratory Screening of Diesel Oxidation Catalysts and Validation with Vehicle Testing: The Importance of Hydrocarbon Stroage*, 1996, SAE International: SAE Technical Paper 962049.
34. Thomas, V.M. and T.G. Spiro, *An Estimation of Dioxin Emissions in the United States.* Toxicological and Environmental Chemistry, 1995. 50: p. 1-37.
35. Kasprzyk-Hordern, B., et al., *MTBE, DIPE, ETBE and TAME degradation in water using perfluorinated phases as catalysts for ozonation process.* Applied Catalysis B: Environmental, 2004. 51(1): p. 51-66.
36. Lapuerta, M., O. Armas, and J. Rodríguez-Fernández, *Effect of biodiesel fuels on diesel engine emissions.* Progress in Energy and Combustion Science, 2008. 34(2): p. 198-223.
37. Canadian Renewable Fuels Association, *Biodiesel: Key Issues*, 2010.
38. Lea-Langton, A., H. Li, and G.E. Andrews, *Comparison of Particulate PAH Emissions for Diesel, Biodiesel and Cooking Oil using a Heavy Duty DI Diesel Engine*, 2008, SAE International: SAE Technical Paper 2008-01-1811.
39. U.S. Department of Health and Human Services, *Toxicological Profile for n-Hexane*, 1999.
40. Lah, K., *Polycyclic Aromatic Hydrocarbons*, 2011.
41. Hardinger, S., *Chemistry Tutorial: Aromaticity*, 2012, University of California at Los Angeles.
42. Larsen, J.C. and European Comissions, *Polycyclic Aromatic Hydrocarbons - Occurrence in foods, dietary exposure and health effects*, 2002.
43. Westerholm, R. and K.-E. Egeback, *Exhaust Emissions from Light- and Heavy-duty Vehicles: Chemical Composition, Impact of Exhaust After Treatment, and Fuel Parameters.* Environmental Health Perspectives, 1994. 102: p. 13-23.
44. Stokman, S.K. *Estimates of Concentrations of Soluble Petroluem Hydrocarbons Migrating into Ground Water from Contaminated Soil Sources*. in *Conference on Petroleum Hydrocarbons and Organic Chemicals in Groundwater, Prevention, Detection and Restoration*. 1987. Houston, TX: Association of Ground Water Scientists and Engineers.
45. Weelink, S.A.B., M.H.A. Eekert, and A.J.M. Stams, *Degradation of BTEX by anaerobic bacteria: physiology and application.* Reviews in Environmental Science and Bio/Technology, 2010. 9(4): p. 359-385.
46. New Hampshire Department of Environmental Services, *Ethylbenzene: Health Information Summary*, 2004.
47. New Jersey Department of Health & Senior Services, *Hazardous Substance Fact Sheet: Xylenes*, 2011.
48. Organization for Economic Cooperation and Development, *Formaldehyde: SIDS Initial Assessment Report*, 2002.
49. Gomes, R., et al., *Acrolein: Concise International Chemical Assessment Document 43*, 2002.

50. New Hampshire Department of Environmental Services, *Acetone: Health Information Summary*, 2005.
51. Sillman, S., *Overview: Tropospheric ozone, smog, and ozone-NOx-VOC sensitivity*, in *Treatise on Geochemistry*2003, Elsevier: University of Michigan.
52. Sillman, S., *The relation between ozone, NOx and hydrocarbons in urban and polluted rural environments.* Atmospheric Environment, 1999. 33(12): p. 1821-1845.
53. U.S. Environmental Protection Agency, *Automobiles and Ozone*, 1992, EPA National Vehicle and Fuel Emissions Laboratory: Ann Arbor, Ml. p. 6.
54. Green, P., *An Investigation of the Potential for Ground-Level Ozone Formation Resulting from Compost Facility Emissions*, 2010, University of California, Davis. p. 10, 28-30.
55. Carter, W.P.L., *Development of Ozone Reactivity Scales for Volatile Organic Compounds.* Journal of the Air and Waste Management Association, 1994. 44: p. 881-889.
56. Sendzikiene, E., V. Makareviciene, and P. Janulis, *Influence of fuel oxygen content on diesel engine exhaust emissions.* Renewable Energy, 2006. 31(15): p. 2505-2512.
57. Chen, H., et al., *Study of oxygenated biomass fuel blends on a diesel engine.* Fuel, 2008. 87(15–16): p. 3462-3468.
58. Wang, X., et al., *Diesel engine gaseous and particle emissions fueled with diesel–oxygenate blends.* Fuel, 2012. 94(0): p. 317-323.
59. Monyem, A. and J. H. Van Gerpen, *The effect of biodiesel oxidation on engine performance and emissions.* Biomass and Bioenergy, 2001. 20(4): p. 317-325.
60. Pinto, A.C., et al., *Biodiesel: An Overview.* Journal of the Brazillian Chemical Society, 2005. 16(6b).
61. Nabi, M.N. and J.E. Hustad, *Influence of oxygenates on fine particle and regulated emissions from a diesel engine.* Fuel, 2012. 93(0): p. 181-188.
62. Robbins, C., et al., *Effects of Biodiesel Fuels Upon Criteria Emissions*, 2011, SAE International: SAE Technical Paper 2011-01-1943.
63. Zhihao, M., et al., *Study on Emissions of a DI Diesel Engine Fuelled with Pistacia Chinensis Bunge Seed Biodiesel-Diesel Blends.* Procedia Environmental Sciences, 2011. 11, Part C(0): p. 1078-1083.
64. Tan, P.-q., et al., *Exhaust emissions from a light-duty diesel engine with Jatropha biodiesel fuel.* Energy, 2012. 39(1): p. 356-362.
65. Sinha, S. and A.K. Agarwal, *Performance Evaluation of a Biodiesel (Rice Bran Oil Methyl Ester) Fuelled Transport Diesel Engine*, 2005, SAE International: SAE Technical Paper 2005-01-1730.
66. Millo, F., D. Vezza, and T. Vlachos, *Effects of Rapeseed and Jatropha Methyl Ester on Performance and Emissions of a Euro 5 Small Displacement Automotive Diesel Engine*, 2011, SAE International: SAE Techincal Paper 2011-24-0109.
67. Gumus, M., C. Sayin, and M. Canakci, *The impact of fuel injection pressure on the exhaust emissions of a direct injection diesel engine fueled with biodiesel–diesel fuel blends.* Fuel, 2012. 95(0): p. 486-494.
68. Knothe, G., *Historical Perspectives on Vegetable Oil-Based Diesel Fuels.* Inform, 2001. 12(11): p. 1103-1107.
69. Labeckas, G. and S. Slavinskas, *The effect of rapeseed oil methyl ester on direct injection Diesel engine performance and exhaust emissions.* Energy Conversion and Management, 2006. 47(13–14): p. 1954-1967.
70. Cecrle, E., et al., *An Investigation of the Effects of Biodiesel Feedstock on the Performance and Emissions of a Single-Cylinder Diesel Engine.* Energy and Fuels, 2012.
71. Karavalakis, G., et al., *Effect of Biodiesel Origin on the Regulated and PAH Emissions from a Modern Passenger Car*, 2011, SAE International: SAE Technical Paper 2011-01-0615.
72. Northrop, W.F., S.V. Bohac, and D.N. Assanis, *Premixed Low Temperature Combustion of Biodiesel and Blends in a High Speed Compression Ignition Engine.* SAE Int. J. Fuels Lubr., 2009. 2(1): p. 28-40.

73. Aakko, P., et al., *Emissions from Heavy-Duty Engine with and without Aftertreatment Using Selected Biofuels*, 1999.
74. McGill, R., et al., *Emission Performance of Selected Biodiesel Fuels*, 2003, SAE International: SAE Technical Paper 2003-01-1866.
75. Chase, C.L., et al., *A 322,000 kilometer (200,000 mile) Over the Road Test with HySEE Biodiesel in a Heavy Duty Truck*, 2000, SAE International: SAE Technical Paper 2000-01-2647.
76. Chauhan, B.S., N. Kumar, and H.M. Cho, *A study on the performance and emission of a diesel engine fueled with Jatropha biodiesel oil and its blends.* Energy, 2012. 37(1): p. 616-622.
77. Pandey, A.K. and M.R. Nandgaonkar, *Comparison and Evaluation of Performance, Combustion and Emissions of Diesel, Jatropha and Karanja Oil Methyl Ester Biodiesel in a Military 780 hp CIDI Engine*, 2010, SAE International: SAE Techincal Paper 2010-01-2138.
78. Lapuerta, M., et al., *Biodiesel from Low-Grade Animal Fats: Diesel Engine Performance and Emissions.* Energy Fuels, 2009. 23(1): p. 121-129.
79. Takayuki, M. and M. Takaaki, *Diesel Engine Operation and Exhaust Emissions When Fueled with Animal Fats*, 2005, SAE International: SAE Techincal Paper 2005-01-3673.
80. Hinshaw, J.V., *The Flame Ionization Detector*, 2005: LCGC North America.
81. U.S. Environmental Protection Agency, *Conversion Factors for Hydrocarbon Emission Components*, 2005. p. 4.
82. Anstalt für Verbrennungskraftmaschinen List, *CSC SESAM-FTIR Emissions Challenge Data*, 2009.
83. Cramers, C.A., et al., *High-speed gas chromatography: an overview of various concepts.* Journal of Chromatography A, 1999. 856(1–2): p. 315-329.
84. Ferreira, S.L., et al., *Analysis of the emissions of volatile organic compounds from the compression ignition engine fueled by diesel–biodiesel blend and diesel oil using gas chromatography.* Energy, 2008. 33(12): p. 1801-1806.
85. He, C., et al., *Characteristics of polycyclic aromatic hydrocarbons emissions of diesel engine fueled with biodiesel and diesel.* Fuel, 2010. 89(8): p. 2040-2046.
86. Acharya, K., et al., *Effect of Different Biodiesel Blends on Autoignition, Combustion, Performance and Engine-Out Emissions in a Single Cylinder HSDI Diesel Engine*, 2009, SAE International: SAE Technical Paper 2009-01-0489.
87. Foster, D.E., *An Overview of Zero-Dimensional Thermodynamic Models for IC Engine Data Analysis*, 1985, SAE International.
88. Jensen, T.K. and J. Schramm, *A Three-Zone Heat Release Model for Combustion Analysis in a Natural Gas SI Engine. -Effects of Crevices and Cyclic Variations on UHC Emissions*, 2000, SAE International.
89. Brand, D., C.H. Onder, and L. Guzzella, *Estimation of the Instantaneous In-Cylinder Pressure for Control Purposes using Crankshaft Angular Velocity*, 2005, SAE International.
90. Friedrich, I., H. Pucher, and T. Offer, *Automatic Model Calibration for Engine-Process Simulation with Heat-Release Prediction*, 2006, SAE International.
91. Ravaglioli, V., et al., *MFB50 On-Board Evaluation Based on a Zero-Dimensional ROHR Model*, 2011, SAE International.
92. Rassweiler, G.M. and L. Withrow, *Motion Pictures of Engine Flames Correlated with Pressure Cards*, 1938, SAE International.
93. Brunt, M.F.J., H. Rai, and A.L. Emtage, *The Calculation of Heat Release Energy from Engine Cylinder Pressure Data*, 1998, SAE International.
94. Brunt, M.F.J. and K.C. Platts, *Calculation of Heat Release in Direct Injection Diesel Engines*, 1999, SAE International.
95. Shayler, P.J., M.W. Wiseman, and T. Ma, *Improving the Determination of Mass Fraction Burnt*, 1990, SAE International.
96. Vibe, I.I., *Brennverlauf und Kreisprozess von Verbrennungsmotoren*1969, Berlin: VEB Verlag Technik.

97. Egnell, R., *A Simple Approach to Studying the Relation between Fuel Rate Heat Release Rate and NO Formation in Diesel Engines*, 1999, SAE International.
98. Matekunas, F.A., *Engine combustion control with ignition timing by pressure ratio management*, 1986, Google Patents.
99. Sellnau, M.C., et al., *Cylinder-pressure-based engine control using pressure-ratio-management and low-cost non-intrusive cylinder pressure sensors.* SAE transactions, 2000. 109(3): p. 899-918.
100. Grimm, B.M. and R.T. Johnson, *Review of Simple Heat Release Computations*, 1990, SAE International.
101. Guezennec, Y.G. and W. Hamama, *Two-Zone Heat Release Analysis of Combustion Data and Calibration of Heat Transfer Correlation in an I. C. Engine*, 1999, SAE International.
102. Gatowski, J.A., et al., *Heat Release Analysis of Engine Pressure Data*, 1984, SAE International.
103. Lapuerta, M., O. Armas, and J.J. Hernández, *Diagnosis of DI Diesel combustion from in-cylinder pressure signal by estimation of mean thermodynamic properties of the gas.* Applied Thermal Engineering, 1999. 19(5): p. 513-529.
104. Stiesch, G. and G.P. Merker, *A Phenomenological Model for Accurate and Time Efficient Prediction of Heat Release and Exhaust Emissions in Direct-Injection Diesel Engines*, 1999, SAE International.
105. Sastry, G.V.J. and H. Chandra, *A Three-Zone Heat Release Model for DI Diesel Engines*, 1994, SAE International.
106. Hiroyasu, H., T. Kadota, and M. Arai, *Development and Use of a Spray Combustion Model to Predict Diesel Engine Efficiency and Pollutant Emission.* Bulletin of JSME, 1983. 26(24): p. 569-575.
107. Hiroyasu, H. and K. Nishida, *Simplified Three-Dimensional Modeling of Mixture Formation and Combustion in a DI Diesel Engine.* 1989.
108. Kadota, T., H. Hiroyasu, and H. Oya, *Spontaneous Ignition Delay of a Fuel Droplet in High Pressure and High Temperature Gaseous Environments.* Bulletin of JSME, 1976. 19(130): p. 437-445.
109. Depcik, C., et al., *Instructional use of a single-zone, premixed charge, spark-ignition engine heat release simulation.* International Journal of Mechanical Engineering Education, 2007. 35(1): p. 1-31.
110. Tamilporai, P., et al., *Simulation and Analysis of Combustion and Heat Transfer in Low Heat Rejection Diesel Engine Using Two Zone Combustion Model and Different Heat Transfer Models*, 2003, SAE International.
111. Woschni, G., *A Universally Applicable Equation for the Instantaneous Heat Transfer Coefficient in the Internal Combustion Engine*, 1967, SAE International.
112. Caton, J.A. and J.B. Heywood, *An experimental and analytical study of heat transfer in an engine exhaust port.* International Journal of Heat and Mass Transfer, 1981. 24(4): p. 581-595.
113. Hohenberg, G.F., *Advanced Approaches for Heat Transfer Calculations*, 1979, SAE International.
114. Wu, Y.-Y., B.-C. Chen, and F.-C. Hsieh, *Heat transfer model for small-scale air-cooled spark-ignition four-stroke engines.* International Journal of Heat and Mass Transfer, 2006. 49(21–22): p. 3895-3905.
115. Olorunmaiye, J.A. and J.A.C. Kentfield, *Numerical simulation of valveless pulsed combustors.* Acta Astronautica, 1989. 19(8): p. 669-679.
116. Staley, D.O. and G.M. Jurica, *Flux Emissivity Tables for Water Vapor, Carbon Dioxide and Ozone.* Journal of Applied Meteorology, 1970. 9(3): p. 365-372.
117. Bahadori, A. and H.B. Vuthaluru, *Predicting Emissivities of Combustion Gases.* Chemical engineering progress, 2009. 105(6): p. 38-41.
118. Howell, J.R., R. Siegel, and M.P. Mengüç, *Thermal radiation heat transfer / John R. Howell, Robert Siegel, M. Pinar Mengüç*2011, Boca Raton, Fla.: CRC Press.
119. Nilsson, Y. and L. Eriksson, *Determining TDC Position Using Symmetry and Other Methods*, 2004, SAE International.

120. Pipitone, E., A. Beccari, and S. Beccari, *The Experimental Validation of a New Thermodynamic Method for TDC Determination*, 2007, Consiglio Nazionale delle Ricerche.
121. Pipitone, E., A. Beccari, and S. Beccari, *Reliable TDC position determination: a comparison of different thermodynamic methods through experimental data and simulations*, 2008, SAE International.
122. Brunt, M.F.J. and C.R. Pond, *Evaluation of Techniques for Absolute Cylinder Pressure Correction*, 1997, SAE International.
123. Tazerout, M., O. Le Corre, and S. Rousseau, *TDC Determination in IC Engines Based on the Thermodynamic Analysis of the Temperature-Entropy Diagram*, 1999, SAE International.
124. Zhong, L., N.A. Henein, and W. Bryzik, *Effect of Smoothing the Pressure Trace on the Interpretation of Experimental Data for Combustion in Diesel Engines*, 2004, SAE International.
125. Kee, R.J., et al., *CHEMKIN-III: A FORTRAN chemical kinetics package for the analysis of gas-phase chemical and plasma kinetics*.
126. Chmela, F.G. and G.C. Orthaber, *Rate of Heat Release Prediction for Direct Injection Diesel Engines Based on Purely Mixing Controlled Combustion*, 1999, SAE International.
127. Villarino, M.B., *A Note on the Accuracy of Ramanujan's Approximative Formula for the Perimeter of an Ellipse.* Journal of Inequalities in Pure and Applied Mathematics, 2006. 7.
128. Poetsch, C., H. Ofner, and E. Schutting, *Assessment of a Multi Zone Combustion Model for Analysis and Prediction of CI Engine Combustion and Emissions.* 2011.
129. *The Nomenclature of Lipids.* European Journal of Biochemistry, 1977. 79(1): p. 11-21.
130. Assanis, D.N., et al., *A Methodology for Cycle-By-Cycle Transient Heat Release Analysis in a Turbocharged Direct Injection Diesel Engine*, 2000, SAE International.
131. Kundu, P.K. and I.M. Cohen, *Fluid Mechanics*. 4 ed2010: Academic Press. 872.
132. Alkhulaifi, K. and M. Hamdalla, *Ignition Delay Correlation for a Direct Injection Diese Engine Fuelled with Automotive Diesel and Water Diesel Emulsion.* 2011.
133. Gopalakrishnan, V. and J. Abraham, *An Investigation of Ignition and Heat Release Characteristics in a Diesel Engine Using an Interactive Flamelet Model*, 2003, SAE International.
134. Assanis, D.N., et al., *A Predictive Ignition Delay - Correlation Under Steady-State and Transient Operation of a Direct Injection Diesel Engine.* Journal of Engineering for Gas Turbines and Power, 2003. 125: p. 450-457.
135. Wolfer, H.H., *Ignition Lag in Diesel Engines.* VDI-Forschungsheft, 1938. 392.
136. Stringer, F.W., A.E. Clarke, and J.S. Clarke, *The Spontaneous Ignition of Hydrocarbon Fuels in a Flowing System.* Proceedings of the Institution of Mechanical Engineers, Conference Proceedings, 1969. 184(10): p. 212-225.
137. Henein, N.A. and J.A. Bolt, *Correlation of Air Charge Temperature and Ignition Delay for Several Fuels in a Diesel Engine*, 1969, SAE International.
138. Itoh, Y. and N.A. Henein. *Determination of Ignition Delay in Diesel Engines From Constant Volume Vessels Data*. in *Proceedings of ASEM-ICE Spring Technical Conference*. 1997. New York.
139. Toshikazu, K., H. Hiroyuki, and O.Y.A. Hideo, *Spontaneous Ignition Delay of a Fuel Droplet in High Pressure and High Temperature Gaseous Environments.* Bulletin of JSME, 1976. 19(130): p. 437-445.
140. Hardenberg, H.O. and F.W. Hase, *An Empirical Formula for Computing the Pressure Rise Delay of a Fuel from Its Cetane Number and from the Relevant Parameters of Direct-Injection Diesel Engines*, 1979, SAE International.
141. Watson, N., A.D. Pilley, and M. Marzouk, *A Combustion Correlation for Diesel Engine Simulation*, 1980, SAE International.
142. Spadaccini, L.J., *Autoignition Characteristics of Hydrocarbon Fuels at Elevated Temperatures and Pressures.* Journal of Engineering, 1977. Power(99): p. 83-87.
143. Spadaccini, L.J. and J.A. Tevelde, *Autoignition characteristics of aircraft-type fuels.* Combustion and Flame, 1982. 46(0): p. 283-300.

144. Ryan, T.W. and T.J. Callahan, *Engine and Constant Volume Bomb Studies of Diesel ignition and Combustion*, 1988, SAE International.
145. Fujimoto, H., T. Shimada, and G. Sato, *Study of Diesel Combustion in a Constant Volume Vessel.* Trans. Japan Society of Mechanical Engineering, 1979. 45(392): p. 599-609.
146. Pischinger, F., U. Reuter, and E. Scheid, *Self-Ignition of Diesel Sprays and Its Dependence on Fuel Properties and Injection Parameters.* Journal of Engineering Gas Turbines and Power, 1988. 110: p. 399-404.
147. Lahiri, D., et al. *Utilization of Oxygen-Enriched Air in Diesel Engines: Fundamental Considerations*. in *Paper No. 97-ICE-72*. 1997. New York.
148. Weisser, G., F.X. Tanner, and K. Boulouchos, *Modeling of Ignition and Early Flame Development with Respect to Large Diesel Engine Simulation*, 1998, SAE International.
149. Ando, H., J. Takemura, and E. Koujina, *A Knock Anticipating Strategy Basing on the Real-Time Combustion Mode Analysis*, 1989, SAE International.
150. Syrimis, M., K. Shigahara, and D.N. Assanis, *Correlation Between Knock Intensity and Heat Transfer Under Light and Heavy Knocking Conditions in a Spark Ignition Engine*, 1996, SAE International.
151. Checkel, M.D. and J.D. Dale, *Computerized Knock Detection from Engine Pressure Records*, 1986, SAE International.
152. Klein, M. and L. Eriksson, *A Specific Heat Ratio Model for Single-Zone Heat Release Models*, 2004, SAE International.
153. Asay, R.J., K.I. Svensson, and D.R. Tree, *An Empirical, Mixing-Limited, Zero-Dimensional Model for Diesel Combustion*, 2004, SAE International.
154. Nabi, M.N., *Theoretical investigation of engine thermal efficiency, adiabatic flame temperature, NOx emission and combustion-related parameters for different oxygenated fuels.* Applied Thermal Engineering, 2010. 30(8–9): p. 839-844.
155. Barua, P.K., *Biodiesel from Seeds of Jatropha Found in Assam, India.* International Journal of Energy, Information and Communications, 2011. 2: p. 53-65.
156. Kouremenos, D.A., C.D. Rakopoulos, and D.T. Hountalas, *Experimental investigation of the performance and exhaust emissions of a swirl chamber diesel engine using JP-8 aviation fuel.* International Journal of Energy Research, 1997. 21(12): p. 1173-1185.
157. Canakci, M. and J.H. Van Gerpen, *Comparison of engine performance and emissions for petroleum diesel fuel, yellow grease biodiesel, and soybean oil biodiesel.* Transactions of the ASAE, 2003. 46(4): p. 937-944.
158. Sahoo, P.K. and L.M. Das, *Combustion analysis of Jatropha, Karanja and Polanga based biodiesel as fuel in a diesel engine.* Fuel, 2009. 88(6): p. 994-999.
159. Yao, M., et al., *Diesel Engine Combustion Control: Medium or Heavy EGR?*, 2010, SAE International.
160. Schubiger, R., A. Bertola, and K. Boulouchos, *Influence of EGR on Combustion and Exhaust Emissions of Heavy Duty DI-Diesel Engines Equipped with Common-Rail Injection Systems*, 2001, SAE International.
161. Chalgren, R.D., et al., *A Controlled EGR Cooling System for Heavy Duty Diesel Applications Using the Vehicle Engine Cooling System Simulation*, 2002, SAE International.
162. Rothamer, D.A. and L. Murphy, *Systematic study of ignition delay for jet fuels and diesel fuel in a heavy-duty diesel engine.* Proceedings of the Combustion Institute, 2013. 34(2): p. 3021-3029.
163. Jayashankara, B. and V. Ganesan, *Effect of fuel injection timing and intake pressure on the performance of a DI diesel engine – A parametric study using CFD.* Energy Conversion and Management, 2010. 51(10): p. 1835-1848.
164. Shahabuddin, M., et al., *Ignition delay, combustion and emission characteristics of diesel engine fueled with biodiesel.* Renewable and Sustainable Energy Reviews, 2013. 21(0): p. 623-632.
165. Zhu, G.G., C.F. Daniels, and J. Winkelman, *MBT Timing Detection and its Closed-Loop Control Using In-Cylinder Pressure Signal*, 2003, SAE International.

166. Pipitone, E. and A. Beccari, *A Study on the Use of Combustion Phase Indicators for MBT Spark Timing on a Bi-Fuel Engine*, 2007, Consiglio Nazionale delle Ricerche.
167. Asad, U. and M. Zheng, *Real-time Heat Release Analysis for Model-based Control of Diesel Combustion*, 2008, SAE International.
168. Kumar, R., et al., *Heat Release Based Adaptive Control to Improve Low Temperature Diesel Engine Combustion*, 2007, SAE International.
169. Schiefer, D., R. Maennel, and W. Nardoni, *Advantages of Diesel Engine Control Using In-Cylinder Pressure Information for Closed Loop Control*, 2003, SAE International.
170. de O. Carvalho, L., T.C.C. de Melo, and R.M. de Azevedo Cruz Neto, *Investigation on the Fuel and Engine Parameters that Affect the Half Mass Fraction Burned (CA50) Optimum Crank Angle*, 2012, SAE International.
171. Asad, U. and M. Zheng, *Fast heat release characterization of a diesel engine.* International Journal of Thermal Sciences, 2008. 47(12): p. 1688-1700.
172. Mattson, J.M.S., et al., *Recommendations for the Next Generation of Hydrocarbon Modeling with Respect to Diesel Exhaust Aftertreatment and Biodiesel Fuels*, 2013, SAE International.
173. Kweon, C.-B., et al., *Effect of Injection Timing on Detailed Chemical Composition and Particulate Size Distributions of Diesel Exhaust*, 2003, SAE International.
174. Tsurushima, T., L. Zhang, and Y. Ishii, *A Study of Unburnt Hydrocarbon Emission in Small DI Diesel Engines*, 1999, SAE International.
175. Krailler, R. and D. Russell, *Laser-ion beam photodissociation studies of C4H4 radical cations.* Organic mass spectrometry, 1985. 20(10): p. 606-613.

Appendices

Table 24. Examples of the molecular formula and lipid number of various FAME species, as well as their fractional composition within used cooking oil, rapeseed oil, and olive oil derived biodiesels, measured by GCMS.

Species	Formula	Lipid Number	Biodiesel Source		
			Used Cooking Oil	Rapeseed Oil	Olive Oil
Caproic	$C_7H_{14}O_2$	C6:0	0.00±0.00	0.00±0.00	0.00±0.00
Caprylic	$C_9H_{18}O_2$	C8:0	0.00±0.00	0.00±0.00	0.00±0.00
Capric	$C_{11}H_{22}O_2$	C10:0	0.01±0.00	0.01±0.00	0.01±0.00
Lauric	$C_{13}H_{26}O_2$	C12:0	0.00±0.00	0.00±0.00	0.00±0.00
Myristic	$C_{15}H_{30}O_2$	C14:0	0.00±0.00	0.00±0.00	0.00±0.00
Palmitic	$C_{17}H_{34}O_2$	C16:0	0.07±0.01	0.03±0.01	0.09±0.01
Palmitoleic	$C_{17}H_{32}O_2$	C16:1	0.00±0.00	0.00±0.00	0.00±0.00
Stearic	$C_{19}H_{38}O_2$	C18:0	0.02±0.00	0.01±0.00	0.02±0.00
Oleic	$C_{19}H_{36}O_2$	C18:1	0.58±0.03	0.14±0.02	0.74±0.02
Elaidic	$C_{19}H_{36}O_2$	C18:1	0.00±0.00	0.01±0.00	0.00±0.00
Linoleic	$C_{19}H_{34}O_2$	C18:2	0.27±0.03	0.12±0.03	0.14±0.02
Linoelaidic	$C_{19}H_{34}O_2$	C18:2	0.00±0.00	0.00±0.00	0.00±0.00
α-Linolenic	$C_{19}H_{32}O_2$	C18:3	0.06±0.01	0.10±0.03	0.00±0.00
γ-Linolenic	$C_{19}H_{32}O_2$	C18:3	0.00±0.00	0.00±0.00	0.00±0.00
Arachidic	$C_{21}H_{42}O_2$	C20:0	0.0±0.00	0.00±0.00	0.00±0.00
Eicosenoic	$C_{21}H_{40}O_2$	C20:1	0.00±0.00	0.06±0.01	0.00±0.00
Behenic	$C_{23}H_{46}O_2$	C22:0	0.00±0.00	0.51±0.00	0.00±0.00

Table 25. Examples of the molecular formula and lipid number of various FAME species, as well as their fractional composition within palm oil, coconut oil, and soybean oil derived biodiesels, measured by GCMS.

Species	Formula	Lipid Number	Biodiesel Source		
			Palm Oil	Coconut Oil	Soybean Oil
Caproic	$C_7H_{14}O_2$	C6:0	0.00±0.00	0.02±0.11	0.00±0.00
Caprylic	$C_9H_{18}O_2$	C8:0	0.00±0.00	0.09±0.01	0.00±0.00
Capric	$C_{11}H_{22}O_2$	C10:0	0.01±0.00	0.07±0.01	0.00±0.00
Lauric	$C_{13}H_{26}O_2$	C12:0	0.01±0.00	0.50±0.03	0.00±0.00
Myristic	$C_{15}H_{30}O_2$	C14:0	0.01±0.00	0.19±0.02	0.00±0.00
Palmitic	$C_{17}H_{34}O_2$	C16:0	0.44±0.03	0.08±0.01	0.10±0.01
Palmitoleic	$C_{17}H_{32}O_2$	C16:1	0.00±0.00	0.00±0.00	0.00±0.00
Stearic	$C_{19}H_{38}O_2$	C18:0	0.03±0.00	0.01±0.00	0.04±0.00
Oleic	$C_{19}H_{36}O_2$	C18:1	0.43±0.03	0.05±0.01	0.23±0.02
Elaidic	$C_{19}H_{36}O_2$	C18:1	0.00±0.00	0.00±0.00	0.02±0.00
Linoleic	$C_{19}H_{34}O_2$	C18:2	0.08±0.01	0.00±0.00	0.54±0.04
Linoelaidic	$C_{19}H_{34}O_2$	C18:2	0.00±0.00	0.00±0.00	0.00±0.00
α-Linolenic	$C_{19}H_{32}O_2$	C18:3	0.00±0.00	0.00±0.00	0.07±0.01
γ-Linolenic	$C_{19}H_{32}O_2$	C18:3	0.00±0.00	0.00±0.00	0.00±0.00
Arachidic	$C_{21}H_{42}O_2$	C20:0	0.00±0.00	0.00±0.00	0.00±0.00
Eicosenoic	$C_{21}H_{40}O_2$	C20:1	0.00±0.00	0.00±0.00	0.00±0.00
Behenic	$C_{23}H_{46}O_2$	C22:0	0.00±0.00	0.00±0.00	0.00±0.00